

**Mechanical Strain Bioreactor Design and Assessment for Culture of Human
Airway Smooth Muscle**

by

ANDREW CAVERS

BASc, Engineering Physics, UBC, 2013

A THESIS SUBMITTED IN PARTIAL FULFILLMENT OF THE REQUIREMENTS FOR THE
DEGREE OF

MASTER OF APPLIED SCIENCE

in

THE FACULTY OF GRADUATE AND POSTDOCTORAL STUDIES
(Biomedical Engineering)

THE UNIVERSITY OF BRITISH COLUMBIA
(Vancouver)

SEPTEMBER 2016

©Andrew Cavers, 2016

Abstract

Bioreactors capable of subjecting cells and tissues to time-varying mechanical strain are one aspect of simulating *in vivo* conditions. A bioreactor to impart arbitrary strain waveforms on cells or tissue scaffolds for loading conditions found in the airway was designed and developed and, in the process, it was determined that there are sources of experimental error which could invalidate bioreactor experiments if not properly mitigated. Without effective design and validation, bioreactors can impart significantly different stimuli than the assumed experimental conditions.

Cyclic strain is thought to play a role in airway remodeling by mediating cytoskeletal contraction of the airway smooth muscle. *In vitro* experiments have demonstrated varying changes to the cytoskeleton depending on experimental conditions. Based on literature review, the strain waveform, magnitude, mechanical properties of the substrate, and anisotropy of the strain stimulus may all affect airway smooth muscle (ASM) differentiation. A bioreactor capable of imparting a broad range of strain stimulus was developed using stepper motors as actuators to allow open-loop control.

Any changes in the cells subjected to cyclic strain in these bioreactors would be assumed to correlate with cyclic strain, but a poorly designed bioreactor could introduce confounding experimental stimuli which could easily invalidate the experiment. Heat generated by the actuators can overheat the cell cultures. Vibration might alter the cytoskeletal response. Strain response across the substrate can drastically vary from modeling predictions depending on the loading conditions and how the substrate has been constrained.

Methods of mitigating heat generation and transfer were developed. The vibrations emitted by the two stepper motor options were evaluated. A method of mapping the substrate was developed such that nonplanar strains across the substrate surface could be characterized to validate the experimental conditions prior to testing. Finally, ASM cells were subjected to cyclic and static strain on PDMS substrates and cell realignment evaluated. Cells were noted to realign in the cyclic strain tests, as has been

reported in several earlier publications, but also realigned under static strain conditions. The bioreactor design objectives were met.

Preface

This thesis is original, unpublished, independent work by the author, with the exception of the idea to coat the PDMS membranes with PEDOT:PSS, which was contributed by Konrad Walus. *In vitro* culture of HASMcs was conducted under bioethics approval #H11-00301-A005.

Table of Contents

Abstract	ii
Preface.....	iv
Table of Contents	v
List of Tables	viii
List of Figures	ix
Acknowledgements	xi
1 Introduction	1
1.1 Motivation	1
1.2 Objectives.....	3
1.3 Literature Review	3
1.3.1 Airway Physiology	4
1.3.2 Asthma, COPD and Airway Wall Remodeling	7
1.3.3 Physiology of ASM Contraction In Normal And Remodeled Airways	10
1.3.4 Contractile and Synthetic HASMc Phenotypes.....	12
1.3.5 Tissue Engineering HASMc Studies	14
1.4 Literature Review Summary	18
2 Bioreactor Design and Implementation.....	20
2.1 Modeling Of Strain Across a Hyperelastic Substrate.....	21
2.2 Actuator Selection	29
2.2.1 Actuator Options And Prior Art	29
2.2.2 Selection Constraints	32
2.2.3 Implementation.....	33
2.3 Enclosure Design.....	40

2.3.1	Heat Transfer Modeling And Simulation	45
2.3.2	FEA Modeling Of Heat Exchange Inside the Incubator.....	47
2.4	Strain Characterization	51
2.4.1	Strain Across a Unit Square.....	52
2.4.2	Surface Strain Measurement Error Due to Height Measurement Error.....	53
2.4.3	Vertical Deformation Mapping Methods.....	54
2.4.4	Conclusions	55
3	Results	58
3.1	Actuator Validation	58
3.1.1	Discussion: Actuator Design, Implementation, and Testing	61
3.1.2	Conclusions	63
3.2	Enclosure Validation	63
3.2.1	Bioreactor Temperature Rise and Cooling Test	64
3.2.2	Heat Output and Temperature Rise Inside Incubator	65
3.2.3	Discussion: Heat Exchange and Enclosure Design	68
3.2.4	Conclusions: Bioreactor Thermal Isolation and Cooling	70
3.3	Strain Characterization	71
3.3.1	Topographical Mapping Using Depth of Focus	71
3.3.2	Contact Sensor Accuracy.....	74
3.3.3	Discussion: Strain Characterization.....	75
3.3.4	Conclusions	76
3.4	HASM Response	76
3.4.1	Effects Of Static And Cyclic Strain And Experimental Design	79
4	Conclusions	82

References 84

List of Tables

Table 1.1: Indicators of contractile and synthetic phenotypes.....	14
Table 1.2: Cell response to various experimental conditions.	19
Table 2.1: Ogden parameters for modeling of hyperelastic response of PDMS.....	24
Table 2.2: Depiction and description of different actuators in prior art.....	29
Table 2.3: Actuator selection requirements.	33
Table 2.4: Voltage, current, and power draw for the Canstack and Vexta motor options.	46

List of Figures

Figure 1.1: Basic anatomy of the lung and bronchi.	5
Figure 1.2: Cross-sectional profile of the airway wall.	6
Figure 1.3: Normal airway, left, and remodeled airway, right.	8
Figure 1.4: Actin-myosin contractile filament and close-up illustration of myosin cross-bridge.	11
Figure 1.5: Illustration of uniaxial and biaxial strain across a pneumatically actuated well.	15
Figure 2.1: Illustration of radial, and circumferential strain fields across a radial cross-section.	22
Figure 2.2 Relationship between the stress on a substrate, the strain across the substrate, and the strain energy function of the substrate for a linear elastic stress-strain response.	23
Figure 2.3: Alternative models using pneumatic and plunger loading of the PDMS membrane in the axisymmetric FEA models.	25
Figure 2.4: Radial and circumferential strains as a function of radius when deflected by pneumatic or plunger loading.	26
Figure 2.5: Strain profiles as a result of varying the plunger width and membrane thickness.	27
Figure 2.6: Membrane deflection versus force for membranes varying in thickness from 0.5 mm to 1.5 mm.	28
Figure 2.7: Linear stepper motor with keyhole bearing.	34
Figure 2.8: Rotary stepper motor with flexural bearing.	35
Figure 2.9: Solidworks linear elastic analysis of the flexure when the nut holder is at 5 mm deflection height.	36
Figure 2.10: The initial, smoothed and discretized waveforms produced using the motor controller Matlab code.	39
Figure 2.11: Control electronics block diagram.	40
Figure 2.12: Initial one-well bioreactor design.	42
Figure 2.13: Final bioreactor design.	43

Figure 2.14: Cell culture well and laser-etched PDMS membrane.....	44
Figure 2.15: Actuator with stepper motor and flexural bearing.....	45
Figure 2.16: Simulation of the heat transfer out of the bioreactor and across the incubator shelf (seen from above).....	48
Figure 2.17: Bioreactor and incubator cross-section.....	49
Figure 2.18: Temperature of the incubator over a 24 hour period 5 cm from the top of the bioreactor in the FEA simulation.	50
Figure 3.1: Actuator motion for 3 cycles.	59
Figure 3.2: Motor vibration, 100 Hz bandwidth.	60
Figure 3.3: Illustration of locations of temperature sensors during bioreactor cooling test.....	64
Figure 3.4: Enclosure temperature inside the bioreactor and in the well.....	65
Figure 3.5: Diagram of bioreactor mockup to test temperature rise.	66
Figure 3.6: Bioreactor temperature rise inside the incubator as a function of time for 6 to 24 W heat sources, modelling various motor combinations.....	67
Figure 3.7: Position measurement repeatability of the camera in x,y,z	72
Figure 3.8: Mapped strain of deformed membrane surface	73
Figure 3.9: Measurement error for the touch probe.	74
Figure 3.10: Cells before and after cyclic strain.	77
Figure 3.11: Diagram illustrating cell alignment calculation.....	78
Figure 3.12: Realigned HASMCs on D3-4, static strain conditions.....	78
Figure 3.13: Variance in cell direction as affected by cyclic and static strain, compared to an unstrained control.	79

Acknowledgements

It would not have been possible to complete this thesis without the selfless contributions of the Engineering Physics program, Scott Lawson, and UBC Rapid. I am deeply grateful for the efforts of Gurpreet Singheera and Christoph Sielmann, the respective lab managers of the Dorscheid and Walus labs, for their relentless professionalism and capability; being able to rely on you helped keep me sane. The software available through CMC Microsystems was invaluable for completing the thesis. I would also like to thank the NSERC CREATE program for the incredible experiences I've had in the Engineers in Scrubs program and for providing one year worth of funding for my research assistantship stipend, Dr Del Dorscheid for his tireless mentorship and support in his role as clinical supervisor for this project as well as providing half of the remaining research assistantship stipend, and Konrad Walus, for providing the remainder of the funding.

1 Introduction

1.1 Motivation

How airway smooth muscle (ASM) cells and tissues remodel in response to mechanical strain is central to the pathology of asthma and chronic obstructive pulmonary disorder (COPD). COPD and asthma involve remodeling of airway smooth muscle tissues, which has been thought to result in increased responsiveness and constriction in response to aggravating stimuli[1]. During breathing, cyclic stretches in the airways affect the remodeling process and cell phenotype and function when paired with altered stiffness and strain response due to inflammation. The *in vitro* study of asthma and COPD require devices capable of replicating the cyclical mechanical strain conditions in the airway on *in vitro* cells or tissues; these devices are usually referred to as *bioreactors*, a blanket term for all devices that subject cells or tissues to particular experimental conditions including mechanical strain, fluid flow, or periodic chemical exposure [2]. Commercial bioreactors for this purpose are expensive and typically accommodate a limited repertoire of experimental conditions. A new bioreactor capable of a wider range of mechanical strain conditions was developed to facilitate studies of ASM behavior when affected by cyclic mechanical strain. During this process, several issues in bioreactor design were determined to have significant potential consequences for the validity of the experiments conducted in these devices. Mitigation for these issues were designed, implemented, tested and are discussed.

The *in vitro* study of asthma, COPD, and other diseases with similar pathologies of airway wall stiffening require bioreactors capable of replicating the cyclical mechanical strain conditions in the airway. Asthma affects as many as 3 million or roughly 8% of all Canadians[3] and is a chronic inflammatory disorder of the airway in which inflamed tissues constrict and cause obstruction of the airway leading to breathing difficulties[4]. These asthma attacks, which are the archetypical symptom of asthma, are characterized by a rapid and exaggerated *bronchoconstriction* in response to a stimulus[5]. While various cell types in the airway are implicated in asthma pathophysiology[6] and airway obstruction, smooth muscle tissues are functionally responsible for reversible airway constriction.

COPD is another chronic inflammatory disease in which airway wall remodeling and airflow obstruction play a role in the progression of the disease. Like asthma, COPD also features remodeling of smooth muscle tissues into hyper-functional phenotypes[7]. Unlike asthma, COPD symptoms cannot be reversed, although bronchodilators can help control the symptoms[8]. While smoking is the predominant cause of COPD in the developed world, people in the developing world often develop COPD as a result of air pollution from poorly ventilated cooking fires ('biofuel-induced COPD'[9]). As much as 5% of the world population suffers from COPD and it is projected to be the third leading cause of death worldwide by 2030[10].

The mechanical strains that cells are subjected to during breathing, coupled with the biomechanics of a remodeled airway, have long been implicated in the pathology of asthma and COPD[11]. Replicating the biomechanical conditions of the airway is one aspect of research for both asthma and COPD.

The problem with studying human airway smooth muscle cell (HASM) contractility and asthmatic or COPD-related phenotypes *in vitro* is that when using standard cell culture techniques, it is not feasible to stretch the cultures and HASMs quickly lose the properties that allow them to contract at all. Contractile phenotype HASMs have various cytoskeletal components which render them capable of contraction. *In-vitro* studies since 1996 have shown that these elements decrease substantially over the course of typical *in vitro* culturing [12]. It has been hypothesized that mechanical forces [13] may play a role in HASM differentiation and regulation of contractile phenotype, although biochemical cues and interactions with other cells and tissues in the airway certainly also play key roles [7]. Standard culture techniques result in a cell that lacks the cytoskeletal machinery necessary for studying the HASM “overdevelopment” inherent to asthma and COPD. Studying ASM cell or tissue response to strain *in vitro* requires bioreactors capable of stretching airway smooth muscle cells to determine how mechanical strain influences the HASM phenotype.

To test the full scope of biomechanical conditions cells are subjected to *in vivo*, a new bioreactor was designed. Respiratory waveforms vary in amplitude and period from breath to breath and the resulting

strain patterns are further altered by an increasingly stiff and remodeled airway wall. This bioreactor was designed to produce an arbitrary strain waveform and methods were developed to characterize the strain in the well. Further, various potential problems in bioreactor design were identified and potential design mitigation methods were explored.

The biomechanical aspect of airway remodeling is a crucial element of asthma, COPD, and other chronic respiratory disorders. Developing more effective tools to impart and measure cyclic strain stimuli on cell cultures is necessary and this has motivated my work.

1.2 Objectives

The objectives of this thesis are to:

1. Design and construct a mechanical strain bioreactor that is sufficiently robust in design such that it can be modified to fulfill the widely varying range of substrates and mechanical strain regimens that have been previously employed or suggested to play a role in replicating the conditions in airway wall remodeling.
2. Discuss the various potential confounding experimental conditions the cells may inadvertently be subjected to in a bioreactor due to design issues.
3. Develop and test methods of validating bioreactor operation.
4. Provide recommendations for future bioreactor design to avoid various design pitfalls that could significantly affect experimental results.

1.3 Literature Review

Airway smooth muscle (ASM) plays a significant role in airway narrowing and remodeling common to asthma and COPD. ASM tissue lies within the airway and can be chemically stimulated by immune system cells or the nervous system to stiffen or narrow the airway, decreasing the airflow. Human airway smooth muscle cells (HASMcs) accomplish this narrowing by activating contractile Alpha-smooth muscle actin (Alpha-SM actin) and myosin filaments within their cytoskeletal structure. In asthma and

COPD, the structure of the airway wall becomes stiffer and thicker and the ASM tissues can sufficiently contract such that airflow can be entirely obstructed. Exaggerated, *hypertrophic* contractile function at a cellular level is a key element in asthma and COPD pathology. However, ASM contractility cannot be replicated in standard lab conditions as standard *in vitro* culture techniques lead to loss of the contractile phenotype. While there are various approaches to altering HASMc phenotype *in vitro*, mechanical strain has often been employed, either to attempt to restore contractile function or to study how HASMcs respond to the cyclic stretches they are subjected to during respiration. These bioreactor tests have delivered widely varying results depending on how the cells have been subjected to mechanical strain.

1.3.1 Airway Physiology

The smaller *bronchioles* near the *alveoli*, in which oxygen is exchanged, are approximately 3 mm in diameter and are the regions of the airway which most obstruct airflow during asthma and COPD. Airways consist of an *epithelial* layer, which provides a protective barrier function, a basement membrane that provides structural support for the epithelium and remains elastic to permit the cyclical changes associated with respiration, an interstitial region or *submucosal* space of connective tissue, nerves, capillaries and lymphatics, and a layer of ASM tissue, the *muscularis*. Mechanical loading and strain of these tissues occurs cyclically during respiration.

The basic physiology of the lung and the airways is depicted in Figure 1.1. The trachea leads into the primary bronchus, which then successively divides into increasingly narrower airways of simpler structure and composition. These airways permeate the lung tissue and terminate in the alveoli in which oxygen is exchanged with carbon dioxide at the capillary/alveoli interface.

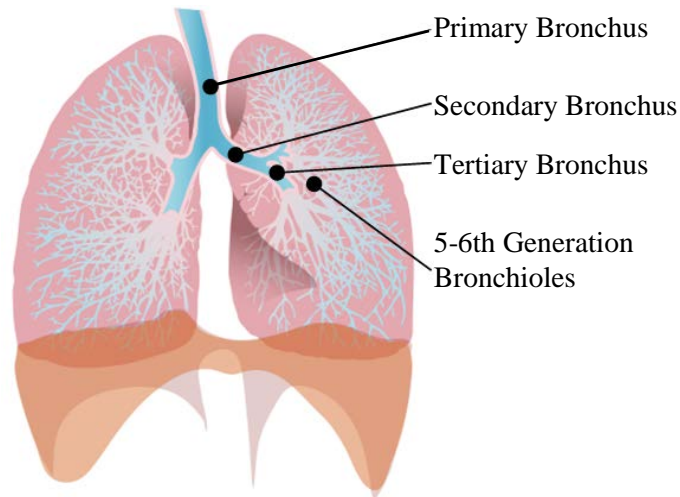


Figure 1.1: Basic anatomy of the lung and bronchi. The windpipe splits successively into smaller bronchioles. Bronchioles 5 to 6 generations from the trachea are a few millimeters in diameter, remodel in COPD and asthma, and impede airflow in those disorders. Reproduced under creative commons license.

The smaller bronchioles, 5 to 6 successive bifurcations (or 'generations') from the primary bronchus, have been shown to be the predominant airway region in which stiffening and over-constriction can impede respiration[15] and as such are the focus of study in COPD and asthma. The tissues that are the structural elements of the airway wall in these smaller, 5 to 6th generation airways are depicted in Figure 1.2 and are described in further detail below[15-16]:

- 1 **Epithelium.** The epithelium provides a barrier against pathogens and other airborne hazards to the body. The epithelium is composed of multiple cell types in a multi-layered architecture. This continuous layer of cells secretes mucous, uses synchronized beats of their cilia to move this mucous through the airway, regulates hydration of the airway and participates in immune system regulation.
2. **Submucosa.** This layer includes the basement membrane, a thin but dense layer of tissue that the epithelial cells anchor into, and a looser layer of connective tissue beneath it. Fibroblast and myofibroblast cells inhabit this layer, as well as immune cells which transiently migrate through this space.

3. **Muscularis.** The epithelial and submucosa layers are girded by a layer of airway smooth muscle tissue. The connective tissue surrounding the muscularis becomes increasingly less dense at increasing distance from the airway, ultimately merging with the interstitial connective tissue that surrounds the bronchioles and alveoli. The nervous system and vascular capillary network also reside in this region.

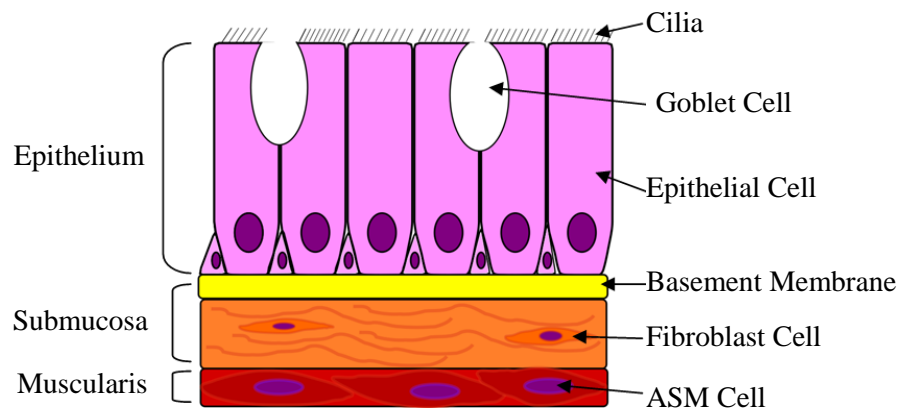


Figure 1.2: Cross-sectional profile of the airway wall.

The airway wall is constantly subjected to mechanical strain. The tidal rhythm of breathing dilates the airway at a frequency of roughly 0.2-0.5 Hz and the magnitude and waveform will vary between breaths. These strains are less than 10% of airway diameter based on most *ex vivo* trials of airway strain during normal respiration[15], which is produced by a combination of air pressure inside the airway and forces from the interstitial connective tissue anchoring it to the surrounding lung[16]. The stiffness of the airway wall is dependent on the thickness, density, and stress-strain response of the epithelial, submucosal, and ASM layers. The strain waveform to which the ASM layer is subjected could vary depending on how the airway has remodeled.

The ASM tissues inside the bronchiolar wall can actively regulate their inner diameter (the airway *lumen*, the open space lined by epithelium through which air travels). Airway constriction and dilation facilitated by ASM tissues may optimize airflow into the alveoli to maximize O₂/CO₂ exchange; various

irritants, such as air pollutants or pollen, can trigger airway constriction as well[17]. Either the autonomic nervous system or immune cells residing in the submucosa can release neurotransmitters and agonists that bind with receptors on the HASMcs, such as *histamine*, *acetylcholine*, and *methacholine*, which cause the ASM to contract the airway[18]. Other agonists, such as *norepinephrine* bind to the β_1 or β_2 receptors on the cell causing relaxation of HASMcs and resulting in airway dilation[19]. The autonomic nervous system can elicit either response by producing suitable agonists. Additional contractile agonists can be produced by immune cells, specifically mast cells, in the submucosa. The immune cells can trigger airway contraction in response to a variety of foreign particles and irritants, such as air pollutants or pollen, as well as temperature changes or physical exertion[20].

The 5 to 6th generation bronchioles in the lungs consist of an epithelial layer, a submucosal region of loose elastic tissue and airway smooth muscle tissue. Respiration subjects these airways to mechanical strain, which varies as a function of the thickness and mechanical properties of the airway tissues. The ASM is able to regulate airway lumen diameter in response to agonists released by either immune cells or the nervous system. As will be discussed in the following section, the mechanical response of the airway and the behavior of the ASM is altered during asthma and COPD.

1.3.2 Asthma, COPD and Airway Wall Remodeling

Airway remodeling in asthma and COPD are key to the pathology of both diseases. In either condition, an increasingly stiffer and thicker airway wall contributes to increased airway narrowing, airflow obstruction and the symptom of increasing difficulty breathing or dysapnea. In asthma, the ASM layer specifically becomes *hyper-responsive* and capable of rapidly constricting the airway in response to aggravating environmental stimuli. The epithelium, submucosal layer, and ASM tissue can also all increase in density and stiffness to result in a stiffer, thicker airway wall, though this remodeling process is poorly understood. The biomechanics of ASM strain response at both a cellular and tissue level, coupled with structural changes to the airway, are thought to play a significant role in the progression of

asthma and COPD as it relates to airway mechanics. The differences between a normal and remodeled airway are illustrated in Figure 1.3.

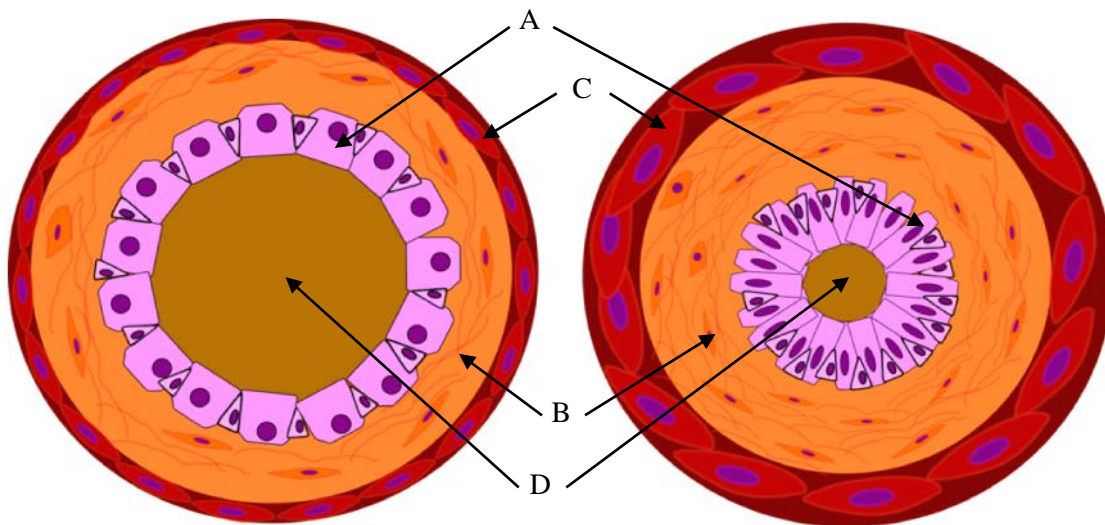


Figure 1.3: Normal airway, left, and remodeled airway, right. Thickening of the epithelial(A), submucosal(B), and muscularis(C) tissues decreases the radius of the airway lumen(D), impeding airflow. The ASM cells in the muscularis may become increasingly contractile or contract more rapidly in response to stimuli.

Asthma is characterized by airflow obstruction, particularly due to the hyper-responsive ASM. This may result from a combination of genetic, immune and inflammatory processes in the lung. Generally, asthma is thought to initiate from a disproportionate inflammatory response in response to normal environmental particles or allergens when combined with a respiratory viral infection[6]. This exaggerated inflammatory response combined with the appropriate genetic background permits similar reactions during subsequent allergen exposures. There is a wide range of severity in symptoms and the extent to which the disease becomes progressively worse and less manageable[21]. While initial asthma symptoms can be mild, the disease can progress to increasingly rapid and exaggerated bronchoconstriction due in part to airway remodeling[22] and hyper-responsive ASM. The ASM tissues can increase in mass or number (*hypertrophy* or *hyperplasia* respectively). Different phenotypes of asthma may be based on different combinations of hyperplasia and hypertrophy[23]. The archetypical symptom of asthma is airway hyper-responsiveness, in which the airway smooth muscle constricts the

airway in response to an appropriate stimulus with increased sensitivity and/or reactivity; for example, the bronchoconstricting drug methacholine produces this effect and is often used to diagnose asthma [17]. The causes of airway hyper-responsiveness are not clear; the explosive “asthma attack” *bronchospasms* were thought to indicate an abnormal ASM[24], but the exact role of ASM in airway hyper-responsiveness is still an open investigation[25],[26].

Chronic obstructive pulmonary disorder (COPD) has similar symptoms to asthma since both diseases show pronounced inflammation and airway remodeling. COPD presents with chronic airflow limitation and obstruction caused by obstruction in small airways - a state known as *chronic bronchitis* or *obstructive bronchiolitis* and emphysema[10]. COPD generally develops after chronic exposure to the noxious particulates in smoke[7]. In the small airways, this leads to chronic inflammation, alteration in the composition of the sub-mucosal connective tissues that lead to stiffening, and increases in density of the airway extra-cellular matrix (ECM), with coinciding increases in density and contractility of HASMc to compensate.

During remodeling, the airway wall tends increase in density and stiffness[22], particularly in the basement membrane[3], resulting in increased airway obstruction. One issue with COPD is that, unlike asthma, symptoms are not alleviated with treatment. In both disorders, the ASM tissue becomes increasingly contractile, dense, and thick, although asthma is characterized by increased hyper-responsive contraction.

Airway wall remodeling plays a role in both diseases, although certain pathways proceed differently in each disease[27]. In fact, patients experiencing symptoms attributable to both diseases has led to the definition of a new disorder, Asthma-COPD Overlap Syndrome (ACOS)[28]. Altered strain response due to airway remodeling has been implicated as a driver for dysfunctional HASMc phenotype [11],[29]. For the past two decades, the idea that mechanical forces and strains in the small airways affect or mediate remodeling and hyper-responsiveness[30] and play a role in the progression of both diseases has been a focus of investigation.

Asthmatic airways place an altered mechanical load on the ASM tissues and how ASM cells and tissues respond to mechanical strain may be a key element in understanding the disorder. As the airway tissue thickens and increases in density, the ASM tissue can become increasingly contractile, and in asthma in particular, feature an increasingly rapid contractile response. Modeling the symptoms and progression of asthma, COPD and airway wall remodeling in ASM tissues and cells requires modeling how altered strain conditions in the airway alter ASM behavior and contraction.

1.3.3 Physiology of ASM Contraction In Normal And Remodeled Airways

ASM tissues are similar to the other smooth muscle tissues in the body. Contractile filaments consisting principally of Alpha-SM actin and myosin proteins are part of the cytoskeletal network, a structure inside the cells which provides an internal mechanism that can exert forces on the surrounding environment via the attachments to the cell membrane[31]. Contraction and forces generated by actin-myosin filaments allows cells to contract or subject their substrate to compressive loads, alter cellular morphology or stiffness, or to move across a substrate. Interactions between Alpha-SM actin and myosin are responsible for active force output and shortening, although mechanical properties of the cytoskeleton such as tensile stiffness may be affected by other cytoskeletal components[32].

While skeletal muscle is responsible for voluntary movements, smooth muscle tissue autonomously regulates certain functions within many organs. Smooth muscle autonomously contracts various tissues in the body including veins, arteries, and the iris in the eye[33]. The main role of smooth muscle in the body is to contract in response to various stimuli, such as chemical signals or changes in mechanical load[34].

There are multiple biochemical factors that control and mediate smooth muscle contractions[35]. Actin filaments are bundled together with myosin filaments into myofibrils. The myosin filaments are comprised of myosin heavy chain strands with globular heads which include myosin light chain (MLC) molecules[35]. When contraction is triggered, the myosin filaments exert force on the Alpha-SM actin filaments, decreasing the filament length. A myosin-actin contractile filament is illustrated in Figure 1.4.

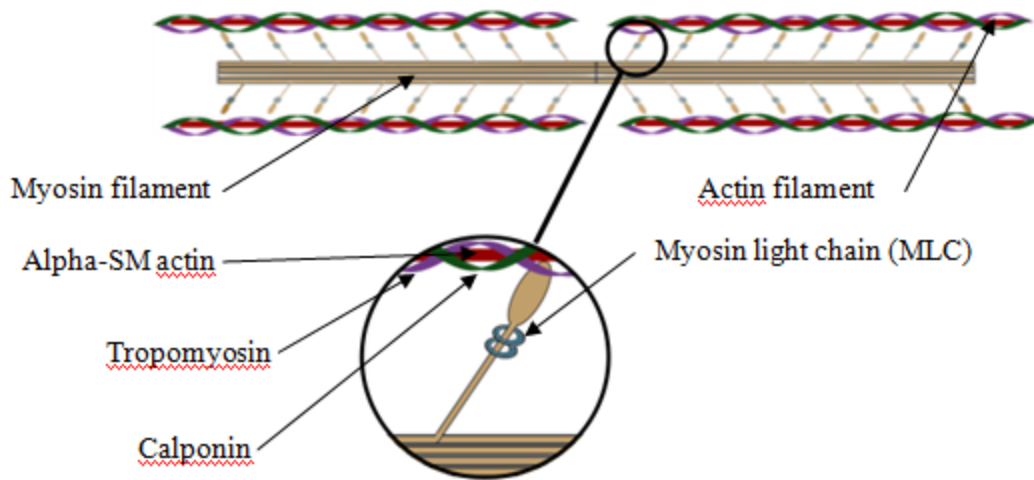


Figure 1.4: Actin-myosin contractile filament and close-up illustration of myosin cross-bridge. Activation of the myosin cross-bridges via myosin light chain enables contraction.

The process is enabled with myosin light chain kinase (MLCK) and disabled with myosin light chain phosphatase (MLCP)[19]; MLCK is activated by a chain of biochemical reactions ultimately initiated by the calcium ions released by spasmogen receptors, for example, histamine receptors[34]. The most familiar application of these contractile filaments is mediating cell stiffness or exerting forces on surrounding tissues, but these contractile filaments also play roles in eukaryotic cell migration and shape[36]. In addition to Alpha-SM actin, the actin filaments also include tropomyosin and calponin, which inhibit the myosin heads from contracting the actin filaments until they are deactivated by calcium ions[37]. These filaments are ultimately connected to the cell membrane, although there may be intermediate connections between two actin-myosin filaments via dense bodies, which are composed of desmin among other proteins[38].

The interactions between Alpha-SM actin and myosin filaments lead to varying force outputs for mechanical loads of varying frequency. Although ASM cells have an approximately proportional stress-strain response to smaller, low-frequency strains, the cells soften in response to larger strains or when cyclically loaded and unloaded more than once per 10-15 minutes [39]. In these cases, the myosin heads are thought to have detached from the Alpha-SM actin fibers, resulting in temporary force decreases[40]

and a new equilibrium position for stress-strain response. ASM cells have been shown to adapt their force output as they are subjected to strain; when the length of an ASM cell is increased or decreased, the contractile force generated by the cell will briefly increase or decrease, but after a period of several minutes will have adjusted and will return to its original force output[41]. The cyclic strains associated with respiration seem to affect actin-myosin filament binding and the cell is never at any particular length long enough to reach its maximum force output[42].

The behavior of asthmatic ASM is altered by exposure to contractile agonists and altered airway stiffness. The ASM tissue in an asthmatic airway is continuously exposed to contractile agonists and continuously generates contractile forces on the airway[43], which may contribute to the described hyper-responsiveness. The altered mechanical loading in a remodeled airway may prevent tidal volume respiration from disrupting actin-myosin binding leading to the exaggerated ASM contraction present in asthma and COPD [15], [44]. The effects of mechanical perturbation have also been explored for potential therapeutic effect; whether deeper inspirations can briefly 'reset' ASM tone has been the subject of various experiments[45].

The actin-myosin binding and the resulting force generated by ASM cells is thought to be mediated by respiratory strains in a non-asthmatic airway, and it is thought that the conditions in a remodelled airway disrupt this process and lead to exaggerated ASM contraction and the hyper-responsiveness that is characteristic of the asthmatic airway. Studying the process through which the ASM tissue becomes increasingly hyper-functional or hyper-responsive requires studying how contractile HASMCs respond to time-varying strain stimulus.

1.3.4 Contractile and Synthetic HASMC Phenotypes

ASM phenotype *in vivo* is highly contractile, but loses its contractile capabilities as well as several biomarkers for contractile phenotype during *in vitro* culture. As discussed below, alternate substrates, cytokine or interleukin interactions, and exposure to cyclic tensile strain may be relevant to *in vivo* HASM behavior and phenotype in remodelled airways.

HASMc cell phenotype *in vivo* varies between synthetic and contractile[12]. When first explanted, cells will be in a contractile phenotype, which is specialized to contract in response to various chemical triggers. Exposure to fetal bovine serum (FBS), a standard reagent in cell culture to promote proliferation, will lead to a synthetic HASMc phenotype that proliferates and secretes ECM components[46]. While synthetic phenotype adapts well in cultures, forcing HASMc cells to adopt a contractile phenotype is necessary to study their function and various roles in airway dysfunctions.

Synthetic phenotype HASMc is more secretory and has reduced or nonexistent response to *bronchoconstrictors* such as histamine, with corresponding drops in the cytoskeletal proteins necessary for contraction. In synthetic phenotypes, concentrations of all of the proteins present in the actin and myosin filaments are diminished by as much as 75%, particularly Alpha- and Gamma- actin, heavy chain myosin (MHC), myosin light chain (MLC), myosin light chain kinase (MLCK), and calponin[47]. Actin and myosin isoforms that are not associated with contractility, such as Beta-actin, increase in concentration, leaving the overall concentrations of actin and myosin roughly the same[12]. Synthetic vascular smooth muscle phenotypes have been associated with proliferation, migration, and tissue repair *in vivo* [48], but synthetic HASMc phenotypes are not expected to form the majority of the population in healthy or even remodelled airway tissues. This “population inversion” has prevented *in vitro* studies from investigating some of the major elements of airway remodeling and contraction alterations in disease states.

Table 1.1 summarizes the differences in phenotype expression between contractile and synthetic HASMcs.

Table 1.1: Indicators of contractile and synthetic phenotypes

Phenotype	Upregulated Proteins	Characteristic Behaviors
Contractile	Alpha-SM actin, MHC, calponin, desmin, MLC, MLCK, Beta-tropomyosin, <i>h</i> -caldesmon	Histamine-responsive contractions
Synthetic	Beta-actin	Secretory Proliferative

Synthetic phenotype HASMCs will proliferate faster and more readily than contractile HASMC [17], although HASMCs can regain contractile phenotype depending on the number of culture passages (successive generations of *in vitro* cell culture) that have taken place[12]. When reaching confluence, cultures tend to produce a ‘hill and valley’ pattern and increasingly exhibit contractile phenotype[12], whereas synthetic phenotypes are encouraged by lower cell seeding densities and more passaging. Removal of FBS from the culture has been shown to influence adoption of a more contractile phenotype in canine ASM[46]. Exposure to IL-13 has been used to produce histamine-responsive ASM[49]. Contractile phenotypes can also be influenced using substrate stiffness[50] and tensile strain[51].

1.3.5 Tissue Engineering HASMC Studies

Given the importance of characterizing how ASM responds to strain, and the difficulties involved in obtaining contractile phenotype ASM, numerous models have explored how biomechanical factors affect ASM differentiation. Cells cultured on rubber substrates subjected to cyclic stretch have been used to assess ASM response to tidal strain for 20 years. Methods of stretching individual cells have been employed since 2005, with markedly different changes to the cytoskeleton than those noticed in the rubber substrate bioreactor experiments. Other investigations have focused on using 3D gel or tissue scaffold cultures to replicate the ECM conditions the cells reside in *in vivo* or culturing tissue-engineered models of complete bronchioles *in vitro*.

Bioreactors have been used to characterize ASM responses via mechanical strain of single cells, primary cultures and *ex vivo* smooth muscle sections in various substrates and in co-culture with other cell types. Cells are seeded onto a rubber substrate coated with collagen or another ECM protein that enables cellular adhesion and the substrate is then stretched cyclically at a frequency approximating that of respiration. Rubber substrates coated with HASMcs have been strained using FlexCell® bioreactors, resulting in realignment and MLC/MLCK expression[13] in regions of uniaxial strain, as illustrated in Figure 1.5. Later methods employing different bioreactors with larger regions of uniaxial strain found the same MLC/MLCK expression and realignment[52]. Cells did not respond in regions undergoing biaxial strain.

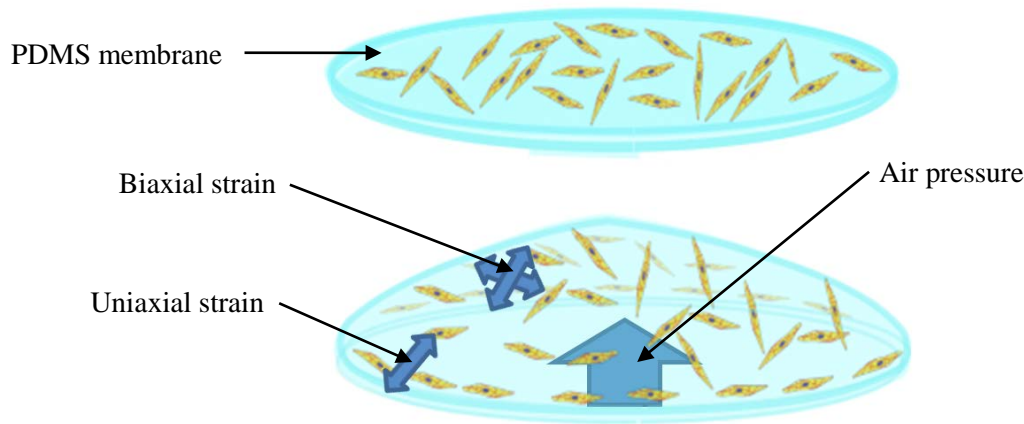


Figure 1.5: Illustration of uniaxial and biaxial strain across a pneumatically actuated well. HASMcs realign perpendicular to uniaxial strain and do not respond to biaxial strain.

Later experiments showed that these changes corresponded to changes in the speed of contraction when exposed to KCl, indicating that contractile speed, one potential hallmark of an asthmatic or hyper-responsive airway, had increased[52], although the stiffness of the cells decreased[13]. Increasingly uniaxial strain fields are thought to resemble the strain regimes found in asthmatic airways, compared to more biaxial strains found in healthy airway tissue[53]. Controlling the cell alignment relative to the axis of principal strain in uniaxial-strain bioreactor experiments produced similar results[54], however, Alpha-SM actin concentrations were unaffected[55]. Maksym *et al.* noted in 2005 that none of these

experiments included cell cultures exposed to static strain [13], in which the substrate is left in a stretched position, as a control in comparison to time-varying strain fields.

Later experiments have added neighboring cell types such as epithelial and fibroblast cells[56] and alternative substrates such as electrospun (ES) scaffold[57] or collagen-based hydrogels[58]. Other groups were able to produce cells with increased actin concentrations by enforcing parallel cellular alignment relative to the strain stimulus, generally by using photolithographically patterned substrates that prevented the cells from realigning [54], although this experiment was conducted on fibroblasts rather than smooth muscle cells.

The response of airway smooth muscle cells to mechanical strain has also been characterized by subjecting individual cells to cyclic forces, with contrasting results in comparison to the rubber membrane bioreactor experiments. In this set of experiments, magnetic microbeads were bonded to cell membranes and then subjected to a time-varying magnetic field such that the beads exerted torques on the cells, subjecting the portions of the cellular membrane adhered to the microbead to mechanical stress. These experiments showed cytoskeletal reorganization, increases in cell stiffness, and upregulation of Alpha-SM actin[53] within the vicinity of the bead. These experiments produced markedly different, and arguably more contractile, cells than the bioreactor experiments conducted using pneumatically-actuated membranes described earlier.

Various 3D cultures and tissue scaffolds have also been employed, since substrates with different morphology or stiffness could affect cellular response or how strain is propagated into the cells. West *et al.* cultured HASMc and HASMc-fibroblast co-cultures in collagen gel droplets on piezoelectric microlevers and found that although the gels underwent *compaction* in which rapid ECM overturn by the cells results in catastrophic reduction in substrate volume and the droplets detached from the piezo levers in less than 5 days, significant actin upregulation and histamine responsiveness was measured prior to failure[59].

Other groups have produced gel tissue cultures meant to replicate bronchiole physiology; Tseng *et al.* used magnetic levitation to produce organized layers of epithelium, ECM/fibroblast cells and airway smooth muscle, a co-culture which over a 7-day lifespan was found to have better regulated mucous expression and improved ECM turnover compared to single-tissue cultures [56], although improvements in contractile function were not reported. HASMCs on electrospun fibres were found to align with the fibres and secrete actin, calponin, and desmin, suggesting that more actin-myosin filaments were produced[57]. Human intestinal smooth muscle (HISM) cells have been cultured on electrospun polycaprolactane (PCL) scaffolds and exposed to strain using a stepper motor[58], but did not result in different phenotype from the unstrained scaffold; the cells may not have been subjected to cyclic strain at all as a result of plastic deformation and tearing of the substrate due to its low tensile strength.

To summarize, mechanical strain and the mechanical properties of the substrate have both been extensively modified over numerous studies in various attempts to induce a more contractile HASMC phenotype. Cyclic mechanical strain of rubber substrates alters MLC/MLCK expression, but cell stiffness decreases and other contractile phenotype biomarkers are unaffected. In contrast, cyclic mechanical strain of single cells via direct application of time-varying forces on the cells leads to changes in measured cell stiffness, reorganization of the cytoskeleton, and altered Alpha-SM actin expression, as does cyclic mechanical strain of rubber substrates featured with microgrooves. 3D gel cultures and tissue scaffolds have also been reported to alter contractile biomarker expression. How the strain stimulus is imparted to the cells appears to strongly affect their response; if the cells can realign, they do so while upregulating MLC and MLCK and decreasing in stiffness, whereas other substrates in which the cells are differently adhered or in which the cellular alignment to strain is enforced results in actin expression and in some cases increases in cell stiffness. As well, collagen gel or electrospun material substrates themselves lead to adoption of at least some contractile phenotype biomarkers.

1.4 Literature Review Summary

Asthma and COPD become increasingly difficult to treat and increasingly dangerous for the patient due to airway remodeling, in which the airway wall becomes stiffer and more capable of contraction. Human airway smooth muscle tissues are known to play a role in this process and are the component of the airway that exerts forces on the surrounding tissues in order to contract and narrow. Understanding and reproducing *in vitro* the biomechanical conditions HASM is under *in vivo* could provide invaluable information. Unfortunately, HASMc phenotype becomes increasingly synthetic *in vitro* and loses the contractile function that is required for proper study. For 20 years, researchers have relied on bioreactors as one of several tools to encourage contractile phenotype. Various bioreactors have been built; HASMcs have been subjected to strain as intact monolayers on various flexible rubber sheets, individual cells using magnetic microbeads or optical tweezers, or in ECM preparations or in entire airway sections *ex vivo*. Based on the literature review, the following experimental conditions led to expression of some aspect of the contractile phenotype:

1. **Substrate selection.** HASMc expression varies depending on substrate. When cultured on certain substrates, such as hydrogels or ES scaffolds, HASMcs show increased expression of proteins associated with contractile phenotype, particularly Alpha-SM actin[57], [59].
2. **Adhesion geometry.** How the substrate imparts strain onto the cells, and how the cells are allowed to respond to the stimulus, affects the result. In experiments in which cellular alignment was not controlled relative to the principal axis of strain, the cells realigned perpendicular to the strain and expressed MLC/MLCK, changing how cellular contraction was mediated. In experiments in which cellular alignment relative to the strain stimulus was controlled, or in which the cells were strained by actuators linked directly to individual cells, cells expressed Alpha-SM actin[54], [55].
3. **Strain waveform.** Smooth muscle tissues have a complicated response to mechanical strain based on *ex vivo* and *in vitro* experiments[52]. Cells can ‘reset’ their strain response when

subjected to higher strains, as observed in *ex vivo* experiments[40]. Imparting specific waveforms onto ASM cells and tissues may be a useful experimental variable, particularly by providing a more realistic approximation of respiratory strains than a purely sinusoidal signal.

4. **Strain field pattern.** The strain anisotropy to which cells have been exposed affects differentiation[55]; uniaxial strains produce realignment and provoke a more contractile HASMc phenotype than biaxial strains. In asthma, the topic has physiological relevance: strain fields are thought to be less biaxial in asthmatic airways than in normal ones[60].

The different phenotype expressions resulting from different substrates, cytokines, and mechanical strain regimes are summarized in Table 1.2. Some related cell types, such as airway wall fibroblasts or intestinal smooth muscle cells (ISMcs), have also been exposed to cyclic mechanical strain; as those experimental results may still be relevant, they are included with the cell types in brackets.

Table 1.2: Cell response to various experimental conditions

Experimental Condition	Response
Unstrained, glass/plastic	Synthetic phenotype
Strained rubber	MLC/MLCK upregulation, cell realignment[55]
Strained rubber, aligned cells	Alpha-SM actin (fibroblast cells), no realignment[54]
Strain of individual cells	Alpha-SM actin[55]
Culture on aligned ES scaffold	Alpha-SM actin, calponin, desmin[57]
Strain on ES materials	Negligible difference to unstrained (intestinal SM), issues with plastic deformation of substrate[58]
Strain in collagen gel droplets	Cell and tissue-level reorganization, Alpha-SM actin (fibroblast cells), histamine response, compaction after 3 days[59]
IL-13 exposure	Histamine response[49]

2 Bioreactor Design and Implementation

Based on the literature review in Chapter 1, a bioreactor that imparts respiratory strain waveforms onto a substrate would benefit from the following design elements:

1. **‘Meso-scale’ Bioreactor.** The Dorscheid and Walus labs both produce and rely on tissue cultures that fit the standard 6 to 24-well plates regularly used in biology (~30 mm to 6 mm diameter). Bioreactor options need to be compatible with these cultures.
2. **Displacement-based actuators.** ASM behavior is generally thought to vary as a function of strain, not stress[39]. The strain of the substrate needs to be controlled directly through a variable-displacement actuator, as opposed to a variable-force actuator that would only indirectly control the strain and would require more complicated closed-loop control for proscribed displacement to occur each strain cycle.
3. **Arbitrarily programmable actuator motion.** Mimicking a gradual increase in airway stiffness by gradually increasing static strain while decreasing cyclic strain amplitude, or adding occasional high-amplitude waves meant to imitate deep inhalations, may provide useful experimental conditions. Electrospun materials and hydrogels may undergo plastic deformation or weakening as the experiment proceeds and this may be compensated for by adjusting the equilibrium position of the actuator. The most flexible approach is the use of an actuator that can produce any programmatically defined waveform within a feasible motion bandwidth.
4. **Strain characterization method.** It would be preferable to be able to characterize the experimental conditions experienced by the cells to validate the apparatus and implementation.

The bioreactor design will need to account for how strain is distributed across the rubber substrate, include a control system able to impart motion waveforms to what may eventually be an arbitrary number of actuators, mitigate environmental hazards to the cells and actuators, and characterize the strain across the rubber substrate.

The cells are subjected to strain via deformation of a polydimethylsiloxane (PDMS) substrate (a form of biocompatible rubber), and the strain across the surface will need to be modeled to determine the necessary range and force output of the actuators. An actuator and controller capable of fulfilling the project requirements must be designed and implemented. Depending on the actuator, an enclosure will be needed to minimize heat emission into the incubator and to protect the actuators from humidity, disinfection agents, or contamination. Lastly, most bioreactor experiments lack a method of validating the strains across the membrane surface; prior investigations generally relied on modeling[60] or actuation methods which were assumed to repeatably produce planar strain[61]. While 2D digital image correlation (DIC) methods have been widely used for strain characterization, there are no methods previously reported in the literature that allow 3D DIC to be performed without specialized optical equipment. Characterizing non-planar strains requires characterizing variations in height across the substrate in addition to 2D strain characterization.

2.1 Modeling Of Strain Across a Hyperelastic Substrate

Since the pattern and magnitude of strain on rubber membranes is thought to affect contractile cytoskeletal components and phenotype as previously discussed, strain patterns in various loading conditions were modeled. Prior studies have concluded uniaxial and biaxial strain affects HASMc differentiation differently [55], and varying patterns of strain have been used in bioreactor experiments both to enable microscopy during stretch [62] and as experimental variables[63]. Biaxial and uniaxial strains are often referred to in the literature, generally to describe the degree of anisotropy in radially symmetric or *axisymmetric* strain patterns. The strain across an axisymmetrically loaded membrane is best described using radial and circumferential coordinates, which are depicted below in Figure 2.1.

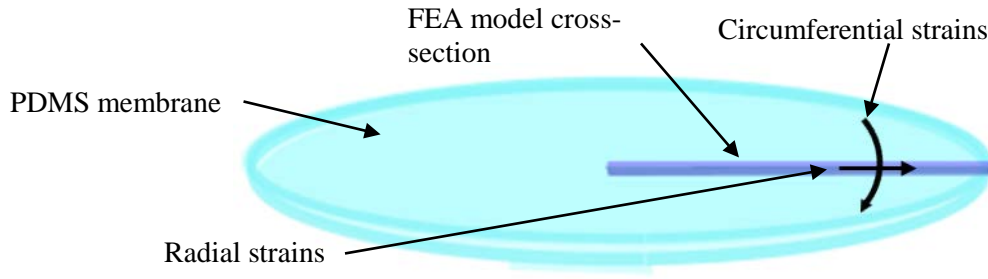


Figure 2.1: Illustration of radial, and circumferential strain fields across a radial cross-section.

In HASMc studies, HASMc realignment was first noted on vacuum-loaded Flexcell membranes along the edges of the well[60]. Two other straightforward methods of straining these membranes would be to use air pressure on the bottom of the well or actuator-driven displacement of a plunger. These three alternate strain methods were modeled in Comsol[64], finite element analysis (FEA) software. Since the circular membrane is fixed around its edges and deformed from the centre, a 2D axisymmetric model was used. The PDMS substrate was modeled as a *hyperelastic* material, as discussed below.

Unlike linear elastic materials, elastomeric materials such as rubber or PDMS can be stretched to well over 100% of their original length without undergoing plastic deformation and produce a nonlinear stress-strain response, particularly for larger strains. Hyperelastic material models such as Ogden, Yeoh, or Mooney-Rivlin[65] derive stress from a strain energy density function which is defined differently depending on the model.

To review basic continuum mechanics and to explain how hyperelastic stress-strain models are defined in contrast to linear elastic materials, a linear stress-strain response is shown in Figure 2.2 below. This stress-strain response occurs in elastic materials for small strains, such as metals and some polymer materials such as polycarbonate or acrylic.

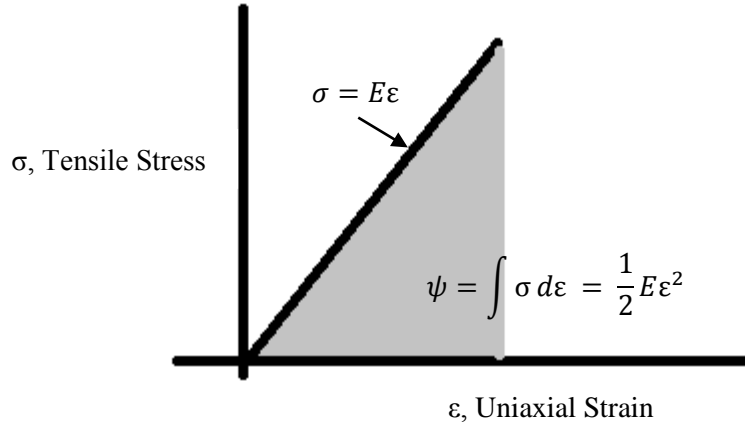


Figure 2.2 Relationship between the stress on a substrate, the strain across the substrate, and the strain energy function of the substrate for a linear elastic stress-strain response.

The area under the curve is the energy stored by the material per unit volume and is the integral of stress as a function of strain. For elastic materials undergoing small strains, the stress-strain response is linear: $\sigma = E\epsilon$, where E , the modulus of elasticity, is a constant, σ is the stress across that region, and ϵ is the strain across that region. It follows via either integral calculus (or basic geometry in this simpler case) that the area under the graph, ψ , the strain energy density per unit volume, is

$$\psi = \int \sigma d\epsilon = \frac{1}{2} E \epsilon^2 \quad (2.1)$$

For the Ogden model of hyperelastic material response, ψ is not linear and instead a polynomial function[66] is used:

$$\psi = \sum_{i=1}^N \frac{2\mu_i}{a_i^2} (\bar{\lambda}_1^{a_i} + \bar{\lambda}_2^{a_i} + \bar{\lambda}_3^{a_i} - 3) + \sum_{i=1}^N \frac{1}{D_i} (J_{el} - 1)^{2i} \quad (2.2)$$

where μ_i and a_i must be derived via materials testing, $\bar{\lambda}_1, \bar{\lambda}_2$, and $\bar{\lambda}_3$ are the principal strains, D_i relates the compressibility of the material, and J_{el} is the elastic deformation per unit volume. The stress can then be derived as a function of strain using this strain energy function. A more rigorous derivation of continuum mechanics and hyperelastic strain models is out of scope for this thesis but can be found elsewhere[67],[68]. The coefficients used in the modelling presented here were derived empirically by

another team using uniaxial strain tests for Sylgard 184 PDMS[69]. Coefficients derived using *equibiaxial* strain tests, in which the substrate is uniformly subjected to two-dimensional strain, may be more reliable, but were not available. Variations can also be expected due to differences in the brand of PDMS used and curing time.

Table 2.1: Ogden parameters for modeling of hyperelastic response of PDMS

Ogden Parameter	Value
μ_1	63.4885 MPa
μ_2	.041103 MPa
a_1	6.371×10^{-10}
a_2	3.81166

FEA software was used to model a 3D volume of PDMS undergoing a deformation derived using the Ogden model parameters discussed above. The axisymmetric deformations allow it to be modeled as a 2D axisymmetric model, in which the FEA software models the strain along a radial cross-section of the membrane, as shown in Figure 2.3.

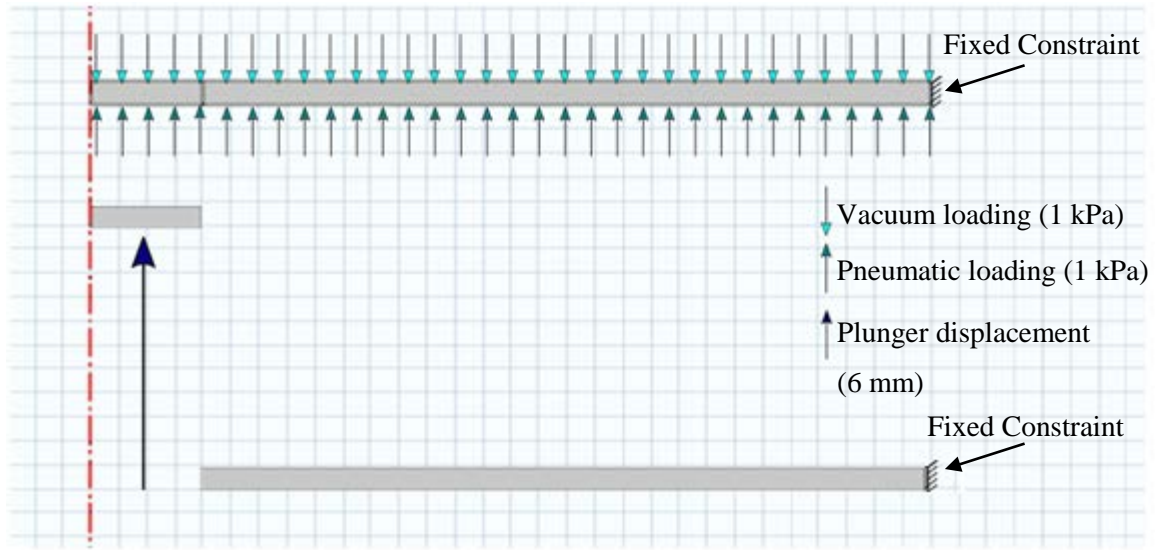


Figure 2.3: Alternative models using pneumatic and plunger loading of the PDMS membrane in the axisymmetric FEA models. In the pneumatic and vacuum loading simulations, pressure is distributed uniformly across the PDMS surface. In the plunger loading simulation, the centre of the cross-section ($r \leq 2$ mm) is displaced by the peak amplitude of the air pressure loading (6 mm).

The PDMS was modeled as incompressible; rather than relying on a Poisson's ratio asymptotically close to 0.5 to approximate incompressibility, which can impact model accuracy, Comsol can avoid locking or stiff results by employing a mixed formulation in which pressure is treated as an extra degree of freedom during simulations.

The FEA analyses do not include the following conditions:

- Hysteresis during unloading could result in varying strain magnitudes, or even gradients, across the surface. It was assumed there was no hysteresis between strain cycles.
- PDMS fatigues and changes in material response over time, due to accumulated loading cycles, or because of other factors. This degradation was ignored.
- Clamping conditions were assumed to be uniform along the edges of the membrane. In practice, clamping conditions may vary around the perimeter and there may be corresponding variations in conditions and experimental results near the edge of the membrane. These edge conditions may produce varying or unpredictable strain results.

- Stick-slip and friction between the plunger surface and the membrane have not been modeled.
- The real strain conditions will not be axisymmetric. For example, the plunger will not be perfectly centred on the membrane or the extent to which the membrane edge has been fixed in place may vary across its circumference.

Comsol model results are depicted in Figure 2.4. Modeling of the conditions in the vacuum and plunger driven wells used in other experiments qualitatively agreed with analyses reported elsewhere [60].

Pressure in the pneumatic/vacuum simulation was set to deflect the membrane to a maximum of 6 mm in height. The actuation forces applied to the pneumatic and plunger-driven models were set such that the deflections in both cases were 6 mm at most.

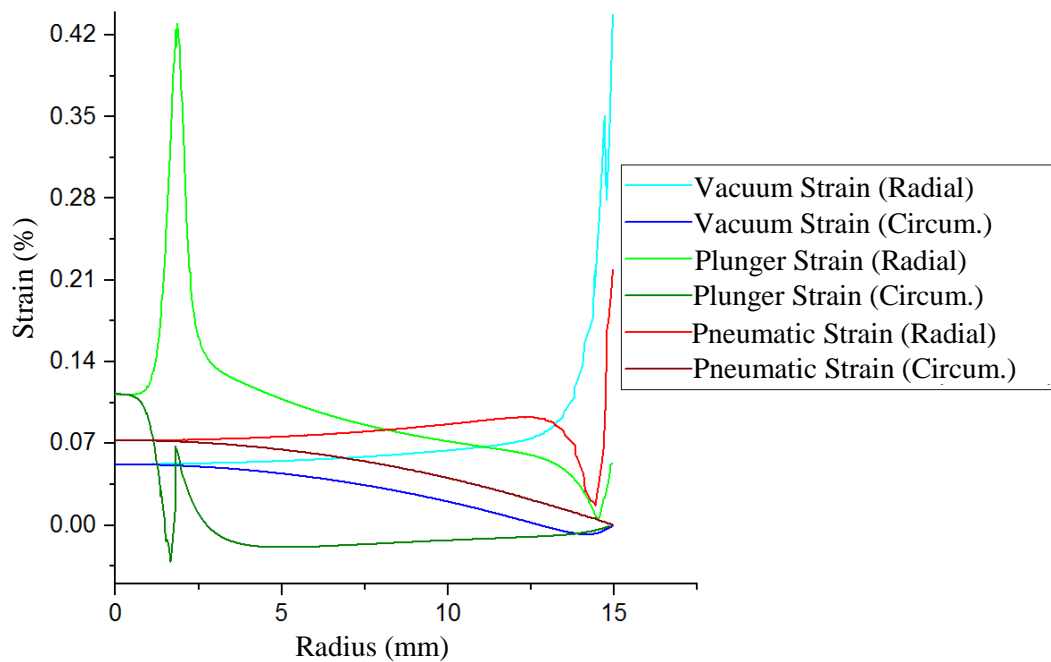


Figure 2.4: Radial and circumferential strains as a function of radius when deflected by pneumatic or plunger loading. Air pressure to produce the vacuum or pneumatic strains was 1 kPa. The plunger load was modeled using a prescribed displacement of the centre of the membrane (2 mm radius). Amplitude of the displacement was equal to the peak amplitude of the pneumatic load (6 mm).

Based on these simulations, the strain near the centre of a pneumatically-deflected membrane is biaxial and becomes increasingly radial toward the edges, with an asymptotic strain near the edge of the

membrane. Although experimental results will vary from the model due to nonideal boundary conditions ('edge effects'), the strain concentrations near the edge of a fixed boundary are a realistic result. The strain produced by a plunger mechanism is highly uniaxial across the membrane, in contrast with the biaxial strain conditions across the pneumatically-loaded membrane, with a strain peak near the edge of the plunger mechanism. As uniaxial strain conditions have been associated with changes in cellular behavior, at least when the cells are seeded directly onto PDMS, uniaxial strain conditions would be employed to test the effects of the bioreactor on cells.

To analyze the sensitivity of the plunger method to different experimental implementations, the membrane thickness and plunger width were varied.

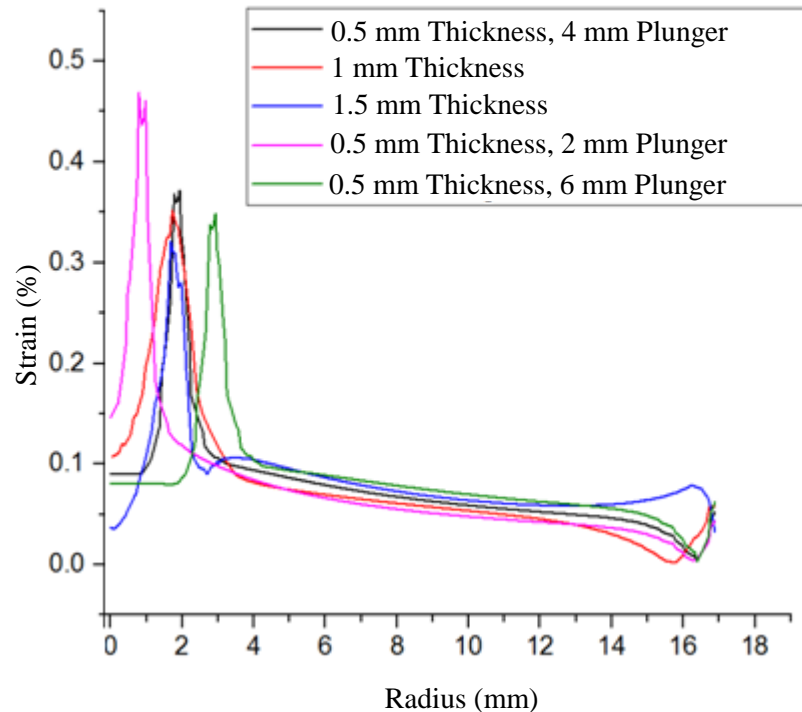


Figure 2.5: Strain profiles as a result of varying the plunger width and membrane thickness.

Peak height and, to a lesser extent, width, varies as a function of membrane thickness. Varying the plunger width moves the strain concentration occurring at the boundary between the edge of the plunger and the rest of the membrane. The plunger would employ a rounded tip (not pictured), which would

attenuate the strain concentration noted in the FEA models and better distribute strain across the PDMS membrane.

Parametric sweeps of membrane thickness were also performed to determine force requirements for the actuator as a function of peak deflection of the membrane, and are shown in Figure 2.6. These will be discussed in Section 2.2.2.

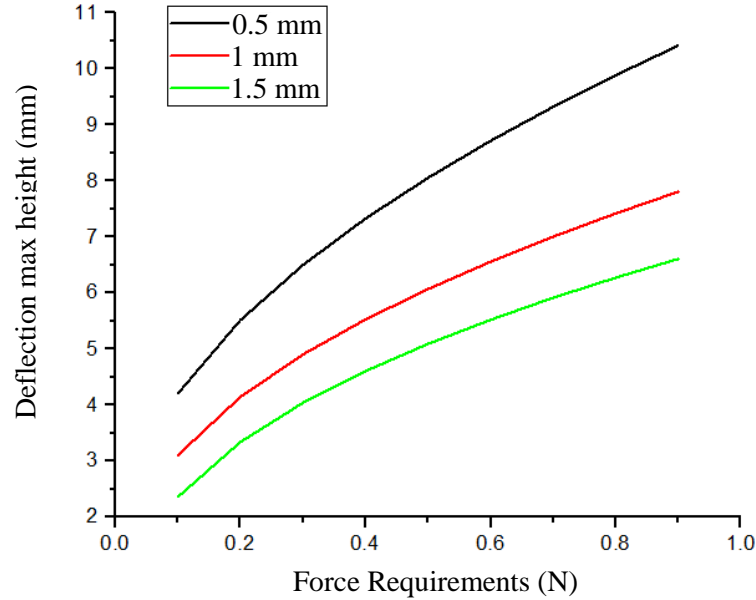


Figure 2.6: Membrane deflection versus force for membranes varying in thickness from 0.5 mm to 1.5 mm.

In conclusion, strain across the PDMS membrane can be estimated using a hyperelastic 2D axisymmetric FEA model. Pneumatic deflection using air or vacuum results in highly biaxial strain near the centre of the well, with increasingly radial strain further from the centre. Plunger deflection results in highly uniaxial strain across most of the well. Edge conditions will affect experimental repeatability near the fixed edge of the membrane. Lastly, parametric sweeps across membrane thickness have been used to obtain force estimates for actuator selection.

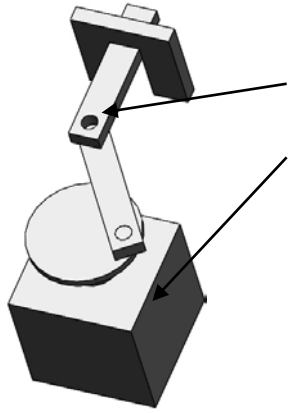
2.2 Actuator Selection

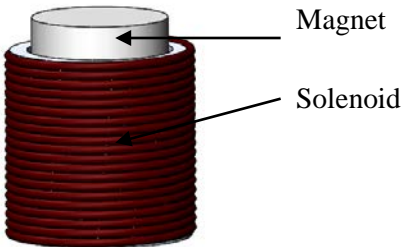
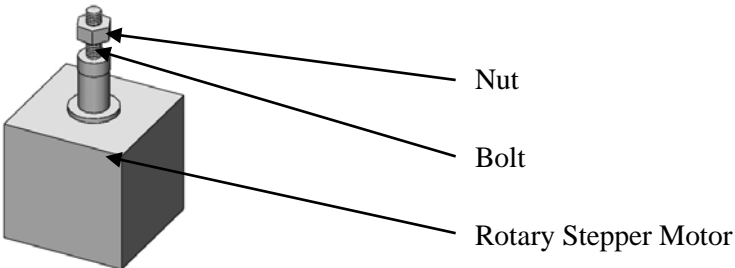
As described at the beginning of this chapter, actuators should be capable of displacement-controlled motion and arbitrary waveforms. Ideally, they should also be controlled in open loop, simplifying the control issues for running several wells simultaneously. Various actuators have been reported in bioreactor publications, as well as various schemes to use one actuator to drive several cultures[70]. Stepper motors were selected for the bioreactor design discussed in this thesis after assessing the selection available based on prior bioreactor designs. Initial control systems used an Arduino™ board and Sparkfun™ stepper drivers. When scaling up to a 6-well bioreactor array, the few motors that could be procured for the experiments used motor-specific driver boards and an STM32®[71] board programmed to output arbitrarily-shaped waveforms was used. The motors were noted to add confounding variables to the experiment, namely heat emissions and vibration. These issues are discussed in Sections 2.2.3 and 2.3.

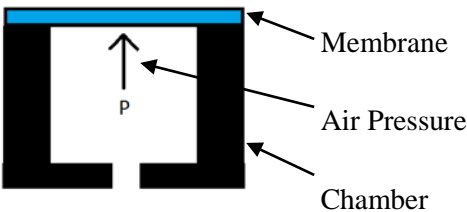
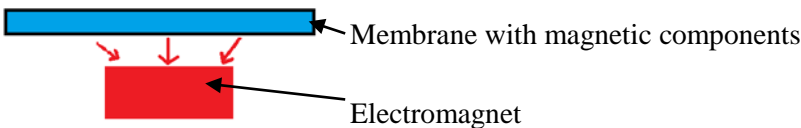
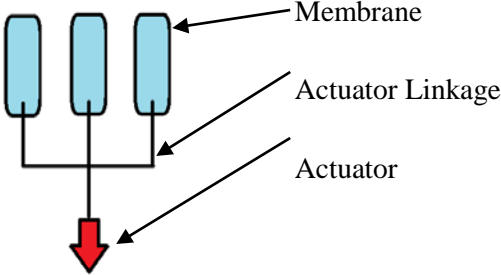
2.2.1 Actuator Options And Prior Art

Table 2.2 schematically depicts various actuator options that have been used in the past.

Table 2.2: Depiction and description of different actuators in prior art.

Actuator	Schematic		
Reciprocating motor[72]	 <p>Actuator linkage for reciprocating linear motion</p> <p>Rotary motor</p>		
	Description	Advantages	Disadvantages
	<ul style="list-style-type: none"> •Constant-V motor •Cyclic linear motion via mechanical coupling. •Example: camshaft. 	<ul style="list-style-type: none"> •DC current – simple control. 	<ul style="list-style-type: none"> •Static strain is not adjustable •Potentially complex mechanical system

Actuator	Schematic		
Voice coil actuator[73]			
	Description	Advantages	Disadvantages
	<ul style="list-style-type: none"> •Concentric solenoid/magnet 	<ul style="list-style-type: none"> •<1 μm positioning accuracy •kHz scale motion bandwidth •No wear 	<ul style="list-style-type: none"> •Higher power draw than stepper motor •Closed-loop control
Actuator	Schematic		
Stepper motor-driven linear actuator[74]			
	Description	Advantages	Disadvantages
	<ul style="list-style-type: none"> •Rotary motor and lead screw 	<ul style="list-style-type: none"> •Open-loop control •High accuracy. 	<ul style="list-style-type: none"> •Wear •Complicated mechanical system

Actuator	Schematic		
Pneumatic drive[75]			
	Description	Advantages	Disadvantages
	<ul style="list-style-type: none"> •Membrane deformed via air pressure 	<ul style="list-style-type: none"> •No wear •Little heat •Fewer hazardous parts 	<ul style="list-style-type: none"> •Closed-loop control •<10 Hz motion bandwidth
Actuator	Schematic		
<i>In-situ</i> magnet drive[76]			
	Description	Advantages	Disadvantages
	<ul style="list-style-type: none"> •Magnet embedded in membrane, pulled by electromagnet 	<ul style="list-style-type: none"> •No wear •Actuator integrated into substrate 	<ul style="list-style-type: none"> •Heat output •Nonlinear response
Actuator	Schematic		
Multi-well-driving actuator[70]			
	Description	Advantages	Disadvantages
	<ul style="list-style-type: none"> •Single actuator displaces n wells 	<ul style="list-style-type: none"> •Single actuator •Simpler control system 	<ul style="list-style-type: none"> •Complicated actuator/well linkage design

2.2.2 Selection Constraints

Actuator selection is limited by various constraints, particularly the mechanics of airway stretch as discussed in Chapter 1 and the potential need to replicate similar prior work in the literature using the device discussed in this thesis. The maximum possible stretch in a well is defined by actuator range. The actuator speed and bandwidth should be sufficient to exert typical respiratory frequencies and waveforms on cultures. Force requirements are more difficult to define given the wide range of different potential substrates, but minimum limits can be set based on the forces required for stretching PDMS membranes. Positioning resolution is of low concern, as it would affect experimental repeatability and the resolution to which static strains can be imposed on the substrate, but not the feasibility of repeating prior work in the literature.

Maximum range was based on well size and an approximate estimate of largest possible strain required. As discussed in Chapter 1.3.1, *ex vivo* models have found airways undergo strains of about 10% of unstrained luminal diameter when subjected to physiologically relevant conditions[39] and prior *in vitro* bioreactor experiments have employed strains between 15-30% to affect MLC/MLCK expression[60] (this discrepancy has been noted previously[30]). Based on this, an actuator capable of producing 40% strain in 6-well-plate-sized substrates is ideal and the minimum stretch range for any actuator is 10%. Using a 6-well-plate size and estimates obtained using FEA modeling, actuators require a maximum range of about 10 mm.

The actuator bandwidth should span 0.2-6 Hz; 0.2 Hz at minimum to produce sinusoidal strains at roughly the usual respiratory rate and 6 Hz to produce waveforms matching those *in situ*. ASM cells *in situ* would reasonably be expected to experience strain cycles at a frequency of 0.5 Hz or less, given that respiratory rates exceeding 16 breaths per minute (~0.7 Hz) are indicative of hyperventilation[77]. Note that other tissues have been shown to respond to markedly different frequencies; heart cells will be exposed to cyclic strains at roughly ~4 Hz (240 BPM)[78] at most and *in vitro* experiments on bone marrow stem cells have demonstrated altered differentiation for 1 and 100 Hz cyclic strain

frequencies[79]. Waveform bandwidth constraints are drawn from research on lung pressure waveforms, which showed that a bandwidth of 6 Hz[80] is necessary.

Based on the range and bandwidth estimates, the actuator must be capable of travel at speeds faster than 4 mm/s and never faster than 40 mm/s, depending on experimental conditions. At 1 Hz frequency and a ~40% strain amplitude (~1 cm peak amplitude in the largest plate size), a maximum speed of roughly 20 mm/s is necessary. Experiments would still be possible at a strain cycle of 0.2 Hz, mimicking regular breathing rates (~10 breaths/minute) with an actuator speed of 4 mm/s. Maximum speed requirement of the actuator will be 4 to 40mm/s.

The actuator must generate sufficient force to deform the membrane and cell culture. It is assumed the actuator will be axisymmetrically deforming a membrane of at most 2 mm thickness, to approximate the force requirements of alternate substrates or tissue models. Bioreactor wells are assumed to be 6-well-plate sized (~15 mm radius). The minimum force the actuator must generate is roughly the force required to displace the membrane 10 mm which, based on Figure 2.6, is approximately 1 N.

Range, force, and speed requirements are summarized in Table 2.3 below. Resolution was determined to be of relatively low priority, so it is not included.

Table 2.3: Actuator selection requirements.

Requirement	Minimum Acceptable Value
Range	1 cm
Force	1 N
Speed	4-40mm/s
Bandwidth	6 Hz

2.2.3 Implementation

Based on the above criteria, stepper motors with lead screws were determined to be the best actuator choice. In contrast with standard motors, where speed is controlled, stepper motors produce motion by

moving through a discrete series of uniformly-sized steps with a given stepping resolution. Stepper motors have the following advantages for driving actuators for bioreactor experiments:

1. Open-loop, programmable motion.
2. Relatively arbitrary range. Velocity, force output, and stepping resolution (generally $<100\text{ }\mu\text{m}$) were all well within the desired constraints.
3. Small sizes are available, suitable for single well actuators.

Motors were sourced as salvage from UBC Rapid, a student team which builds 3D printers.

Following research on stepper motor options, Haydon-Kerk linear actuators were determined to fit the requirements discussed previously; Canstack actuators[81] have a built-in lead screw and nut, removing some of the difficulties involved in building a linear actuator. Several Canstack motors of varying size, shape and functionality were received as donations from UBC Rapid. Later, design revisions for a 6-well stepper motor-driven bioreactor relied on 10 5-phase ‘Vexta’ stepper motors, also obtained as donations from UBC Rapid. The procured motors all required some method of linear bearing/angular lock so that the nut could not rotate relative to the lead screw. The two solutions used are depicted in Figure 2.7 and Figure 2.8.

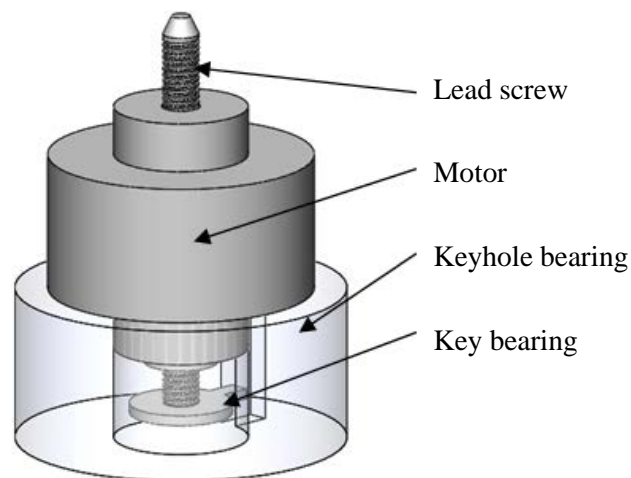


Figure 2.7: Linear stepper motor with keyhole bearing.

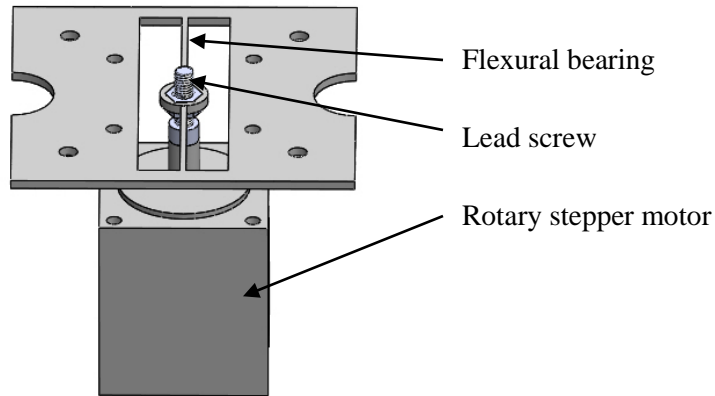


Figure 2.8: Rotary stepper motor with flexural bearing.

Motor parts were either epoxied onto the stepper motor parts or pressure-fitted by designing the rapid-prototyped (RP) parts with mating holes for motor features which were approximately 0.1 mm smaller in diameter than the feature, allowing the parts to be forced together using a vice. Heat shrink tubing and epoxy were used to attach M3 machine bolts to the shafts of the Vexta motors using a lathe to clamp and align the components; microscopy verified that the machine bolt was aligned to the centre of rotation to better than 1 degree. ‘Blue Goop™’ lubricant was used to lubricate the shafts to minimize brinelling or wear during motion.

The shaft/key lock mechanism caused the motor and screw to vibrate due to poor tolerances; a 0.2 to 0.5 mm gap between each of the shaft and key features allowed the lead screw to vibrate back and forth approximately 3 to 5 degrees. Polycarbonate waterjet-cut (WJC) flexures prevented or minimized vibration, and were easily manufactured, but had a maximum travel of 10 mm, the flexure was too wide to accommodate a standard 6-well plate, and forces on the motor varied as a function of travel, which affected motor vibration and driving current requirements. Solidworks FEA modeling of the polycarbonate flexure suggested forces up to 2N were placed on the motor to a maximum travel of 5 mm before undergoing plastic deflection, as shown in Figure 2.8. As the flexure can travel 5 mm in either direction from equilibrium before it starts to plastically deform, the motion range requirements were met using this flexural bearing.

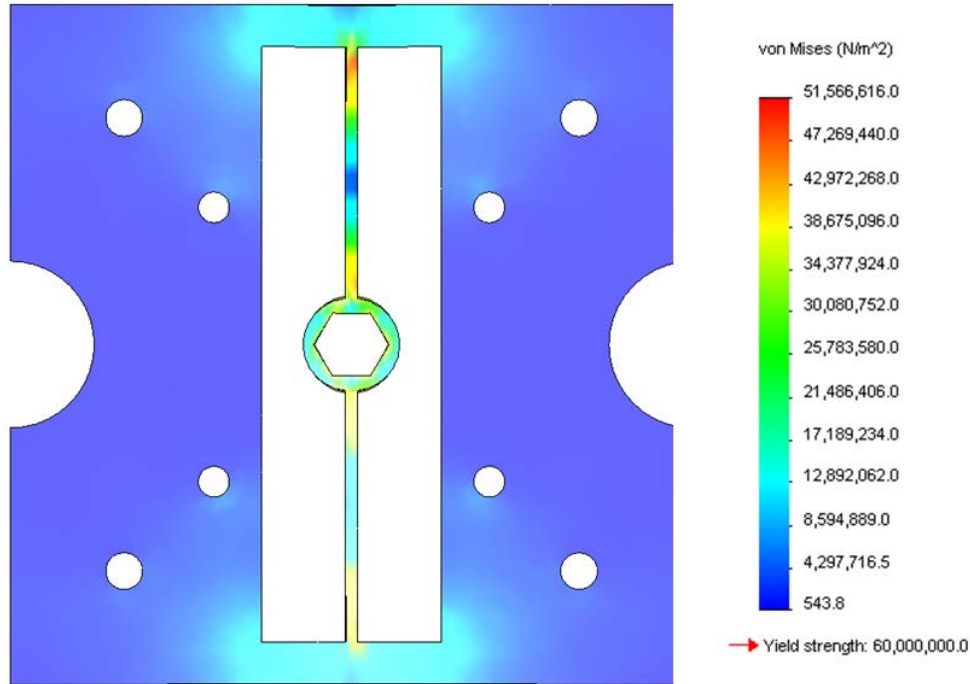


Figure 2.9: Solidworks linear elastic analysis of the flexure when the nut holder is at 5 mm deflection height. A force of 1.9 N results in a deflection 5 mm in height and stresses close to the ~62 MPa yield strength.

While the first linear actuators were being designed and tested, the vibratory noise generated by the motors was determined to be a design risk that could potentially affect experimental results. The effects of vibration on cells have been explored to some extent. Bone cells and bone cell progenitors are affected by 30-100 Hz vibrations[82]. Studies of vocal fold and laryngeal fibroblasts have also found that frequencies of 100+ Hz can result in increased ECM deposition [83],[84]. One dissertation has characterized the frequency response in pig tracheas and found that cell stiffness decreases as a function of frequency[85].

Stepper motors will generate vibration, although there are ways of mitigating this in both actuator design and implementation. Stepper motors generate motion by ‘stepping’ from one stable position to another, giving them excellent position resolution and repeatability in open loop. Depending on the current driving the motor and the load, damped harmonic oscillation occurs during this motion and the motor vibrates. This problem has been solved by either altering the arrangement of coils inside the motor[86] or by altering the stepping process to compensate for these oscillations[87]. The usual 2-phase stepper motors employ 8 coils arranged around the motor shaft, which are energized in a 4-step sequence,

requiring two electrical signals in order to do so. 5-phase motors energize 5 coils in a 10-step sequence, requiring 5 separate electrical channels. The 2-phase stepper motors will energize two coils at a time to produce motion, whereas the 5-phase motors energize either 4 or 5 coils at a time depending on the resolution settings. This 5-phase motor design produces motion and force more uniformly than standard steppers at the cost of more sophisticated control electronics and increased heat output; the 5-phase Vexta motors each have driver boards roughly of 4.9 cm², the size of a single Arduino microcontroller, and can generate over twice as much heat given the larger number of coils energized at a time. These motors required some improvements to the control electronics, as sudden start/stop motions led to dropped steps and it was necessary to implement a motor controller able to impart arbitrarily-shaped waveforms which provided smooth accelerations and decelerations. The alternative is to change the way the 2-phase motors are controlled by moving the motors in more incremental ‘microsteps’ which, when employed properly, can prevent the harmonic oscillations described earlier from occurring at the cost of decreased force output from the actuator and increased control system complexity.

There are other sources of vibration from a linear actuator, namely shaft eccentricity and any vibration emitted by the mechanism which translates rotary stepping motion into linear motion. Inside the motor, a misaligned shaft will result in lateral vibration proportional to the rotational speed; similarly, misalignment between the motor shaft and the mechanism attached to it can produce vibration within a similar bandwidth.

The potential for vibrations to affect experimental results has not been explored in prior bioreactor designs, including those reporting systems based on stepper motors. Numerous prior bioreactor designs have relied on stepper motors[74],[88] or other actuators that may generate higher-frequency vibrations during motion, but vibration generated by the actuator is generally not reported. Regardless, in the present work, steps were taken to measure the vibration created by the motors and actuators and to mitigate it. The motor vibration analysis is presented in Chapter 3.

In addition to dynamic strain, static strain across the well could also have an impact on cell phenotype. Static strain may be induced onto the culture by the actuator depending on the load range of the actuator and the effectiveness of the membrane clamping. Static strain may also be introduced via fatigue in the PDMS membrane after numerous loading cycles. To the best of the author's knowledge, static strain has not been explored as an experimental variable for HASMcs and has only been rarely discussed for other cell types[89]. While the airway wall may be statically loaded due to fibrosis and airway wall remodeling, and while this may affect the HASMcs, *in vitro* tests have focused on time-varying strains. A static strain control will be used in bioreactor experiments to determine the difference between HASMc response to a substrate with an anisotropic stress-strain field and an anisotropic time-varying strain stimulus.

Many bioreactors rely on motion control boards[74], although the project budget meant these options were not feasible. Initially, an Arduino®[90] microcontroller and Sparkfun® stepper drivers[91] were sufficient to drive the stepper motors. When the 2-phase Canstack® motors had to be replaced with 5-phase stepper motors, the complexity of the control system needed to increase. It was necessary to provide motion waveforms which accelerated and decelerated the motors smoothly to prevent missed steps and to minimize the driving current such that the heat emissions from the 5-phase motors would be manageable.

The initial prototypes used 2-phase stepper motors; an Arduino Mega microcontroller outputting square waves at constant frequency was sufficient to drive the motors. This was sufficient to expose cells to cyclic strain, although custom waveforms or different strain frequencies for each well would be impossible. With the Vexta motors, this control method resulted in dropped pulses and position drift unless the driver boards were set to 300 mA/phase, which increased the power draw to 12 W/actuator. This, in turn, would generate unacceptable amounts of heat inside the incubator unless a cooling system capable of removing up to 80 W of heat was implemented.

The next iteration of software and firmware needed to control 5-phase stepper motors from Oriental Motors required more sophisticated control methods and an upgrade to the control system to allow truly arbitrarily-defined motion waveforms. Arbitrary waveforms would be most easily generated by using a microcontroller which could output an arbitrary pulse series.

Figure 2.10 below depicts the process through which pulse train waveforms with acceptable acceleration are generated. Note that the stepping size of the hypothetical motor being driven in Figure 2.10 was set to 50 μm so that the viewer could discern the steps in the discretized waveform; the 5-phase motors had a stepping size of 0.5-1 μm depending on driver board settings. As an example, a waveform in which the amplitude of the peaks varied between simulated breaths was used to test the software, and in Chapter 3, to test the actuator.

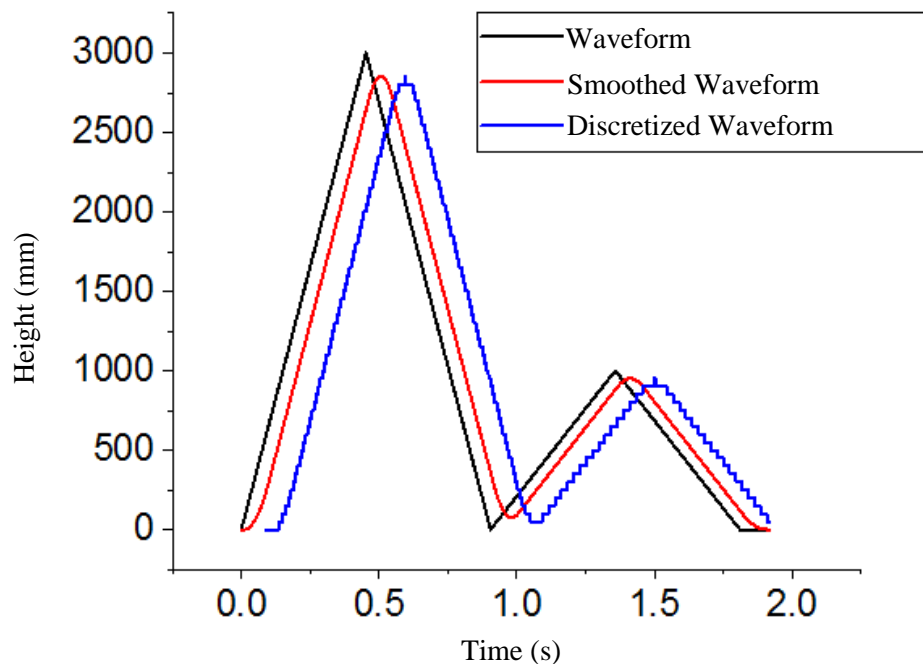


Figure 2.10: The initial, smoothed and discretized waveforms produced using the motor controller Matlab code. The initial motion waveform was formatted via a Matlab script producing a linear waveform ('Waveform', black). The initial waveform was smoothed using a moving window average filter in Matlab to remove sudden start-stop motions which would generate very high acceleration/deceleration forces in the motors ('Smoothed Waveform', red). The smoothed waveform was then discretized in Matlab to the given stepping resolution to provide the individual control pulses to the stepper motor ('Discretized Waveform', blue). The waveform was then sent into the motor controller via UART where it is stored and repeated to provide the intended motion. The discretized waveform is offset on the graph by 0.2 seconds for clarity.

The motion waveform is generated in Matlab® by the user. A program smooths the waveform using a moving average filter, resulting in a filtered motion profile that limits the bandwidth of the signal and removes any sudden acceleration above the desired bandwidth. The program then discretizes the motion profile into a series of steps based on the user-input step size for the motor and produces a ‘step’ and ‘direction’ pulse series for each waveform, converts these pulse series into ASCII characters, and sends them to the microcontroller via UART. The microcontroller can then repeatedly output this waveform to the motors.

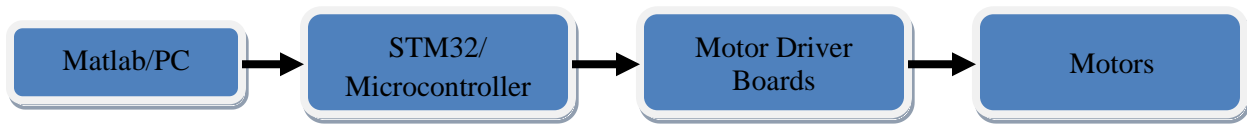


Figure 2.11: Control electronics block diagram.

To control a series of motors with an arbitrary motion control waveform, an STM32® ‘Discovery’ board was selected. The motor controller needs to store and output a waveform at least 2 seconds long with a bandwidth of 10 kHz, given the stepping size of the motors and the amplitudes and frequencies required to simulate tidal respiration. This requires at least one timer interrupt and at least 40 kB of RAM; the simplest coding implementations compressed poorly and ultimately required nearly 1 MB for 3 seconds of run time. The STM32® ‘Discovery’ board has a 180 MHz processor, 1 MB of RAM, 80 General Purpose Inputs/Outputs (GPIO), and 23 external and timer interrupts, is less expensive than the Arduino Mega board used during prototyping and allows for up to 4 separate experimental conditions to be carried out for over 10 seconds under the requisite bandwidth before memory space becomes an issue.

To validate the actuators and control system used in the bioreactors, actuator motion and vibratory emission are characterized in Chapter 3.

2.3 Enclosure Design

The actuators are vulnerable to contamination and generate heat; the cells need to be protected from the actuators and vice versa.

The actuators are regularly carried in and out of a tissue culturing room containing biologically hazardous materials, and are in direct contact with a well containing cell culture media and primary cells; any exposed surfaces need to be periodically disinfected with ethanol or bleach. The containment issues involved have led researchers to isolate the actuators from the cells using various enclosure designs[92], or to select or develop entirely new actuators that are not as vulnerable to corrosion and that simplify disinfection[76]. Actuators using air pressure[75] or electromagnets[76] can be easier to engineer to run inside an incubator, although any form of motion control becomes difficult and could require closed-loop control, particularly if the mechanical properties of the substrate under strain vary between or during experiments.

For the present work, experiments began with one-well prototypes (illustrated in Figure 2.12). Early experiments placed motors in plastic bags that were zipstrapped shut. The bags were pinned between the plunger head and either the PDMS membrane or a flexure that aligned the lead screw, compressed the bag and provided a restorative force that pinned the membrane against the actuator. The slack in the bag allowed it to act as a bellows diaphragm. Minute quantities of color-indicating dessicant inside the bag ensured that the motor was not subjected to damaging humidity from a poor seal and provided an indication if humid incubator air was leaking into the motor bag. The motors and wells were held in laser-cut acrylic stands. A major disadvantage of acrylic is that it undergoes crazing (effectively, rapid brittle failure across any loaded components to an extent that can resemble disintegration) when sprayed with ethanol, and the components tend to fracture into pieces when under tensile load. Water-jet-cut (WJC) polycarbonate parts are recommended for future fabrications given the need for pressure-fitting the parts together and proper disinfection protocols as they enter and leave the tissue-culturing areas of the lab. To validate bioreactor operation and design, cells were cultured and strained using these devices before the bioreactor was redesigned for high-throughput cell experiments using the available resources and motors.

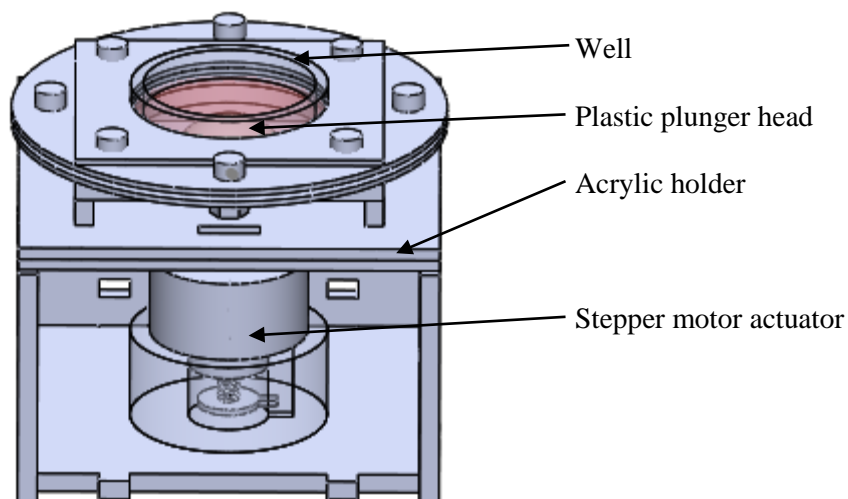


Figure 2.12: Initial one-well bioreactor design.

The final enclosure design, shown in Figure 2.13, needed to permanently enclose the motors in a way that ensured they would not have to leave the incubator for days and would not need to be constantly re-assembled prior to each test. A waterproof-rated box meant for electronics enclosures from Hammond Manufacturing[93] was purchased. The lid was altered using a waterjet cutter so that the actuators could be bolted on. A plastic sheet was used as a diaphragm/seal and secured with Kapton® tape. The motors were cooled using air circulated through the enclosure. The wells were clamped down by bolting a water jet cut aluminum plate on top of the wells. 5-phase Vexta motors were used, both to minimize vibratory output and because that it was the only motor of which 6 fully functional motors of the same model were available.

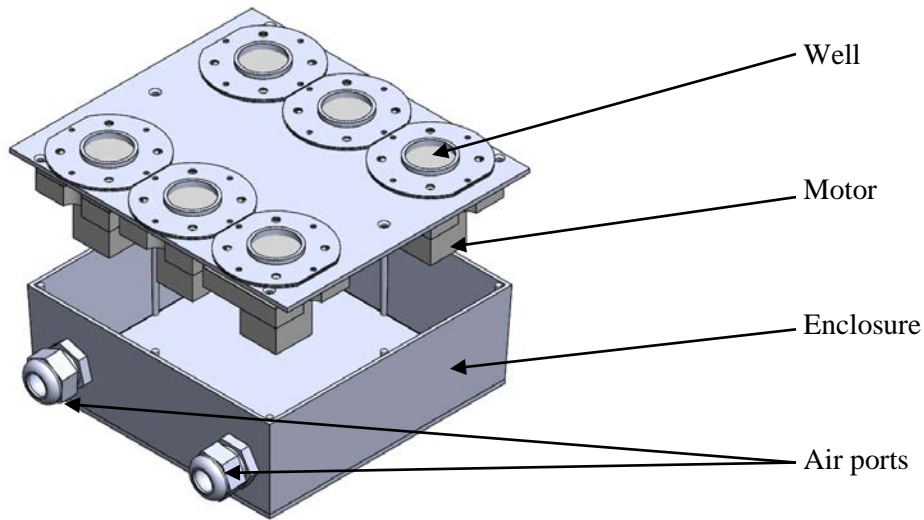


Figure 2.13: Final bioreactor design.

PDMS parts were molded using laser-cut acrylic slices. Membranes as thin as about 200 μm were produced by clamping two glass slides using tape or similar-thickness materials as shim stock. PDMS surfaces were etched with a grid using a laser cutter for the purposes of tracking strain.

PDMS flanges were also needed to build an enclosed well. Moulds were made by stacking laser-cut parts. One of the resulting components is shown in Figure 2.14.

The flanges were then glued onto the membranes using PDMS, producing a sealed well. WJC aluminum or stainless steel disks were then used to clamp the PDMS substrate onto the bioreactor.

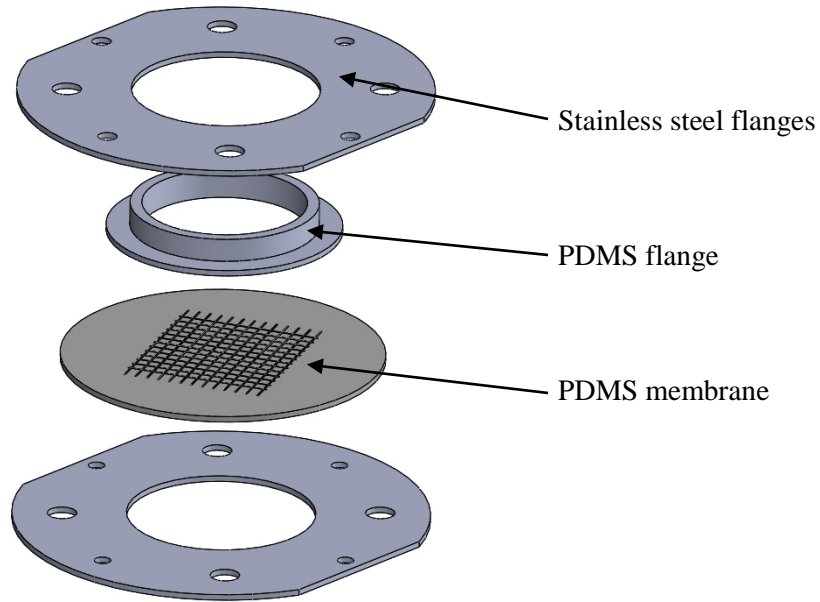


Figure 2.14: Cell culture well and laser-etched PDMS membrane. The PDMS membrane is coated with collagen to allow cells to adhere to its surface. A flange molded out of PDMS provides a biocompatible wall to hold culture media. Stainless steel flanges are secured via bolts to clamp the well together and onto the bioreactor enclosure.

As will be discussed later, heat transfer was determined to be a potential problem during the high-throughput bioreactor design. The 5-phase motor-based actuator, shown in Figure 2.15, includes an aluminum block to increase heat capacity of the motor and polycarbonate/acrylic layers to thermally insulate the motor from the rest of the enclosure.

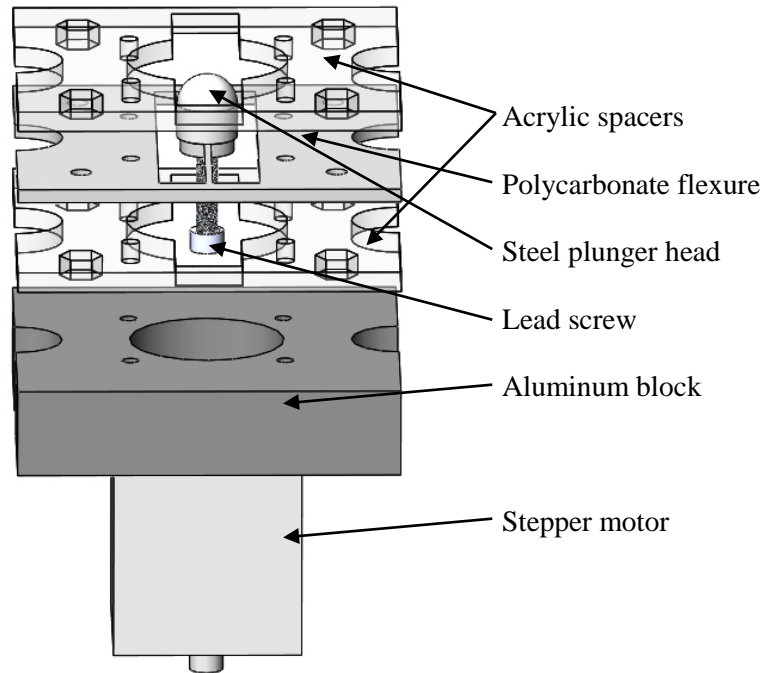


Figure 2.15: Actuator with stepper motor and flexural bearing.

2.3.1 Heat Transfer Modeling And Simulation

Another potential issue with motor-driven actuators in bioreactors is the heat generated. The temperature at which cells are cultured strongly affects cell differentiation and incubators typically control temperature to $37\text{ C} \pm 0.1^{\circ}\text{C}$. Higher culture temperature has well known effects on proliferation rates, and 40°C culture temperatures can result in widespread cell death[94]. It also upregulates heat shock proteins, many of which are produced in response to other stressors[95]. Periodic heat shocks or stresses as low as 38°C have been found to affect the cells[96] by affecting the circadian rhythms of the cells.

The heat generated as a result of work done in flexing the membrane is far too small to result in overheating. Membrane forces were estimated in an earlier section. Energy produced through work is calculated as:

$$W = \int F dx \quad (2.3)$$

W is the work performed in Joules and F is the force in Newtons integrated across the distance travelled. Work was estimated by assuming the force required at maximum deflection was constant throughout the motion for the maximum amplitude. Based on the force-amplitude curves derived earlier using Comsol, PDMS membranes require approximately 10 mJ for each stretch and each relaxation for a deflection of 10 mm. As no energy is being stored in the membrane or motor, as nothing is changing in height and the membrane is not increasingly storing energy, all of the power being used by the motors must ultimately be dissipated as heat. The mechanical loading leads to approximately 20 mJ emitted per strain cycle per well. For a ~0.5 Hz strain cycle, this is roughly 10 mW generated by each PDMS membrane. The heat capacity of 1 mL of water, to approximate the heat rise of the culture fluid, was used to conservatively approximate the heat capacity of the well and the surrounding bioreactor. The strain would need to be cycled at 30 Hz at 10 mm amplitude before even a conservative estimate of overheating occurs (0.1°C rise) simply due to PDMS flexing. This is well beyond the range of mechanical stimulus from respiration.

However, the heat generated by the motors is an issue. Most motors use power even at no load, and most stepper motors will draw power far in excess of the minimum amounts required to deflect the membrane. Power draw specifications for both motor types are shown in the table below, drawn from the manufacturer specifications.

Table 2.4: Voltage, current, and power draw for the Canstack and Vexta motor options.

Motor	Power (W)
H-K Canstack 25000	4
OM Vexta 5-phase	4-12

2.3.2 FEA Modeling Of Heat Exchange Inside the Incubator

Temperature rise inside the cell incubator due to a motor-driven bioreactor was modeled using FEA software. As an approximation of heat dissipation under ideal conditions from a motor-driven bioreactor, the rest of the bioreactor was assumed to be in excellent thermal contact with the wells and to dissipate 10 W of power. While a 6-well bioreactor built using the 5-phase stepper motors could be expected to output a great deal more heat than the 2-phase motors, smoothed waveforms with low acceleration/deceleration minimized the power draw of the 5-phase motors. Without a cooling system or thermal insulation, the heat would be conducted into the surrounding incubator. The incubator walls are maintained at 37°C using a water jacket; therefore, it is a reasonable assumption that the incubator walls will remain at 37°C and act as a heat sink for any heat sources inside the incubator.

Heat transfer from the bioreactor and incubator heat rise were assessed using FEA heat transfer modeling. In theory, heat will be conducted, convected and radiated out of the bioreactor into the incubator. Convective heat losses were assumed to be negligible to simplify the model, as no significant air flow through the incubator was expected. Given that the temperature difference on any exposed bioreactor surface should not be more than a few degrees over ambient, radiative cooling should also play a negligible role as the bioreactor should not have sufficient surface area at sufficient temperature. As such, conductive losses across the bioreactor and into the incubator were thought to be the most likely cooling mechanism.

To estimate the temperature around the bioreactor without additional cooling, heat transfer out of the bioreactor was modeled using Comsol FEA software. Conductive heat losses across the 5 mm thick steel shelf were modeled as a 2D surface, as shown in

Figure 2.16. The temperature on the surface of the incubator walls was set to 37°C as a boundary condition. The heat source was approximated as 50 kW/m³ across the footprint of the bioreactor enclosure, which was equivalent to a 10W source given the dimensions. The simulation modeled heat

transfer through the incubator and bioreactor over 24 hours of constant bioreactor operation. The temperature distribution across the shelf after one hour simulated time is shown in Figure 2.16.

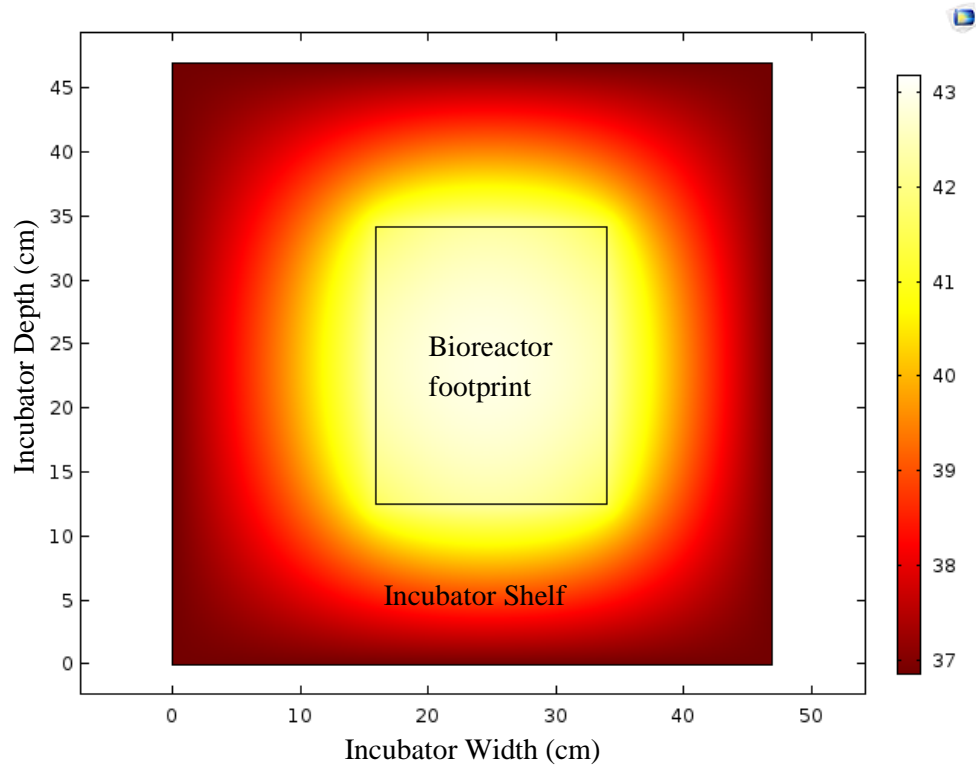


Figure 2.16: Simulation of the heat transfer out of the bioreactor and across the incubator shelf (seen from above). The heat conducts out of the bioreactor, into the steel shelf, and into the walls of the incubator, which are assumed to act as heat sinks. Except for the edge of the shelf at the incubator wall, the entire shelf was predicted to experience a temperature rise above the safe limit of 1°C.

The incubator was also modeled in vertical cross-section, with the bioreactor surrounded by air on an incubator shelf. After about 3 hours, the temperature distribution across the incubator reached steady state conditions, with a peak temperature of 43°C, as shown in Figure 2.17.

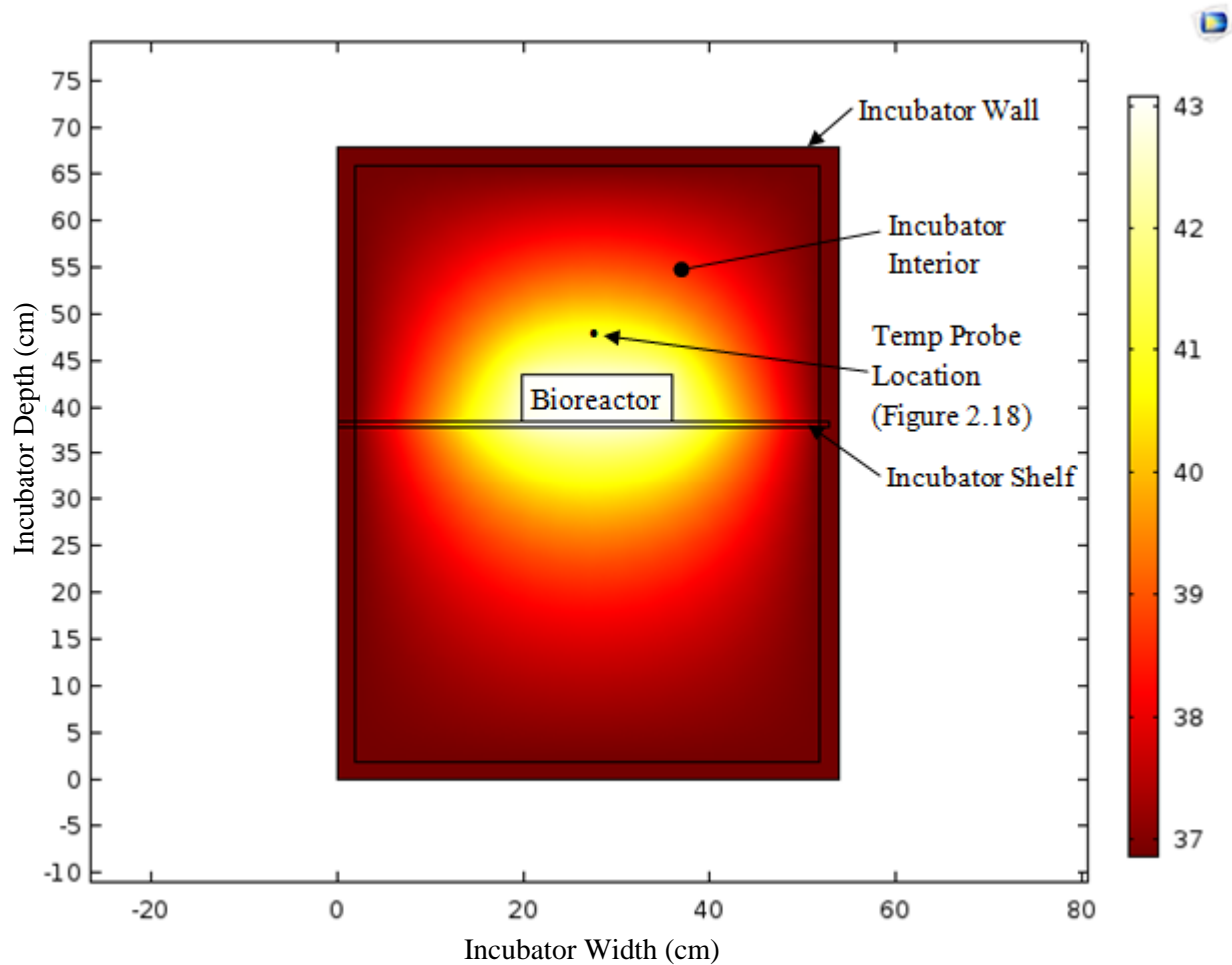


Figure 2.17: Bioreactor and incubator cross-section. The incubator interior was predicted to rise to about 40°C after 1 hour of run time. The bioreactor is assumed to be sitting on a shelf in the middle of the incubator. The location of the probe is indicated by a black dot.

It is worth noting that if these simulation results are valid, the incubator temperature sensor, which is mounted at the upper right corner of the incubator (upper right corner in Figure 2.17), would report temperature rises of 0.5 to 1°C at most despite a rise of 3 to 6°C at the location of the cell cultures in the bioreactor. The temperature probe in the model indicated the incubator temperature remained within 1°C of that temperature rise for the remaining 23 hours of simulation runtime (Figure 2.18). Nearby experiments could also be affected. Temperature rises of 3°C will result in heat shock, drastic changes to protein expression, and eventually widespread cell death. There would also be unexpected negative

results, artifacts and variable results as a consequence of variable proximity to the bioreactor during operation.

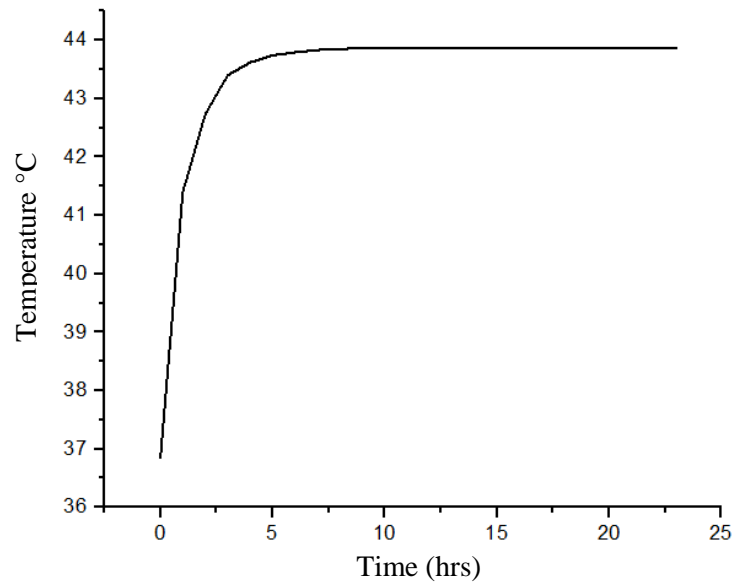


Figure 2.18: Temperature of the incubator over a 24 hour period 5 cm from the top of the bioreactor in the FEA simulation.

There was a 2°C difference in temperature rise between the horizontal cross section and the vertical cross section, presumably due to differences in geometry and thermal mass of the bioreactor due to the difference in cross-section, and the addition of a thin insulating layer between the bioreactor and the incubator shelf in the vertical cross-section model (Figure 2.17). The models show that heat emissions by bioreactor actuators cannot be discounted during design and operation and, if not mitigated, may subject the cells to heat stress sufficient to disrupt basic biological function.

A cooling system was implemented to adequately drain the heat generated by the actuators during operation, and the bioreactor design was modified so that the motors were thermally isolated from the rest of the bioreactor. Each motor was bolted into an aluminum spacer, 1 cm thickness, to act as a heat sink.

Using the 1D heat conductivity equation for heat flow through a wall:

$$\dot{Q} = \frac{kA(T_B - T_I)}{d} \quad (2.4)$$

An acrylic spacer of 1 cm thickness with surface area of 0.0036 m² was determined to limit heat transfer to 0.4 W given a 6°C rise in motor/sink temperature. As long as the remaining heat can be reliably removed using a cooling system such that the temperature inside the bioreactor stabilizes at 43°C or below, the thermal insulation appeared to be sufficient to prevent the overheating of cell cultures inside a running bioreactor.

Both water and air cooling were possible; air cooling was determined to be the easiest and least hazardous method to implement given the numerous electrical components in the machine. The implementation was constrained by the resources available; the lab has one air supply at 10 psi pressure.

Air cooling was employed to mitigate the temperature rise produced the power dissipated by the stepper motors. Cooling air was provided at 10 psi from pressurized lab sources, through 3 m of 16 mm diameter rubber hose, into the bioreactor, and back out via the same method. As with the electrical cabling required by the actuators, these tubes were molded into a rubber cork using biocompatible silicon rubber and plugged into the cable access port (25 mm diameter) in the back of the incubator.

The in-well temperatures of the final bioreactor design was evaluated in Chapter 3, as well as characterization of temperature across the incubator due to different heat sources.

2.4 Strain Characterization

2D planar strains are increasingly straightforward to map using one-camera digital image correlation (DIC) methods[97], but non-planar 3D strains require more specialized techniques. Based on prior work, there are three general methods for mapping surface strains across a 3D surface with, at best, micron-scale accuracy:

1. Stereoscopic DIC. Two cameras are used so that the system has depth perception[98]. Single-camera methods which use a prism[99] or different light sources[100] to produce two separate images have also been pursued.

2. Structured-light DIC. A light pattern is projected onto the surface, and distortions correspond to changes in height[101].
3. Coordinate measurement of a series of points across the surface in 3 axes.[102]

Characterizing strains across the substrate surface allows the experimenter to test for issues with experimental implementation which cannot be easily studied in an FEA model. The strain distribution in each bioreactor well is not ideal; the actuator may not impart strain in a radially-symmetric way if the well is poorly secured or if the plunger is misaligned relative to the well, for example. A strain characterization method of the strained membrane validates the experimental setup and provides a more direct and reliable strain characterization than FEA modeling.

The amount of time required to map the strain could mean that the strain pattern at any particular actuator amplitude during a cyclic strain experiment will be different from the strain pattern at any particular actuator amplitude as measured by any strain mapping method. Any of the methods described above would allow for validation of strains developed across a substrate while the membrane is statically stretched. They cannot measure strains while the membrane (or any other substrate) is in motion, as it would be during a real bioreactor experiment. If the actual strain across the substrate during 0.5 Hz cyclic strain is affected by hysteresis, or the equilibrium strain pattern across the surface of the PDMS takes any significant fraction of the cyclic strain period to develop, the strain pattern across the PDMS membrane surface during cyclic strain experiments will be different from the strain pattern measured using these methods. It is doubtful that this will occur for thin PDMS membranes, although the same cannot be said for all 3D gel cultures or tissue scaffolds. Basic validation of strain across the substrate and experimental design can at least be confirmed using this method, although *in situ* observation of substrate strains may still be valuable.

2.4.1 Strain Across a Unit Square

The strain ε on an object is one-dimensionally defined as:

$$\varepsilon = \delta/L_{ref} \quad (2.5)$$

L_{ref} is the reference length and δ is the amount of stretch. Depending on the nomenclature, the reference length is either the length of the object before stretch (Lagrangian), L_0 , or after stretch (Eulerian), L . This analysis, and most solid mechanics analyses, relies on the Lagrangian definition.

This definition of strain is applied to an infinitesimally small square on a plane, which changes shape as it undergoes deformation. Magnitude of strain across the principal axes x and y can be expressed by

$$\|\epsilon_i\| = \frac{\|D_i\| - \|A_i\|}{\|A_i\|} \quad (2.6)$$

where i is the axis x or y depending on the direction, and D and A are the side lengths after and before strain, respectively. Assuming a cell can be approximated as infinitely narrow, it would experience a magnitude of strain depending on its direction relative to the strain stimulus.

The mapping system, as implemented in this thesis, determines the xyz positions of a series of evenly-spaced grid points. As such, the strains ϵ_x and ϵ_y are determined by finding the lengths between grid points before and after the surface is strained. This holds as long as each square can be roughly assumed to be planar and as long as strain across each unit square can be assumed to be relatively uniform. The magnitude of strain in each grid square can be calculated using this data.

2D strain mapping alone cannot measure the curvature of the overall membrane surface and, therefore, will be in error when there is any significant deflection. The potential error is discussed below, assuming that the visual sensor used for 2D DIC is co-planar with the surface and that the sensor is far enough away from the surface so that, as the object deflects and moves closer to the camera used in the mapping, it does not significantly increase in size.

2.4.2 Surface Strain Measurement Error Due to Height Measurement Error

It is not possible to simply neglect the vertical deformation of the substrate during strain characterization. Given a substrate deflection of 8 mm, as in the FEA modeling, the substrate would deflect by approximately 0.5 mm per radial millimetre across a 35 mm diameter substrate, assuming

axisymmetric strain and ideal boundary conditions across the surface, a potentially poor approximation. Using a 2D DIC method in this context would result in errors in length measurement of at worst 25%.

Once the substrate deformation has been mapped across a grid of evenly spaced points, curve fitting and interpolation between points is an option. The true, non-planar strains would be found by finding the projection of the 2D 'planar' strain measurements onto the true topography of the substrate. For these experiments, the surface was approximated as linear between each grid point to simplify calculations.

In a linear approximation, the error in measuring substrate height at each point can be estimated using Pythagorean theorem. For a given error in height measurement, the error in strain is

$$\frac{\sqrt{X^2+(H+E)^2}-\sqrt{X^2+H^2}}{\sqrt{X^2+H^2}} \quad (2.9)$$

Where X is the planar length of the grid line measured using some 2D method, H is the vertical displacement between the two points, and E is the error in measurement of the vertical displacement.

2.4.3 Vertical Deformation Mapping Methods

The easiest way to map the surface topography would be to use a sensor that can determine surface height at a point, and then perform this measurement repeatedly across a grid of evenly spaced points. The implementation of this method was limited by lab resources and experimental constraints. Pressure-based touch sensors, for example, would require sufficient sensitivity to detect a rubber or potentially even a hydrogel surface without excessively deforming it; would need to be built inexpensively and easily enough for the device to be built and tested within the required time frame and budget; and would need to perform the measurement rapidly enough that 200+ point measurements within a few hours would be feasible.

Two methods were explored:

1. Substrate focus. This method was limited by the quality and cost of reflected-light microscope cameras which are small enough to be easily mounted onto a moving 3-axis stage to perform the measurements.

2. Touch probes which determine contact by checking the impedance across the probe and substrate. This method is only possible if the PDMS surface can be rendered conductive.

In theory, either method would work on a hydrogel or wetted electrospun surface; there are sufficient substrate features for substrate focus in either material, and once wetted, either material should be sufficiently conductive for the touch sensor to be able to distinguish between an air gap and physical contact with the material.

2.4.4 Conclusions

A bioreactor suitable for HASMc tissue cultures, or culture of other cell types exposed to respiratory strains, was designed and implemented. This required modeling of the strain fields in the PDMS substrate, actuator selection and design based on the needs set in the literature review and the requirements drawn from the models, enclosure design to mitigate contamination and heat transfer problems and a strain characterization system.

Strain conditions were modeled across the PDMS substrate to determine design requirements and determine how different methods of deforming the PDMS membrane would result in different experimental conditions. These hyperelastic FEA models, as well as objectives and performance parameters drawn from literature review, were used to determine actuator performance requirements.

Stepper motors were determined to be an ideal choice for building a scalable, modular bioreactor that can be easily redesigned as an array suitable for 6-well culture, as would be suitable for most *in vitro* bioreactor experiments. Open-loop, programmable motion control allows the experimental standard operating procedures (SOPs) to be altered. Arbitrary motion waveforms, which may be useful in replicating the time-varying strain conditions in the airways during respiration, can be programmed rather than physically redesigning the actuators. Changes in dynamic load, which could be expected depending on the substrate, or altering the well design to produce different strain patterns across the substrate, have

no effect on the motion waveform, avoiding a number of issues. It is also straightforward to redesign the bioreactor into an actuator array for higher-throughput experiments.

Actuators were built using rapid-prototyping equipment. A motor controller able to produce up to four separate arbitrary waveforms with 10 kHz bandwidth was designed and implemented. A disinfectable enclosure which can isolate the motors from the incubator environment was implemented for single- or multiple-motor prototypes.

Temperature rise due to heat generated by the bioreactor actuators was determined to be a potential confounding variable and was studied using FEA modeling. Temperature variations can alter experimental conditions for the bioreactor cells or even for nearby experiments inside the incubator if not adequately mitigated. FEA modeling predicted that the motors could produce a temperature rise of up to about 8°C across the incubator without the incubator registering a problem. A cooling system was implemented to remove the heat generated by the bioreactor motors and the motors were thermally isolated from the rest of the enclosure. The temperature rise inside the incubator due to heat generation by the bioreactor actuators and the effectiveness of the selected mitigation methods is discussed in Chapter 3. In general, the temperature of the bioreactor and the surrounding incubator should be measured in trial experiments before use and heat generation transfer should be accommodated for during the design phase.

Another potential confounding variable is vibration produced by the actuators; design mitigations for the specific actuator type selected were discussed, and vibration emitted by the motors will be evaluated later. Stepper motors, as well as other motors, can generally be assumed to vibrate in addition to the ~10 Hz or lower motion waveforms they are intended to supply to the cells. This was mitigated by using a 5-phase motor with significantly decreased vibratory output according to manufacturer specification. There are other sources of vibration due to construction of either the motor or the rest of the actuator. The vibratory output of the 2-phase and 5-phase motor-based actuators was assessed, as described in Chapter 3.

Finally, a method of mapping the substrate deformation during nonplanar strains was implemented. Although there are various methods of measuring planar strain, accurately determining strain across a non-planar surface requires a mapping of the height of the surface as a function of position. Further, while DIC or other methods may be advisable in the future to improve granularity, a strain measurement method using a USB microscope camera mounted to a 3-axis stage and a height sensor was developed. This method would allow for validation of strains developed across a PDMS membrane while the membrane is statically stretched, although it cannot measure strains while the membrane (or any other substrate) is in motion, as it would be during a real bioreactor experiment. If the actual strain across the substrate during 0.5 Hz cyclic strain is affected by hysteresis or the equilibrium strain pattern across the surface of the PDMS takes any significant fraction of the cyclic strain period to develop, the strain pattern across the PDMS membrane surface during cyclic strain experiments will be different from the strain pattern measured using this method. This method allows for validation of the strains across the membrane at the peak amplitude of the bioreactor actuator and can be used to determine whether there are errors in apparatus design or setup which could alter the experimental results.

Cyclic strain has been known to produce realignment in HASMcs and other cell types. As a basic validation of the bioreactor's operation, HASMcs would be subjected to cyclic strain using this equipment and the realignment assessed. Cells were also be exposed to static strain, as a control to compare to the cyclic strains and to confirm that cells were responding to a time-varying signal rather than just to the peak strain the substrate experienced.

3 Results

Following the requirements and design phases of Chapter 2, the bioreactor, the strain characterization method, and the potential sources of error due to heat or vibration emitted by the actuators needed to be validated or characterized. The bioreactor actuators were programmed to carry out a specific motion; whether the actuators followed the programmed motion needed to be confirmed and the vibration emitted by the motors throughout the experiment needed to be measured. FEA modeling had indicated that heat generated by the motors could cause temperature rise and affect experimental results; the validity of the FEA modeling needed to be confirmed by tracking temperature rise in and around the bioreactor due to heat sources simulating the heat generated by a potential actuator. The air cooling system meant to mitigate temperature rise in the bioreactor also needed to be tested. Next, the strain characterization method needed to be tested; the repeatability of the substrate focus or touch sensing methods and the *xyz* point mapping across the substrate was tested, and a trial run of the system across a PDMS surface was conducted using substrate focus. Finally, the entire bioreactor system was validated by subjecting cells to cyclic strain and static strain to ensure that the cells adhered properly to the PDMS membrane and that the most basic endpoints of cyclic strain experiments, cell realignment to uniaxial strain, occurred.

3.1 Actuator Validation

The bioreactor actuators provide an arbitrary motion waveform, resulting in a time-varying strain field across the well, with the field pattern varying depending on the membrane design. The accuracy of the motion waveform and whether the actuator generates excess 100 Hz-bandwidth noise was evaluated. Methods of evaluating these quantities without specialized lab equipment had to be developed.

A linear potentiometer[103] was used to measure the motion. A flexure which produced small and design-adjustable spring force against the direction of load was designed and cut out of polycarbonate. Based on measurement against a set of calipers it was determined that the potentiometer had a resolution of 10 μ m/mV. Potentiometer linearity was checked by manually stepping the potentiometer in 1 mm

increments using a 3-axis stage. The stage was previously calibrated and verified within that range of motion using glass microscope slides of known thickness which was validated, in turn, using a machine-shop grade granite surface and a dial gauge.

The potentiometer was then loaded against one of the actuators and was used to measure its motion waveform. Figure 3.1, below, shows a plot of the actuator in motion for 3 cycles.

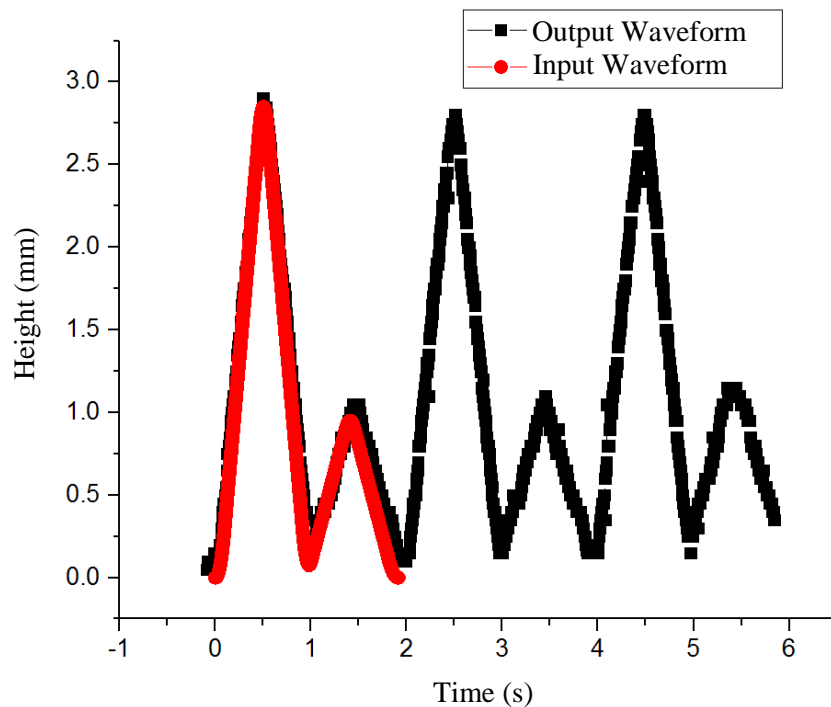


Figure 3.1: Actuator motion for 3 cycles.

The measurement of actuator motion provides validation that the actuator is correctly fabricated such that it does not experience open-loop drift, that the driving current is sufficient to overcome load forces so that pulses are not dropped resulting in open-loop drift, and that the motion controller program is sending the correct pulse waveform to the actuator. However, the potentiometer/flexure does not have the bandwidth to detect motion beyond 1-2 Hz, and as such, the potentiometer cannot be used to check for higher-frequency vibrations. Position measurement accuracy is limited by the electrical noise in the

connection and the resolution of the ADC; the potentiometer accuracy is $10\text{ }\mu\text{m/mV}$, so electrical noise will affect the signal. The potentiometer may also experience stick-slip motion due to friction between the moving contact electrode and the resistive material.

A piezo vibration sensor was used to measure vibration to a bandwidth of 100 Hz, allowing the assessment of noise generated by flaws in the actuator mechanism or due to eccentricity and misalignment of the motor shaft relative to the housing. One actuator of each type was assessed. The sensor was placed in direct contact with the tip of the actuator linkage in each case. As the 5-phase motor has a step size of $1\text{ }\mu\text{m}$, in contrast to the $6\text{ }\mu\text{m}$ step size of the 2-phase motor, different stepping frequencies are required for the two types of motors. No significant differences in vibration were noted between the 2-phase and 5-phase actuators at the tip of the plunger mechanism, as shown below in Figure 3.2. One actuator of each type was tested; one 2-phase motor with a built-in lead screw and one 5-phase motor with a custom-built lead screw attached to a rotary 5-phase motor.

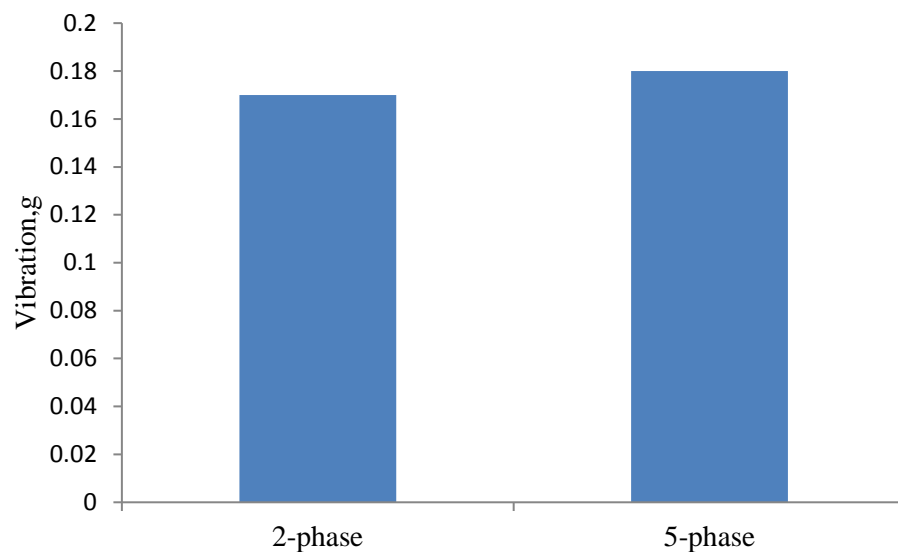


Figure 3.2: Motor vibration, 100 Hz bandwidth.

The best explanation for these results is that the eccentricities in the lead screws of the actuators generate vibration within a 100-Hz bandwidth during rotation (the harmonic oscillations generated during

the stepping sequence are well out of bandwidth for the sensor). This would indicate that at the stepping frequencies which produce the amplitudes necessary, the 5-phase actuator design emits vibration roughly equivalent to the 2-phase linear stepper motor within the testable bandwidth of the sensor. It would be useful to assess motor vibration within a wide enough bandwidth to observe differences due to stepping size, but suitable sensors were not available.

3.1.1 Discussion: Actuator Design, Implementation, and Testing

The bioreactor design provides wide range and speed, programmable and arbitrarily-shaped strain waveforms and the position waveform is unaffected by dynamic loading. Inside the well, altering the membrane design would allow for biaxial or uniaxial strain stimuli to be studied relative to cellular alignment. The bioreactor design and accompanying programming, control and other methods allow for any of the experiments in the published literature review to be carried out. The bioreactor design in this thesis should provide all of the advantages of other experimental apparatuses barring *in situ* microscopy during the strain cycles. However, during the process, it became apparent that vibration emitted by the actuators may affect cell behavior and response to strain; the actuator options were compared using an accelerometer.

Strain stimulus and cell alignment can both be controlled by altering the substrate and although this aspect was not explored in this thesis, it may provide some benefit in future bioreactor experiments. Cells align parallel to microgrooves 1-5 μm in width; diffraction gratings can be used as PDMS moulds to produce these features inexpensively without the need for expensive stereolithographic methods[104]. Through FEA modeling and experimental validation, it should be possible to mould custom PDMS flexures meant to impart varieties of biaxial or uniaxial strain of varying amplitude or pattern. Similarly, the moulds for the well components could be modified to allow for different substrates to be anchored inside the well as necessary. These options for modifying the well could be explored in the future if there are reasons to do so.

Programmable strain waveforms allow for better simulation of respiratory strain and allow researchers to evaluate how cells or tissues may respond to more physiologically relevant strain waveforms. The validation shows that the bioreactor designed for this thesis can be programmed with an arbitrary strain waveform to impart onto the culture, within the motion bandwidth of the actuator. A programmable cyclic strain waveform would allow investigators to study how airway mechanics influences ASM response in airways with varying degrees of remodeling and consequently varying strain responses. Variation in amplitude of breaths was used as an example waveform, which has been used before[105]; variations in equilibrium strain or specific peak shapes could also be implemented in future experiments.

The testing equipment itself could be improved. The potentiometer tests showed that the motor and controller were outputting the programmed waveform. This method was sufficient to validate motor operation. Improved waveform measurement methods would include a quadrature encoder or linear voltage displacement transducer (LVDT); Hall Effect sensors[106] suitably implemented may be less expensive, smaller, and place less load on the actuator and may thus provide another means to validate motor operation, and may even provide sufficient bandwidth and resolution to study vibration due to stepping size.

Published *ex vivo* experiments on ASM tissues showed decreasing cellular stiffness as a function of frequency[85], which would affect cellular response and cytoskeletal remodeling. In general, the actin cytoskeleton is assumed to have a nonlinear frequency response and fibroblasts have shown altered behavior in response to 10-100 Hz vibration. Tests showed no significant variation in vibration emissions from the actuators employing 5-phase rotary stepper motors and scratch-built linear drive mechanisms in comparison to 2-phase linear stepper motors. Accelerometers with a bandwidth and sensitivity well beyond those available under the project budget would be necessary in order to study vibration emitted by the stepper motor itself, but the present results imply that alignment eccentricity in the motor or in the lead screw mechanism used to convert rotary motion into linear motion could just as readily produce

vibration as the motor itself. Higher-frequency vibration from the motors would also be easier to damp than ~100 Hz bandwidth vibration emitted due to the design of the lead screw and coupling.

There are various options available to reconfigure the bioreactor system for future applications, and although the validation methods available indicated the bioreactor actuators were functioning adequately, better testing equipment could be used in the future.

3.1.2 Conclusions

The motor controller and bioreactor actuator are adequate. Vibration tests showed no difference between the bioreactor actuators using 5-phase or 2-phase motors; the most likely source of any remaining vibration is the lead screw drive. Depending on how the actuators are to be used, there are various ways that the design of the actuator itself and the membrane can be tailored for particular experiments, including controlling cell alignment and the strain stimulus.

3.2 Enclosure Validation

The next step was to assess the temperature rise inside the incubator when using a stepper-motor-driven bioreactor, to assess the extent to which the bioreactor designed in this thesis would pose a hazard to the cultured cells and to examine mitigation methods. As discussed earlier in Section 2.3.1, the motors emit heat. The wells should be as close to 37°C as possible; 38°C or higher will be considered heat stress, and temperatures above 40°C will harm the cells.

First, the bioreactor itself was run for an hour and the temperature rise due to the motor operation assessed with and without air cooling. Next, the temperature rise across the bioreactor and incubator due to 6 to 24 W of heat emission was assessed, corresponding to 1 to 4 W heat emitted per actuator in a 6-well array; in this case, due to limitations in available resources, 4 actuators were used and 1.5 to 6 W of heat per actuator studied. The effects of air cooling inside the bioreactor and thermal insulation of the cell culture were also investigated.

3.2.1 Bioreactor Temperature Rise and Cooling Test

The bioreactor was constructed as described in Chapter 2. A temperature sensor (DHT-22) was taped onto the centre of the underside of the roof of the enclosure. A DS18B20 temperature sensor was taped onto the surface of the well. Thermal paste was applied between the DS18B20 temperature sensor and the contact surface to ensure excellent thermal conductivity between the sensor and the substrate, and were intermittently pushed down by hand to ensure it was still in contact. This additional body heat resulted in the intermittent temperature spikes in the figure below. The bioreactor was then run for an hour in open air. Four of the six motors were run with the drivers adjusted to provide ~200 mA of current to each motor. The experimental setup and test results are depicted in Figure 3.3 and Figure 3.4 respectively.

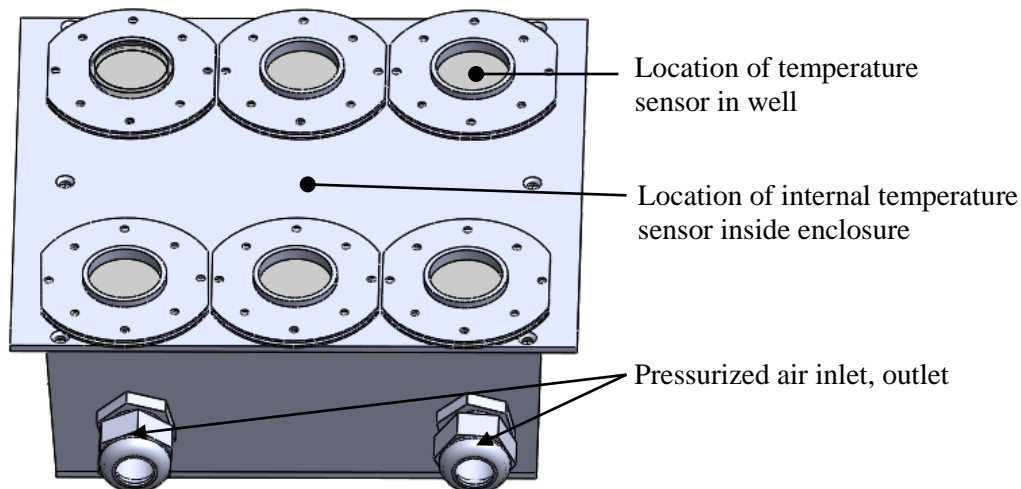


Figure 3.3: Illustration of locations of temperature sensors during bioreactor cooling test.

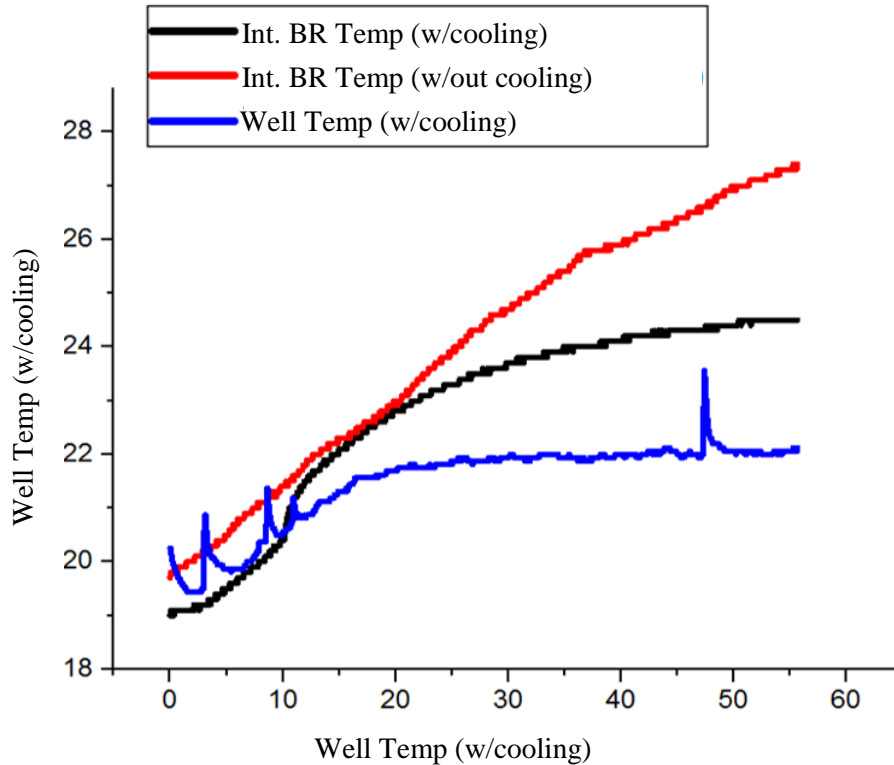


Figure 3.4: Enclosure temperature inside the bioreactor and in the well. The temperature inside the bioreactor and in one of the wells in which cell culture occurs, with and without cooling, and well temperature in a running bioreactor (referred to as 'BR' in the Figure) during a dry run outside the incubator. Without cooling, the enclosure temperature increased until heat began leaking into the ambient environment. Without cooling, the temperature showed no sign of peaking after one hour of run time and reached nearly 10°C over ambient temperature (19°C during the test). With cooling, the internal temperature stabilized at roughly 5°C over ambient, but the well temperature stabilized at 3°C over ambient temperature. 1°C increase is an experimentally confounding condition, and 3°C or more is sufficient to kill cells or substantially alter behavior.

As shown in the figure above, while air cooling appears to be an effective strategy for controlling the motor temperature, the wells are not sufficiently insulated from the interior of the bioreactor. The result would be cell cultures at temperatures of 40°C during experiments.

3.2.2 Heat Output and Temperature Rise Inside Incubator

In addition to the temperature rise of the bioreactor and the cells cultured in it, the temperature increases inside the incubator due to heat emission from actuators were also assessed to check the temperature distributions determined using FEA modeling in Chapter 2 and to assess whether the bioreactors heat up similarly when inside the incubator as in open air. The effect of 6 to 24 W of heat

output on the temperature of the incubator, corresponding to 1 to 4 W per actuator in a 6-well bioreactor array was assessed. The bioreactor frame described in Section 3.2.1 was re-assembled and each heat source was modelled using 15Ω power resistors driven by a DC voltage source, as shown in Figure 3.5 below.

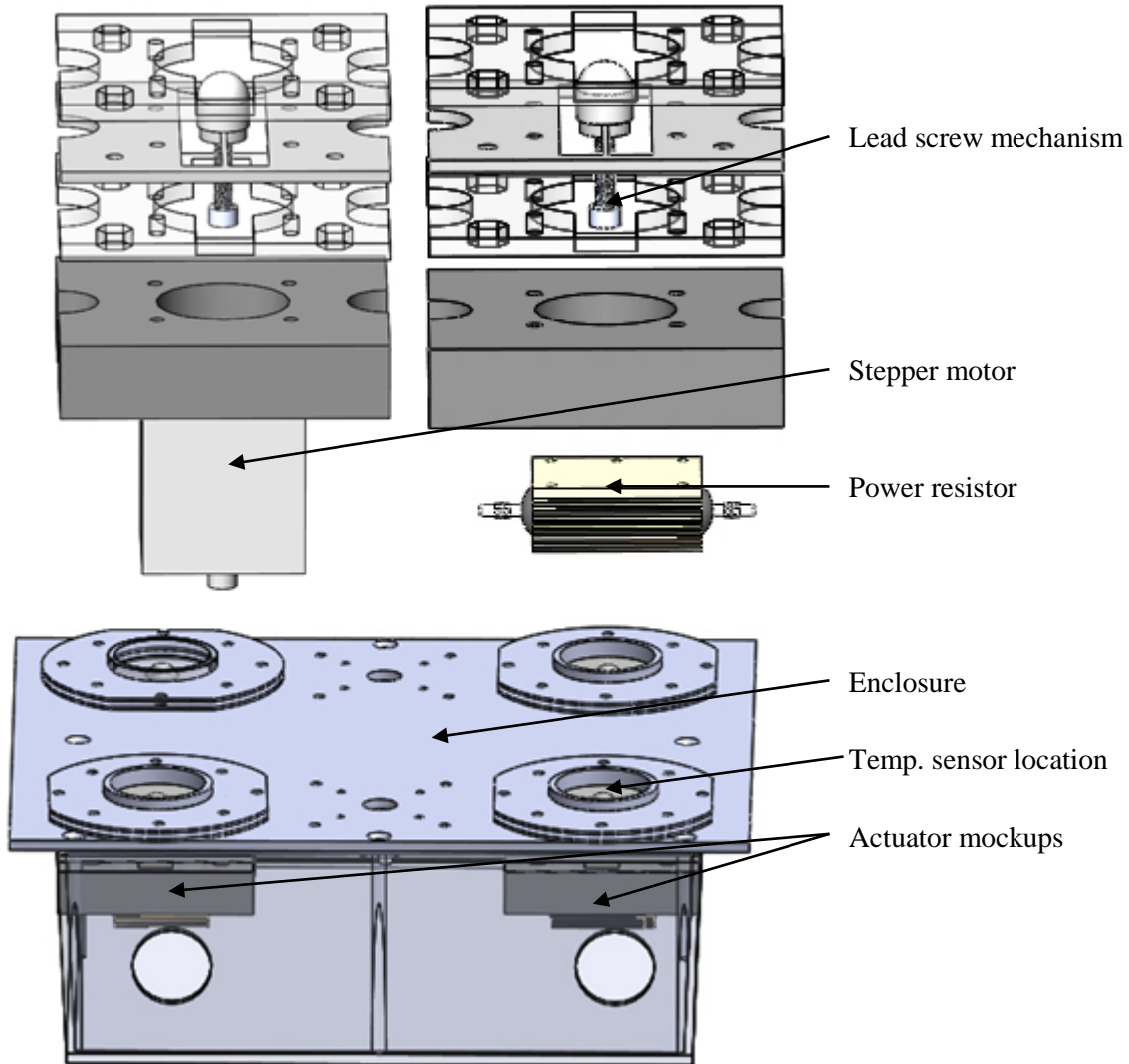


Figure 3.5: Diagram of bioreactor mockup to test temperature rise. The 5-phase motor actuator, left, is fitted with a power resistor as a substitute for the 5-phase stepper motor. Varying current loads are then used to simulate a wide array of potential actuator choices, including the power output range of the 2-phase and 5-phase motors used in these experiments (4-12 W per 2- or 5-phase actuator).

The lead screw in each actuator mockup was positioned such that it was in direct contact with the surface of the power resistor. The cooling system was not used for this experiment. One temperature

sensor was taped directly to the outside of the bioreactor enclosure on top of one of the incubator wells and the other temperature sensor was taped to the incubator shelf, 10 cm away from the bioreactor. The temperature sensor 10 cm from the bioreactor did not increase in temperature beyond 39°C, and consistently reported a temperature within 1°C of that reported by the incubator. After an hour of runtime, each experiment was halted and several temperature readings across the bioreactor surface were taken using an infrared thermometer. Temperatures across the bioreactor surface were within 1°C of those reported by the digital temperature sensor mounted onto the bioreactor well. The results of this experiment are shown below in Figure 3.6.

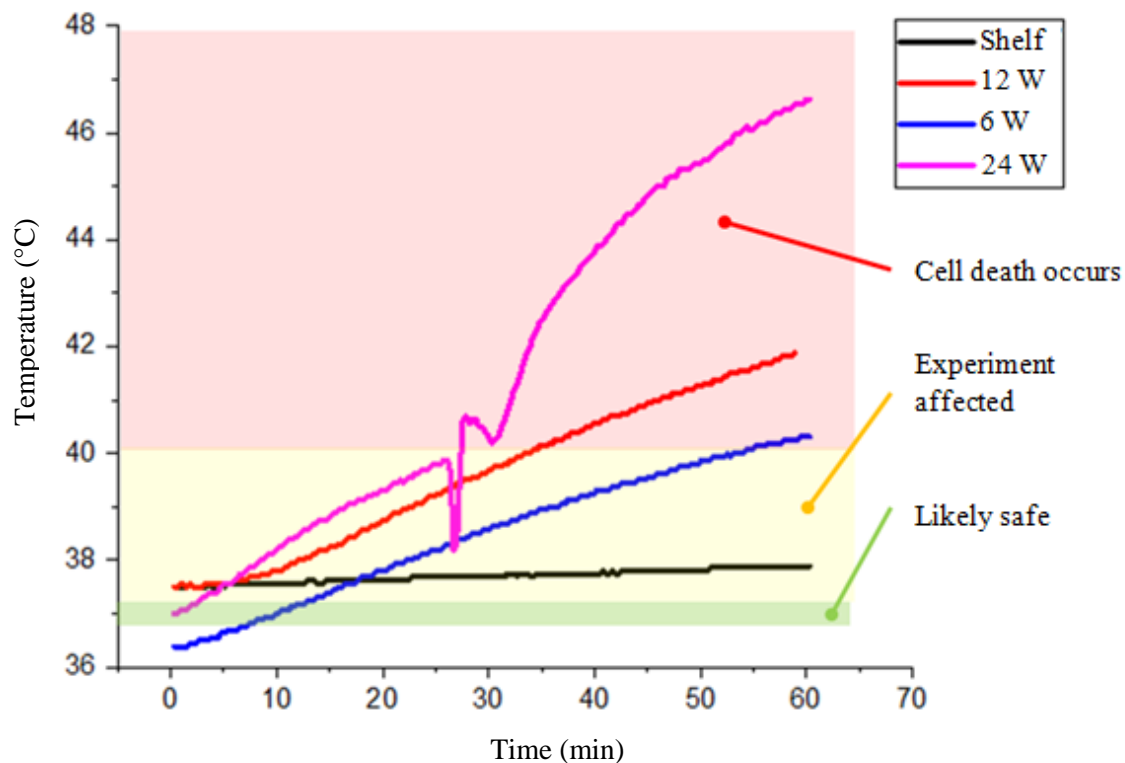


Figure 3.6: Bioreactor temperature rise inside the incubator as a function of time for 6 to 24 W heat sources, modelling various motor combinations. Shelf temperature 10 cm from the bioreactor did not vary significantly between simulations. Note that during the 24W test, the door was opened at about 28 minutes into the test.

The temperature of all of the bioreactor components in direct contact with the actuator heat sources rose dramatically, but the incubator shelf did not substantially vary in temperature and remained within

1°C of the temperatures reported by the incubator itself. The difference between the FEA models and the experimental results is probably due to convective cooling across the incubator shelf and air circulation due to CO₂ injection. The incubator shelf is perforated stainless steel, which increases the surface area inside the incubator and allows air circulation driven by warm, humid air rising from the heated pan in the base of the incubator or by CO₂ injection to dissipate the heat. The fact that the incubator was empty may improve the efficacy of convective heat transfer compared to more typical operating conditions with several experiments on the shelves; results reported here do not conclusively apply to that situation.

Across the bioreactor itself, the temperatures increased well beyond 40°C even for a 6 W heat source, which in the 6-well bioreactor array corresponded to 1 W of heat expended per actuator. This would produce drastically altered cell behavior and death rates in any culture.

3.2.3 Discussion: Heat Exchange and Enclosure Design

Controlling temperature rise due to actuator heat generation was determined to be a major issue in bioreactor design and implementation, although it does not appear to have been discussed previously in the literature. This variable could have been a confounding variable in bioreactor investigations in which heat transfer was not considered or mitigated in any way.

Cell cultures near the bioreactor and its heat sources are unlikely to experience serious heating issues, but cell cultures inside the bioreactor itself are likely to experience excessive temperatures if heat transfer is not accommodated for in the design. Experiments found that although this particular incubator used in the experiments was able to effectively distribute temperature rise across most of the incubator shelf when empty, the heat conducted through the bioreactor produced temperature rises of 4-10°C in the bioreactor for heat emissions between 6 and 24 W total. For a 6-actuator motor array, this would correspond to 1-4 W each. Single actuators in open air overheated similarly for 1-1.5 W of heat emitted. It should be noted that even small DC motors will output 1 W of power, and mid-size stepper motors, DC motors, or voice coils[73] which are appropriately sized for bioreactor applications and have been used previously in publication[74], can generate significantly more heat. Cooling and thermal insulation

provided partial mitigation, but temperature increases of 3°C or more were still measured during tests. Thermal insulation between the cells and the actuators must be improved; separating the actuators from the cells using a drive mechanism exposed to convective heat transfer inside the incubator and composed of materials with poor thermal conductivity, as was inadvertently done in the 1-well prototypes developed earlier in this project, should provide adequate protection from temperature rise. Cultures nearby the bioreactor may experience less than 2°C of temperature rise but this could depend on the incubator design and the number of experiments on the shelves.

Heat emission from bioreactor actuators and the resulting temperature rise inside the incubator does not appear to have been previously explored in other bioreactor designs; based on the results of these experiments, heat emission from actuators could potentially invalidate experimental results. A wide variety of bioreactor designs have employed actuators capable of emitting over 1 W of heat each [70], [73]–[76], [107]–[111]. Two publications were found in which operating temperatures were noted to have been checked prior to use [76], [111]. In one case, temperature rise inside the wells due to the actuator was confined to below 0.2 °C over a 4-hour period[111]; in the other case, temperature rose to 38 °C within 15 minutes and oscillated between 37°C and 38°C at a frequency consistent with when the actuator was activated[76]. In the latter case, cell proliferation was measured using DNA secretion; in a culture subjected to similar thermal conditions as in the bioreactor, it was found that mean DNA concentration increased by 10% and variance increased by 200% due to this thermal stimulus. Although the results were not statistically significant, the sample size (n=3) was smaller than could be applicable for many cell culture experiments. As mentioned earlier, temperature variations of similar amplitude have been used in other experimental protocols[96] to assess how cells rely on temperature cues as part of circadian oscillation and temperature variations have a well-known effect on cell proliferation rates[94]. In the future, heat generation by the actuator should be accommodated by design, and the effects on the cells being cultured assessed prior to the bioreactor being used for experiments.

As the materials selection for the actuator linkage and the current draw of the actuator would generally be regarded as details that may not be reported in bioreactor experiments, and as heat transfer across the bioreactor is not widely acknowledged as a potential hazard to experimental results, it is very difficult to determine which bioreactor designs reported in the literature actually suffered from these problems. Heat transfer from the actuator to the cell culture will depend on the design of the actuator linkage used to transmit force or displacement to the cells and even on design elements regarded as minutiae without considering heat transfer. It is straightforward to thermally isolate the cells from the actuator and, at least in these experiments, an empty incubator was able to mitigate the potential heat rise adjacent to the bioreactor due to convective heat transfer and air circulation.

One other alternative solution to heat rise affecting the bioreactor is to build a micro-incubator for the cells and keep heat-generating mechanical equipment outside it. It should be possible to actuate the cells via a diaphragm without compromising thermal isolation. Custom micro-incubators are often built for real-time cell microscopy[112] or to avoid the expense of a commercial incubator[113].

Heat generation and exchange is to be expected even from small electromechanical actuators. Simulations and experiments showed that convective heat exchange inside the incubator does distribute heat acceptably across empty shelves and bioreactors outputting more than 5 W of heat may not be hazards to surrounding experiments; however, the bioreactor itself and any conductive thermal path which experiences minimal convective losses could heat up well beyond the desired experimental tolerances. Solutions to heat generation are feasible as long as the issue is considered during design and tested for during bioreactor validation.

3.2.4 Conclusions: Bioreactor Thermal Isolation and Cooling

Heat generation by the bioreactor actuators and transfer through the enclosure and actuator linkages has been concluded to be a serious risk to experimental validity in bioreactor experiments. If heat generation and transfer are not accommodated for in the design of the bioreactor, it appears likely that cell culture temperatures within the bioreactor will exceed 40°C; even if the temperatures rise to 38-39°C,

variations in cell behavior could still occur, as discussed below. Further, thermal isolation of the bioreactor actuators from the bioreactor frame was attempted but was not sufficient, as the linear drive mechanism itself was able to conduct heat into the cells sufficient to create 40°C conditions; actuator linkages should be designed to minimize heat transfer (this would be straightforward in many designs) and the temperature inside the well checked prior to experiments.

3.3 Strain Characterization

Given that the strain is distributed across a non-planar surface, mapping the shape of that surface is necessary for accurately characterizing the strain. Substrate focus (determining height based on depth of focus using a microscope) was used initially to find the surface, but there were limits in its application and capability. While this method did allow for identification of x - and y -features to within $\pm 25\text{ }\mu\text{m}$, z -axis characterization was limited to roughly $\pm 60\text{ }\mu\text{m}$. This was still sufficient to note significant implementation problems in the bioreactor well, but higher accuracy would be desirable.

An alternate method is a conducting touch probe, where surface contact could be identified by electrical contact. This method was implemented and tested on rubber by applying PEDOT:PSS to the surface, rendering it temporarily conductive. Tests showed that the probe was able to identify the substrate surface to within $\pm 25\text{ }\mu\text{m}$.

3.3.1 Topographical Mapping Using Depth of Focus

One simple way to find the height of the substrate is to use a microscope by finding the height at which the substrate is in focus.

Measurement accuracy in z was limited by the focal plane thickness of the microscope camera. This was determined to be $50\text{ }\mu\text{m}$, based on the width at which a surface at a 45° angle to the camera lens was in focus. Grid patterns were laser-etched onto the PDMS substrates, as depicted in Figure 2.3. Microscopy showed they were approximately $250\text{ }\mu\text{m}$ wide; depth measurements were within the error due to the focal plane thickness of the microscope.

The upper left corners of each vertex between the grid lines were used as position markers rather than the centres of the vertices between the grid lines themselves, limiting the accuracy to the visual acuity of the user and the visibility of the edge of the grid lines rather than to the grid line width. A USB microscope camera (Edmond Optics, EO1918M) was mounted onto the 3-axis stage mentioned in Section 3.1 and moved overtop and into focus over each grid vertex. As discussed in Section 3.1, positioning repeatability and accuracy of the stage was verified by measuring the dimensions of a gauge block in the form of a glass microscope slide. The gauge block had been dimensionally validated previously using a granite surface plate and a dial gauge. The dimensions of the gauge block were measured using the device, and the measurements were within the positioning resolution of the stage ($2.5\text{ }\mu\text{m}$).

To test the repeatability of the topographical mapping method, the same unstretched PDMS membrane was mapped twice, with resulting errors between the first and second measurements of each point acting as a repeatability measurement. A histogram of the measurement differences between measurements of each point distributed across the grid is shown below in Figure 3.7.

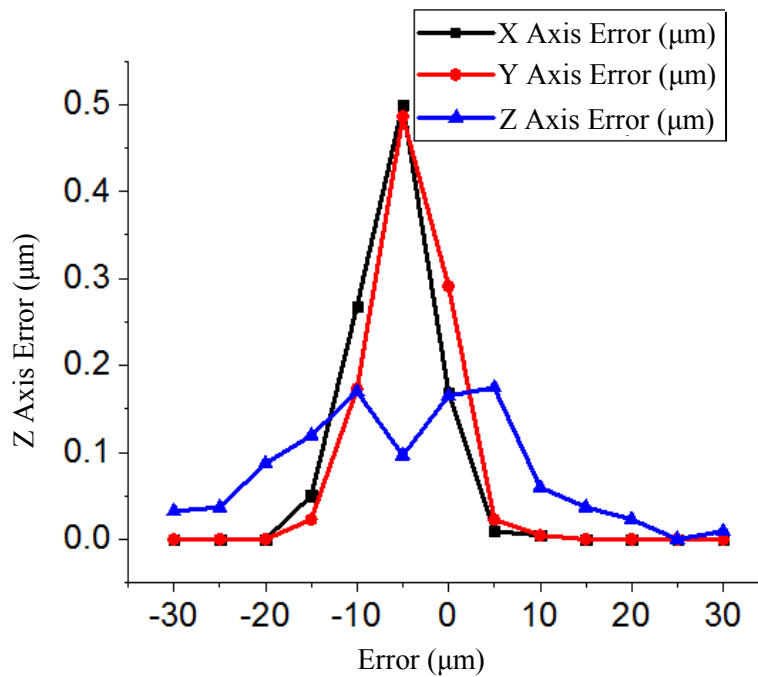


Figure 3.7: Position measurement repeatability of the camera in x,y,z.

A PDMS membrane was then mounted into a bioreactor and the strain characterized using the strain mapping method as discussed in Section 2.4. The strain magnitude across the surface is shown below, in Figure 3.8.

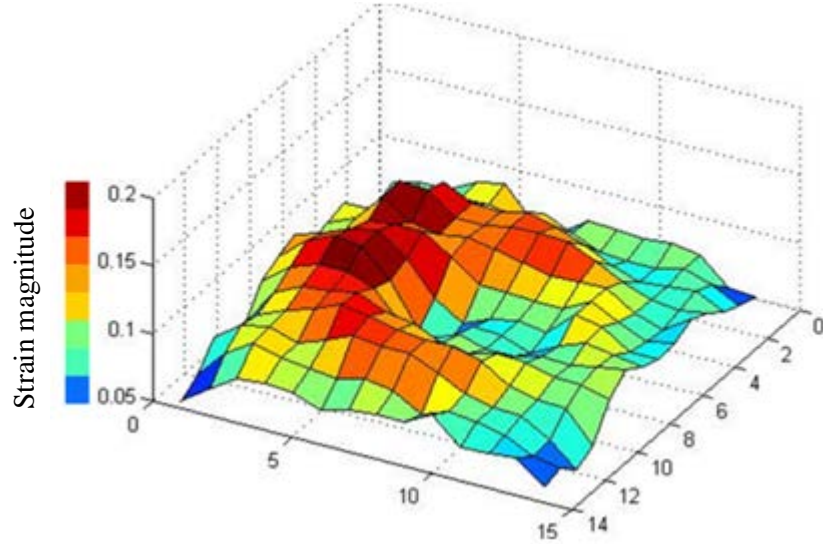


Figure 3.8: Mapped strain of deformed membrane surface. The grid units are in mm.

Depth of focus appears to be sufficient for generally validating the membrane strain patterns. The resulting pattern is radially asymmetric, possibly due to a poorly fixed membrane edge, but it is qualitatively similar to the FEA model. Quantitative results were not expected in any case given the difficulty in obtaining appropriate Ogden model parameters and the differences between the flat plunger shape employed in the FEA model and the spherical head employed in reality.

Although accuracy of the substrate focus method is limited, particularly in z , the method appears to be sufficiently accurate to validate the actual strain patterns compared to those expected. The case discussed above illustrates that the actual strain patterns may differ significantly from those expected due to apparently minor variations in the experimental setup. The FEA modeling of the substrate conducted earlier would be unable to capture these experimental conditions, as it was conducted in axisymmetric conditions. More complicated 3D modeling would be required to even provide the relevant boundary conditions.

3.3.2 Contact Sensor Accuracy

An alternate method to characterize the deformed surface was to render the PDMS surface conductive and to use a touch probe that determined contact based on electrical impedance. After rendering the surface hydrophilic using a corona treater[114], PEDOT:PSS was swabbed onto the surface using a Kim wipe and the surface impedance was tested using a digital multimeter (DMM). One electrode was used as a touch sensor, and mounted onto a 3-axis stage. The other was put in contact with the PDMS substrate. As repeated contact or stresses may have affected the impedance of the PEDOT:PSS layer, Aloe Vera was used as a conducting gel to keep the electrode in electrical contact with the substrate while avoiding damage. Evaluations of the touch sensor were carried out by stepping the sensor closer to the surface until the measured impedance dropped to 20 M Ω in 25 μ m increments, corresponding to the impedance across the surface of the coating. It was determined that the touch sensor could determine the height of the substrate with a repeatability of 25 μ m, presumably limited by the positioning repeatability of the stage. A histogram of the probe accuracy is provided below in Figure.3.9.

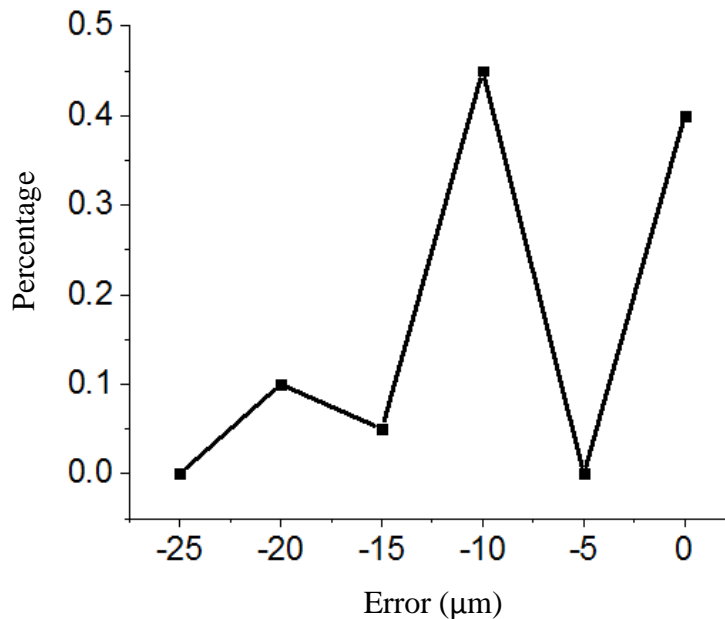


Figure.3.9: Measurement error for the touch probe.

Contact sensing was determined to be a viable method of determining height of the PDMS substrate. To implement this method, the touch sensor would need to be mounted at a known position relative to the microscope camera. Variations in probe position would severely impact accuracy and calibration would be necessary.

3.3.3 Discussion: Strain Characterization

Strain characterization of the membrane surface using two methods, substrate focus and contact sensing, were developed. Substrate focus was sufficient to validate the bioreactor actuator operation. Based on these results, a 3-axis stage with requisite positioning accuracy can be converted into a CMM with 25 μm repeatability and resolution for rubber substrates with minimal investment.

Validating substrate strain, as discussed earlier in Section 2.4, requires validating the nonplanar topography of the strained membrane. Substrate focus using a microscope camera provided $\pm 25\mu\text{m}$ xy resolution and repeatability and $\pm 60\mu\text{m}$ resolution and repeatability in z . By rendering the PDMS surface conductive, it was possible to use a touch probe to determine contact based on when the measured impedance between the probe and a grounding wire in electrical contact with the substrate dropped to 10-26 M Ω . This required rendering the PDMS surface hydrophilic using a plasma system, which adds hydroxyl groups to the PDMS surface by exposing it to ozone. Prior investigations have noted this produces a brittle nanolayer to the top of the PDMS which gradually disappears[103]; presumably, the conductivity effects disappear when the substrate is subjected to tensile strain due to the brittleness of the nanolayer. It will be necessary to subject the substrate to tensile biaxial strain during application of PEDOT:PSS and thus it would also be necessary to optimize how the substrate is coated with PEDOT:PSS to produce a uniform layer thickness, either while the substrate is subjected to strain or in such a way that the conductivity survives the cyclic strain tests.

Characterizing 2D strain across the surface can be accomplished using the grid vertex method and useful information can be obtained. The grid could be stenciled or printed in the future, rather than etched into the substrate, to minimize the effects varying membrane thickness on strain.

Regardless of the methods chosen, strain validation is generally necessary for bioreactor tests. The tested membrane was found to have uneven clamping force around the boundaries of the membrane, causing unexpected warping of the strain field. Even determining the qualitative effects would be difficult using a typical axisymmetric FEA model, as the effects of non-uniform boundary conditions along the edges of a hyperelastic substrate would not be possible to study. Measuring strain fields less than 1 mm from the edge of the substrate would be even more difficult using this method and was not attempted.

A microscope camera mounted onto a 3-axis stage could determine xy position of a series of optical landmarks with $\pm 25\ \mu\text{m}$ repeatability in xy and $\pm 60\ \mu\text{m}$ repeatability in z , sufficient for mapping strain across the substrate. A conductivity-based touch sensor was able to determine surface height to a repeatability of $\pm 25\ \mu\text{m}$, which appears to be mainly limited by the resolution of the stage. Optimization of the PEDOT:PSS layer application and a complete design of a sensor head would still be necessary before the method can be fully implemented.

3.3.4 Conclusions

A method of mapping the substrate strain validates bioreactor operation and allows for detecting flaws in implementation before they affect experimental results. Using the depth of focus of a microscope is a straightforward and familiar method of determining substrate height, although it places limits on resolution and accuracy. However, rendering the PDMS substrate conductive using PEDOT:PSS and determining substrate height using a touch probe appears to provide substrate height measurement limited only to the resolution and repeatability of the 3-axis stage being used.

3.4 HASM Response

To validate the bioreactor operation, HASMcs were subjected to cyclic and static strain using the single-well bioreactor designs. The cells realigned to both stimuli when tested in these preliminary experimental settings.

Primary HASMCs were obtained from the tissue bank at St. Paul's Hospital, with bioethics approval provided by the Dorscheid lab. Cells were cultured under standard conditions in Dulbecco's Modified Eagle's Medium, 10% w/v FBS, and 1% penicillin/streptomycin (P/S), refreshed every 2 days. At Passage 7, cells were seeded into the collagen-coated PDMS wells for bioreactor stimulation. One well per experimental condition was employed. Cells were fed DMEM and 1% P/S every 2 days while in the PDMS wells. After 24 hours of standard culture, the wells were mounted onto the bioreactor and subjected to cyclic strain for 8 hours per day for 3 days at 3 mm amplitude and 0.5 Hz frequency, with a triangle waveform. Micrographs were taken of the centre of the well and near the edge of the well, which was identified in the micrograph as a shadow due to the well wall.

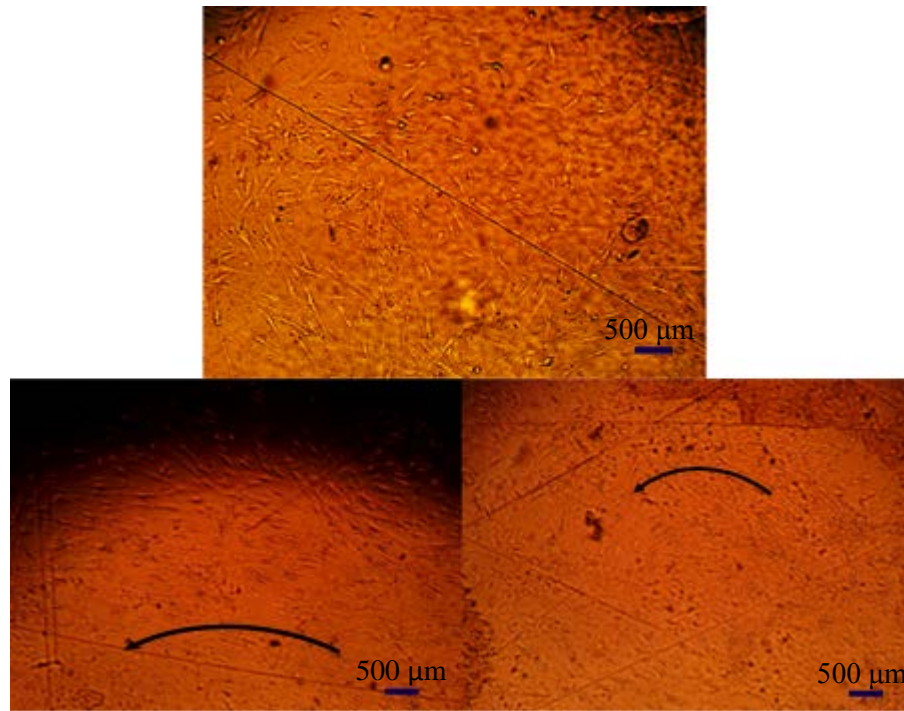


Figure 3.10: Cells before and after cyclic strain. Top: Cells prior to strain, near the edge of the well. Bottom left: Cells at the edge of the well, following 24 hours total cyclic strain. Bottom right: Cells near the centre of the well, following 24 hours total cyclic strain. Circumferential direction is indicated using arrows.

To quantify realignment in the images above, the cell alignment was measured and the variance in direction calculated for 3% of the cells. The direction of the cells was measured manually for a random sampling by drawing a line across the major axis of the cell. The lines were converted into polar

coordinates relative to the centre of the well and the variation from circumferential alignment determined in degrees. This is illustrated in Figure 3.11, below.

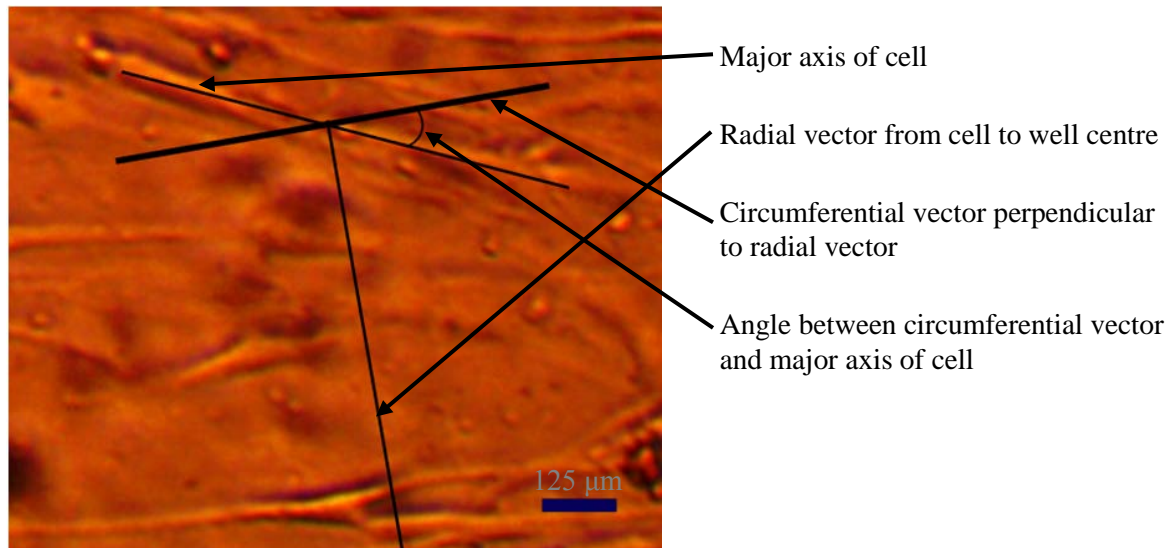


Figure 3.11: Diagram illustrating cell alignment calculation.

In a second experiment, passage 7 cells were also similarly deposited into a PDMS well. After 24 hours of standard culture the well was mounted onto the bioreactor, the motor set to 3 mm amplitude, and left in static strain conditions for 3 days. The cells realigned, as shown in Figure 3.12. Realignment was measured as discussed above.

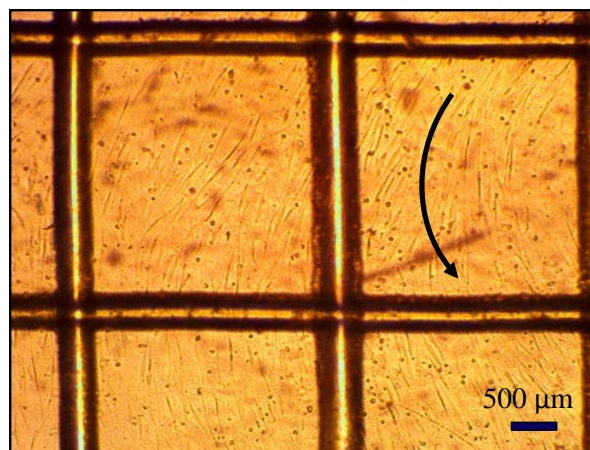


Figure 3.12: Realigned HASMcs on D3-4, static strain conditions. The grid lines are due to laser-etching on the underside of the substrate. Circumferential alignment is indicated by the arrow.

The variance in cell direction in all of the samples is shown in Figure 3.13; realignment was determined as above. As a control, an image of the cells in an unstrained PDMS substrate was used (Figure 3.10, top).

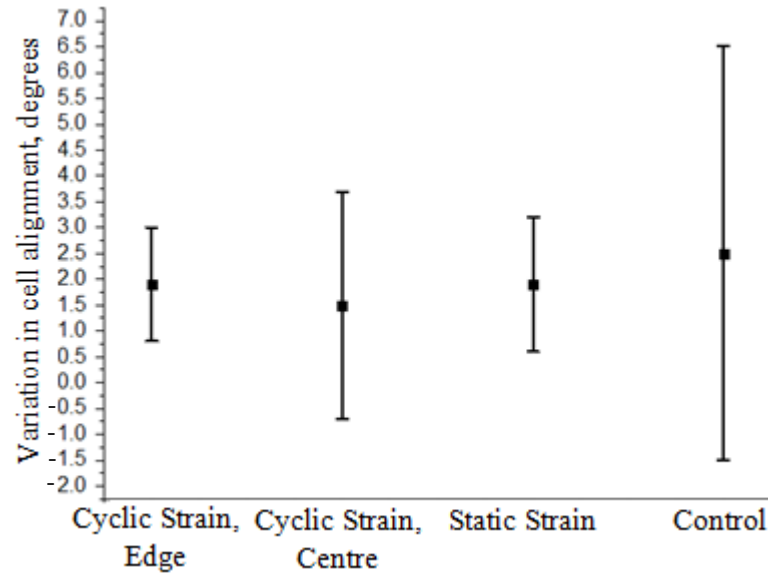


Figure 3.13: Variance in cell direction as affected by cyclic and static strain, compared to an unstrained control.

The cells appear to be affected by the cyclic strain stimulus in a manner similar to prior experiments performed in other labs[38], except that static strain appeared to produce realignment as well as cyclic strain.

3.4.1 Effects Of Static And Cyclic Strain And Experimental Design

Cellular response to cyclic strain in the bioreactor was demonstrated to be the same as in prior experiments[60]. *In vitro* experiments in this thesis were sufficient to determine that the bioreactor design was functional, and methods of minimizing technical sources of variation were discussed, but future experiments using this bioreactor design will need to be conducted with an appropriate number of well replicates and separate cell donors such that the variation in cell response due to genetic variability can be differentiated from the variation in cell response due to technical sources of noise. The cells realigned in

the direction of minimal strain; although the results were not replicated sufficiently to be statistically significant, this matches the response commonly reported in other studies for this cell type[60]. HASMc response to static strain does not appear to have been previously recorded, but the cells realigned as readily as in cyclic strain; although more tests would need to be conducted for the results to have statistical significance.

Future experiments will need to ensure that technical variation and genetic variation are accounted for in experimental design as well as bioreactor design. Variations in measured protein expression due to genetic variation between cell sources must be controlled as part of experimental design[116] in future experiments. How noise from technical variations due to bioreactor design could be minimized was discussed in this thesis; specific experimental designs are out of scope. There will be variability in how HASMcs alter themselves or their behavior in response to mechanical strain due to genetic variation; studying that variability, let alone comparing that variability between cells acquired from asthmatic and normal members of the population, is even a useful experimental endpoint in itself. Even with an 'ideal' bioreactor which does not impart mechanical strain, temperature, or vibration stimuli which are not consistent with experimental SOPs, there will be sources of technical variation between different investigators. There would need to be a sufficient number of replicates to compensate for these sources of noise, and a sufficient number of different primary cell sources to evaluate the variability in response due to genetic variation across a given population. Regardless, the thesis identifies sources of technical variation due to bioreactor design that do not appear to have been previously identified and provides means of minimizing these sources of technical variation using equipment which is inexpensive or commonly available in prototyping spaces[117].

Static strain as an experimental variable has been explored much less than cyclic strain, so the implications are unclear; cells may be responding identically to cyclic and static strains, or static strain response may be a different phenomenon entirely. The observation of HASMc response to cyclic strain was consistent with previous experiments; the effects of static strain on HASMcs does not appear to have

been previously tested. In both cases, the cells realigned, although cell viability and temperature were not measured during these tests. Static strain caused no observable realignment in one experiment testing the effects of static strain on a cell lineage derived from aortic smooth muscle cells[118], although these cells might have more longitudinally arranged actin-myosin filaments, changing how the cytoskeleton would respond to strain. Protein expression was not evaluated, but MLC/MLCK expression has correlated with HASMc realignment in prior experiments[60].

The rationale for cyclic strain experiments in prior investigations was to assess the effects of respiratory strains on the smooth muscle cells and tissues, and the resulting alignment changes and MLC upregulation were associated with an asthmatic phenotype due to uniaxial strain[60]. If static strain has the same effect on cells as cyclic strain, at least when cells are cultured on a rubber substrate, it changes how these results may need to be interpreted and could undermine the rationale of the experiments. It is also possible that the SOPs for coating PDMS substrates were flawed or that the cells were injured in some way during passaging; the cells might be changing shape due to difficulties attaching to a stiffer, strained substrate and are simply clinging to the softest points available on the substrate. Regardless, realignment certainly occurred without cyclic strain under some experimental condition, which should be taken into account the next time this result is noted in bioreactor experiments and is assumed to have occurred in response to the cyclic strain stimulus. The stimulus could be physiologically relevant in airway remodeling, as changes in magnitude and anisotropy of airway stiffness are certainly expected during remodeling.

Although it is out of scope for this thesis, further study of static strain effects on HASMcs is warranted.

4 Conclusions

Using bioreactors to provide a simulacrum of the mechanical dynamics *in vivo* is a widely employed aspect of tissue engineering, mechanotransduction research, and the mechanical conditions affecting airway and ASM tissue remodelling, but there are basic issues in bioreactor design and application that may affect experimental results and which appear to have been unexplored. After reviewing airway physiology and ASM mechanobiology, this thesis determined a set of design objectives and constraints and determined a viable bioreactor design based on a review of prior bioreactor designs and FEA modeling of the strain conditions in the bioreactor. During the literature review and design phase, it became clear that heat generation and transfer, vibration, and unverified strain conditions on the well membranes added potentially confounding variables to experimental conditions, and that the bioreactor design and implementation needed to mitigate these issues. Further, tests to validate the bioreactor operation relative to unstrained and statically strained controls found that static strain also causes realignment of ASM cells, which has previously not been reported. Future bioreactor designs and experiments focused on ASM response to respiratory strains should design and implement bioreactor experiments with these variables in mind.

Heat generation and transfer has been rarely considered during bioreactor design, but depending on whether the bioreactor is designed to thermally isolate the cells from the actuators, even 1.5 W of heat emitted by an actuator was found to be more than sufficient to result in cells being cultured at over 40°C, which is sufficiently high to damage or kill the cells, or alter cellular expression and phenotype. Given the number of bioreactors that have employed bioreactor actuators with significantly higher power draw, this is a potentially confounding variable in bioreactor experiments and may invalidate experimental results. FEA simulations found that the incubator shelf would fail to transfer heat sufficiently effectively to keep the bioreactor and the incubator below 38°C and temperature readouts from the sensor inside the incubator will become inaccurate; experiments using power resistors found that convective heat exchange across the incubator shelf in an empty incubator will distribute heat across the incubator effectively,

although thermal conductivity across the bioreactor itself can still overheat the bioreactor cultures depending on design and actuator selection. Air cooling, measurement of bioreactor well temperatures, and thermal isolation of the cells from the rest of the bioreactor are advisable mitigation strategies.

Vibration emitted by the actuator in the 100-Hz bandwidth could affect the cytoskeleton based on tests performed on *ex vivo* tissues in other labs, but could not be fully explored. The accelerometers available for the project allowed the actuator vibration emitted within a 100-Hz bandwidth to be compared.

FEA modeling of the hyperelastic substrate provides a qualitative understanding of the strain distribution across the membrane for the ideal case, but characterization of the strain across the membrane surface was determined to be necessary to fully validate the bioreactor operation and to understand the actual strain patterns. Strain characterization of a PDMS membrane was attempted using a depth of focus technique, which was sufficient to detect errors in implementation. Resolution and repeatability of the vertical mapping method was $\pm 60\text{ }\mu\text{m}$ and $+25\text{ }\mu\text{m}$ for the focal depth and touch sensor methods respectively.

Bioreactor experiments meant to validate the cyclic strain stimulus and verify its effects on HASMCs delivered somewhat surprising results: static strain seemed to provoke cell realignment as readily as cyclic strain. The results should not be treated as conclusive, but further tests on HASMC response to static strain are warranted. Since the rationale for subjecting ASM cells to cyclic strain on rubber substrates in prior experiments has been to study the effects of cyclic strain on airway remodeling, if the cells do not appear to be able to distinguish cyclic strain from static strain, the conclusions drawn from these experiments may be undermined to some extent, or confound the ability to model the desired variables in airway remodelling or hyper-responsiveness specifically.

References

- [1] A. L. James, P. D. Paré, and J. C. Hogg, “The Mechanics of Airway Narrowing in Asthma,” *Am. Rev. Respir. Dis.*, vol. 139, no. 1, pp. 242–246, Jan. 1989.
- [2] U. Marx and V. Sandig, Eds., *Drug testing in vitro: breakthroughs and trends in cell culture technology*. Weinheim: Wiley-VCH, 2007.
- [3] Y. Chen, H. Johansen, S. Thillaiampalam, and C. Sambell, “Asthma,” *Health Rep.*, vol. 16, no. 2, pp. 43–46, Mar. 2005.
- [4] D. Dougherty, N. Sander, M. Schatz, K. S. Elward, G. S. Rachelefsky, W. Storms, J. Mitchell, R. M. Nowak, N. M. Clark, P. V. Williams, and others, “NATIONAL ASTHMA EDUCATION AND PREVENTION PROGRAM COORDINATING COMMITTEE,” *J ALLERGY CLIN IMMUNOL*, p. 5A, 2007.
- [5] F. T. Ishmael, “The Inflammatory Response in the Pathogenesis of Asthma,” *J. Am. Osteopath. Assoc.*, vol. 111, no. 11_suppl_7, pp. S11–S17, Nov. 2011.
- [6] “Asthma: Practice Essentials, Background, Anatomy.” [Online]. Available: <http://emedicine.medscape.com/article/296301-overview>. [Accessed: 05-Oct-2015].
- [7] P. J. Barnes, J. M. Drazen, S. I. Rennard, and N. C. Thomson, *Asthma and COPD: Basic Mechanisms and Clinical Management*. Elsevier, 2009.
- [8] P. T. Diaz, A. S. Bruns, M. E. Ezzie, N. Marchetti, and B. M. Thomashow, “Optimizing Bronchodilator Therapy in Emphysema,” *Proc. Am. Thorac. Soc.*, vol. 5, no. 4, pp. 501–505, May 2008.
- [9] L. Cheng, Y. Liu, Z. Su, J. Liu, R. Chen, and P. Ran, “Clinical characteristics of tobacco smoke-induced versus biomass fuel induced chronic obstructive pulmonary disease,” *J. Transl. Intern. Med.*, vol. 3, no. 3, pp. 126–129, 2015.
- [10] E. Wouters, “COPD: a chronic and overlooked pulmonary disease,” *The Lancet*, vol. 370, no. 9589, pp. 715–716, Sep. 2007.

- [11] N. J. Fairbank, S. C. Connolly, J. D. Mackinnon, K. Wehry, L. Deng, and G. N. Maksym, "Airway smooth muscle cell tone amplifies contractile function in the presence of chronic cyclic strain," *Am. J. Physiol. Lung Cell. Mol. Physiol.*, vol. 295, no. 3, pp. L479–488, Sep. 2008.
- [12] S. J. Hirst, "Airway smooth muscle cell culture: Application to studies of airway wall remodelling and phenotype plasticity in asthma," *Eur. Respir. J. Off. J. Eur. Soc. Clin. Respir. Physiol.*, vol. 9, no. 4, pp. 808–20, 1996.
- [13] G. N. Maksym, L. Deng, N. J. Fairbank, C. A. Lall, and S. C. Connolly, "Beneficial and harmful effects of oscillatory mechanical strain on airway smooth muscle," *Can. J. Physiol. Pharmacol.*, vol. 83, no. 10, pp. 913–922, Oct. 2005.
- [14] S. T. H. Darryl A Knight, "Knight DA, Holgate STThe airway epithelium: structural and functional properties in health and disease. *Respirology* 8:432–446," *Respirol. Carlton Vic*, vol. 8, no. 4, pp. 432–46, 2004.
- [15] B. C. Harvey, H. Parameswaran, and K. R. Lutchen, "Can tidal breathing with deep inspirations of intact airways create sustained bronchoprotection or bronchodilation?," *J. Appl. Physiol.*, vol. 115, no. 4, pp. 436–445, Aug. 2013.
- [16] J. H. T. Bates and A.-M. Lauzon, "Parenchymal tethering, airway wall stiffness, and the dynamics of bronchoconstriction," *J. Appl. Physiol.*, vol. 102, no. 5, pp. 1912–1920, May 2007.
- [17] J. R. Murdoch and C. M. Lloyd, "Chronic inflammation and asthma," *Mutat. Res.*, vol. 690, no. 1–2, pp. 24–39, Aug. 2010.
- [18] G. Pelaia, T. Renda, L. Gallelli, A. Vatrella, M. T. Busceti, S. Agati, M. Caputi, M. Cazzola, R. Maselli, and S. A. Marsico, "Molecular mechanisms underlying airway smooth muscle contraction and proliferation: Implications for asthma," *Respir. Med.*, vol. 102, no. 8, pp. 1173–1181, Aug. 2008.
- [19] M. Cazzola, C. P. Page, L. Calzetta, and M. G. Matera, "Pharmacology and Therapeutics of Bronchodilators," *Pharmacol. Rev.*, vol. 64, no. 3, pp. 450–504, Jan. 2012.

- [20] D. Price, P. Dale, E. Elder, and K. R. Chapman, "Types, frequency and impact of asthma triggers on patients' lives: a quantitative study in five European countries," *J. Asthma*, vol. 51, no. 2, pp. 127–135, Mar. 2014.
- [21] E. A. Koshak, "Classification of asthma according to revised 2006 GINA: Evolution from severity to control," *Ann. Thorac. Med.*, vol. 2, no. 2, pp. 45–46, 2007.
- [22] B. E. McParland, P. T. Macklem, and P. D. Pare, "Airway wall remodeling: friend or foe?," *J. Appl. Physiol. Bethesda Md 1985*, vol. 95, no. 1, pp. 426–434, Jul. 2003.
- [23] A. L. James, J. G. Elliot, R. L. Jones, M. L. Carroll, T. Mauad, T. R. Bai, M. J. Abramson, K. O. McKay, and F. H. Green, "Airway smooth muscle hypertrophy and hyperplasia in asthma," *Am. J. Respir. Crit. Care Med.*, vol. 185, no. 10, pp. 1058–1064, May 2012.
- [24] J. L. Black and P. R. Johnson, "Airway smooth muscle in asthma," *Respirol. Carlton Vic*, vol. 1, no. 3, pp. 153–158, Sep. 1996.
- [25] G. Skloot, S. Permutt, and A. Togias, "Airway hyperresponsiveness in asthma: a problem of limited smooth muscle relaxation with inspiration.," *J. Clin. Invest.*, vol. 96, no. 5, pp. 2393–2403, Nov. 1995.
- [26] D. S. Robinson, "The role of the mast cell in asthma: induction of airway hyperresponsiveness by interaction with smooth muscle?," *J. Allergy Clin. Immunol.*, vol. 114, no. 1, pp. 58–65, Jul. 2004.
- [27] P. K. Jeffery, "Differences and similarities between chronic obstructive pulmonary disease and asthma," *Clin. Exp. Allergy J. Br. Soc. Allergy Clin. Immunol.*, vol. 29 Suppl 2, pp. 14–26, Jun. 1999.
- [28] S. Louie, A. A. Zeki, M. Schivo, A. L. Chan, K. Y. Yoneda, M. Avdalovic, B. M. Morrissey, and T. E. Albertson, "The asthma-chronic obstructive pulmonary disease overlap syndrome: pharmacotherapeutic considerations," *Expert Rev. Clin. Pharmacol.*, vol. 6, no. 2, pp. 197–219, Mar. 2013.

- [29] J. M. Hughes, F. G. Hoppin, and J. Mead, "Effect of lung inflation on bronchial length and diameter in excised lungs," *J. Appl. Physiol.*, vol. 32, no. 1, pp. 25–35, Jan. 1972.
- [30] K. R. Lutchen, "Airway smooth muscle stretch and airway hyperresponsiveness in asthma: Have we chased the wrong horse?," *J. Appl. Physiol.*, vol. 116, no. 8, pp. 1113–1115, Apr. 2014.
- [31] P. W. Gunning, U. Ghoshdastider, S. Whitaker, D. Popp, and R. C. Robinson, "The evolution of compositionally and functionally distinct actin filaments," *J Cell Sci*, vol. 128, no. 11, pp. 2009–2019, Jun. 2015.
- [32] B. Lan, L. Wang, J. Zhang, C. D. Pascoe, B. A. Norris, J. C.-Y. Liu, D. Solomon, P. D. Paré, L. Deng, and C. Y. Seow, "Rho-kinase mediated cytoskeletal stiffness in skinned smooth muscle," *J. Appl. Physiol. Bethesda Md 1985*, vol. 115, no. 10, pp. 1540–1552, Nov. 2013.
- [33] D. Rizzo, *Fundamentals of anatomy & physiology (Book, 2006) [WorldCat.org]*. Delmar Cengage Learning, 2010.
- [34] R. C. Webb, "Smooth Muscle Contraction and Relaxation," *Adv. Physiol. Educ.*, vol. 27, no. 4, pp. 201–206, Dec. 2003.
- [35] G. M. Cooper, "Actin, Myosin, and Cell Movement,". *The Cell: A Molecular Approach*. 2nd Ed. 2000.
- [36] T. D. Pollard and J. A. Cooper, "Actin, a Central Player in Cell Shape and Movement," *Science*, vol. 326, no. 5957, pp. 1208–1212, Nov. 2009.
- [37] J. R. Haeberle and M. E. Hemric, "A model for the coregulation of smooth muscle actomyosin by caldesmon, calponin, tropomyosin, and the myosin regulatory light chain," *Can. J. Physiol. Pharmacol.*, vol. 72, no. 11, pp. 1400–1409, Nov. 1994.
- [38] M. L. Costa, R. Escaleira, A. Cataldo, F. Oliveira, and C. S. Mermelstein, "Desmin: molecular interactions and putative functions of the muscle intermediate filament protein," *Braz. J. Med. Biol. Res.*, vol. 37, no. 12, pp. 1819–1830, Dec. 2004.

- [39] J. Latourelle, B. Fabry, and J. J. Fredberg, "Dynamic equilibration of airway smooth muscle contraction during physiological loading," *J. Appl. Physiol.*, vol. 92, no. 2, pp. 771–779, Feb. 2002.
- [40] S. M. Mijailovich, J. P. Butler, and J. J. Fredberg, "Perturbed Equilibria of Myosin Binding in Airway Smooth Muscle: Bond-Length Distributions, Mechanics, and ATP Metabolism," *Biophys. J.*, vol. 79, no. 5, pp. 2667–2681, Nov. 2000.
- [41] C. Y. Seow and J. J. Fredberg, "Emergence of airway smooth muscle functions related to structural malleability," *J. Appl. Physiol.*, vol. 110, no. 4, pp. 1130–1135, Apr. 2011.
- [42] J. J. Fredberg, D. Inouye, B. Miller, M. Nathan, S. Jafari, S. Helioui Raboudi, J. P. Butler, and S. A. Shore, "Airway Smooth Muscle, Tidal Stretches, and Dynamically Determined Contractile States," *Am. J. Respir. Crit. Care Med.*, vol. 156, no. 6, pp. 1752–1759, Dec. 1997.
- [43] Y. Bossé, L. Y. M. Chin, P. D. Paré, and C. Y. Seow, "Chronic Activation in Shortened Airway Smooth Muscle," *Am. J. Respir. Cell Mol. Biol.*, vol. 42, no. 3, pp. 341–348, Mar. 2010.
- [44] J. J. Fredberg, D. S. Inouye, S. M. Mijailovich, and J. P. Butler, "Perturbed Equilibrium of Myosin Binding in Airway Smooth Muscle and Its Implications in Bronchospasm," *Am. J. Respir. Crit. Care Med.*, vol. 159, no. 3, pp. 959–967, Mar. 1999.
- [45] T. Kapsali, S. Permutt, B. Laube, N. Scichilone, and A. Togias, "Potent bronchoprotective effect of deep inspiration and its absence in asthma," *J. Appl. Physiol.*, vol. 89, no. 2, pp. 711–720, 2000.
- [46] A. J. Halayko, B. Camoretti-Mercado, S. M. Forsythe, J. E. Vieira, R. W. Mitchell, M. E. Wylam, M. B. Hershenson, and J. Solway, "Divergent differentiation paths in airway smooth muscle culture: induction of functionally contractile myocytes," *Am. J. Physiol.*, vol. 276, no. 1 Pt 1, pp. L197–206, Jan. 1999.
- [47] A. J. Halayko, H. Salari, X. Ma, and N. L. Stephens, "Markers of airway smooth muscle cell phenotype," *Am. J. Physiol.*, vol. 270, no. 6 Pt 1, pp. L1040–1051, Jun. 1996.

- [48] V. R. Babaev, Y. V. Bobryshev, O. V. Stenina, E. M. Tararak, and G. Gabbiani, "Heterogeneity of smooth muscle cells in atheromatous plaque of human aorta," *Am. J. Pathol.*, vol. 136, no. 5, pp. 1031–1042, May 1990.
- [49] A. P. Nesmith, A. Agarwal, M. L. McCain, and K. K. Parker, "Human airway musculature on a chip: an in vitro model of allergic asthmatic bronchoconstriction and bronchodilation," *Lab. Chip*, vol. 14, no. 20, pp. 3925–3936, Oct. 2014.
- [50] N. K. Malavia, C. B. Raub, S. B. Mahon, M. Brenner, R. A. Panettieri, and S. C. George, "Airway epithelium stimulates smooth muscle proliferation," *Am. J. Respir. Cell Mol. Biol.*, vol. 41, no. 3, pp. 297–304, Sep. 2009.
- [51] Q. Hamid, J. Shannon, and J. Martin, *Physiologic Basis of Respiratory Disease*. PMPH-USA, 2005.
- [52] S. C. Connolly, P. G. Smith, N. J. Fairbank, C. A. Lall, D. J. Cole, J. D. MacKinnon, and G. N. Maksym, "Chronic oscillatory strain induces MLCK associated rapid recovery from acute stretch in airway smooth muscle cells," *J. Appl. Physiol.*, vol. 111, no. 4, pp. 955–963, Oct. 2011.
- [53] S. S. An, T. R. Bai, J. H. T. Bates, J. L. Black, R. H. Brown, V. Brusasco, P. Chitano, L. Deng, M. Dowell, D. H. Eidelman, B. Fabry, N. J. Fairbank, L. E. Ford, J. J. Fredberg, W. T. Gerthoffer, S. H. Gilbert, R. Gosens, S. J. Gunst, A. J. Halayko, R. H. Ingram, C. G. Irvin, A. L. James, L. J. Janssen, G. G. King, D. A. Knight, A. M. Lauzon, O. J. Lakser, M. S. Ludwig, K. R. Lutchen, G. N. Maksym, J. G. Martin, T. Mauad, B. E. McParland, S. M. Mijailovich, H. W. Mitchell, R. W. Mitchell, W. Mitzner, T. M. Murphy, P. D. Paré, R. Pellegrino, M. J. Sanderson, R. R. Schellenberg, C. Y. Seow, P. S. P. Silveira, P. G. Smith, J. Solway, N. L. Stephens, P. J. Sterk, A. G. Stewart, D. D. Tang, R. S. Tepper, T. Tran, and L. Wang, "Airway smooth muscle dynamics: a common pathway of airway obstruction in asthma," *Eur. Respir. J. Off. J. Eur. Soc. Clin. Respir. Physiol.*, vol. 29, no. 5, pp. 834–860, May 2007.

- [54] J. H.-C. Wang, G. Yang, Z. Li, and W. Shen, "Fibroblast responses to cyclic mechanical stretching depend on cell orientation to the stretching direction," *J. Biomech.*, vol. 37, no. 4, pp. 573–576, Apr. 2004.
- [55] G. N. Maksym, L. Deng, N. J. Fairbank, C. A. Lall, and S. C. Connolly, "Beneficial and harmful effects of oscillatory mechanical strain on airway smooth muscle," *Can J Physiol Pharmacol*, vol. 83, no. 10, pp. 913–922, Oct. 2005.
- [56] H. Tseng, J. A. Gage, R. M. Raphael, R. H. Moore, T. C. Killian, K. J. Grande-Allen, and G. R. Souza, "Assembly of a three-dimensional multitype bronchiole coculture model using magnetic levitation," *Tissue Eng. Part C Methods*, vol. 19, no. 9, pp. 665–675, Sep. 2013.
- [57] G. E. Morris, J. C. Bridge, O. M. I. Eltboli, M. P. Lewis, A. J. Knox, J. W. Aylott, C. E. Brightling, A. M. Ghaemmaghami, and F. R. a. J. Rose, "Human airway smooth muscle maintain in situ cell orientation and phenotype when cultured on aligned electrospun scaffolds," *Am. J. Physiol. Lung Cell. Mol. Physiol.*, vol. 307, no. 1, pp. L38–47, Jul. 2014.
- [58] C. Walthers, "Regeneration and Maintenance of Intestinal Smooth Muscle Phenotypes.," *eScholarship*, Jan. 2014.
- [59] A. R. West, N. Zaman, D. J. Cole, M. J. Walker, W. R. Legant, T. Boudou, C. S. Chen, J. T. Favreau, G. R. Gaudette, E. A. Cowley, and G. N. Maksym, "Development and characterization of a 3D multicell microtissue culture model of airway smooth muscle," *Am. J. Physiol. - Lung Cell. Mol. Physiol.*, vol. 304, no. 1, pp. L4–L16, Jan. 2013.
- [60] G. N. Maksym, L. Deng, N. J. Fairbank, C. A. Lall, and S. C. Connolly, "Beneficial and harmful effects of oscillatory mechanical strain on airway smooth muscle," *Can J Physiol Pharmacol*, vol. 83, no. 10, pp. 913–922, Oct. 2005.
- [61] A. A. Lee, T. Delhaas, L. K. Waldman, D. A. MacKenna, F. J. Villarreal, and A. D. McCulloch, "An equibiaxial strain system for cultured cells," *Am J Physiol*, vol. 271, no. 4 Pt 1, pp. C1400–1408, Oct. 1996.

- [62] L. Huang, P. S. Mathieu, and B. P. Helmke, "A Stretching Device for High Resolution Live-Cell Imaging," *Ann. Biomed. Eng.*, vol. 38, no. 5, pp. 1728–1740, May 2010.
- [63] R. A. Gould, K. Chin, T. P. Santisakultarm, A. Dropkin, J. M. Richards, C. B. Schaffer, and J. T. Butcher, "Cyclic strain anisotropy regulates valvular interstitial cell phenotype and tissue remodeling in three-dimensional culture," *Acta Biomater.*, vol. 8, no. 5, pp. 1710–1719, May 2012.
- [64] "COMSOL Multiphysics® Modeling Software." [Online]. Available: <http://www.comsol.com/>. [Accessed: 06-Feb-2016].
- [65] M. C. Boyce and E. M. Arruda, "Constitutive Models of Rubber Elasticity: A Review," *Rubber Chem. Technol.*, vol. 73, no. 3, pp. 504–523, Jul. 2000.
- [66] Ali, "A Review of Constitutive Models for Rubber-Like Materials," *Am. J. Eng. Appl. Sci.*, vol. 3, no. 1, pp. 232–239, Jan. 2010.
- [67] "Applied Mechanics of Solids (A.F. Bower) Chapter 3: Constitutive laws - 3.5 Hyperelasticity." [Online]. Available: http://solidmechanics.org/text/Chapter3_5/Chapter3_5.htm. [Accessed: 01-Feb-2016].
- [68] ANSYS, Inc., "Hyperelasticity." [Online]. Available: http://ansys.net/ansys/papers/nonlinear/conflong_hyperel.pdf. [Accessed: 01-Feb-2016].
- [69] T. K. Kim, J. K. Kim, and O. C. Jeong, "Measurement of nonlinear mechanical properties of PDMS elastomer," *Microelectron. Eng.*, vol. 88, no. 8, pp. 1982–1985, Aug. 2011.
- [70] B. Beca, "A Platform for High-throughput Mechanobiological Stimulation of Engineered Microtissues," 2012.
- [71] "32F411EDISCOVERY Discovery kit with STM32F411VE MCU - STMicroelectronics." [Online]. Available: <http://www.st.com/>. [Accessed: 21-Jan-2016].
- [72] E. Zhao, "Cardiomyocyte differentiation with cyclic mechanical strain", M.A.Sc. Thesis, Dept. Mech. Eng., UBC, Vancouver, BC, 2015.

- [73] T. J. Lujan, K. M. Wirtz, C. S. Bahney, S. M. Madey, B. Johnstone, and M. Bottlang, "A Novel Bioreactor for the Dynamic Stimulation and Mechanical Evaluation of Multiple Tissue-Engineered Constructs," *Tissue Eng. Part C Methods*, vol. 17, no. 3, pp. 367–374, Oct. 2010.
- [74] M. A. Brady, R. Vaze, H. D. Amin, D. R. Overby, and C. R. Ethier, "The Design and Development of a High-Throughput Magneto-Mechanostimulation Device for Cartilage Tissue Engineering," *Tissue Eng Part C Methods*, vol. 20, no. 2, pp. 149–159, Feb. 2014.
- [75] W. F. Ong, A. C. Ritchie, and K. S. Chian, "Effects of Biaxial Mechanical Strain on Esophageal Smooth Muscle Cells," in *13th International Conference on Biomedical Engineering*, C. T. Lim and J. C. H. Goh, Eds. Springer Berlin Heidelberg, 2009, pp. 1484–1487.
- [76] Q. Pang, "Design and Development of a Biostretch Apparatus for Tissue Engineering," Ph.D. dissertation, Dept. Mech. Eng., UT, Toronto, 2010.
- [77] "Rapid shallow breathing: MedlinePlus Medical Encyclopedia." [Online]. Available: <https://www.nlm.nih.gov/medlineplus/ency/article/007198.htm>. [Accessed: 08-Jan-2016].
- [78] "Target Heart Rates." [Online]. Available: <http://www.heart.org/HEARTORG/GettingHealthy/PhysicalActivity/FitnessBasics/>. [Accessed: 08-Jan-2016].
- [79] A. T. Cashion, M. Caballero, A. Halevi, A. Pappa, R. G. Dennis, and J. A. van Aalst, "Programmable mechanobioreactor for exploration of the effects of periodic vibratory stimulus on mesenchymal stem cell differentiation," *Biores Open Access*, vol. 3, no. 1, pp. 19–28, Feb. 2014.
- [80] M. J. Turner, V. A. Davies, T. J. De Ravel, A. D. Rothberg, and I. M. MacLeod, "Bandwidths of respiratory gas flow and pressure waveforms in mechanically ventilated infants," *Physiol. Meas.*, vol. 14, no. 4, pp. 419–431, Nov. 1993.
- [81] "HAYDON™ Stepper Motor Linear Actuators." [Online]. Available: <http://www.haydonkerk.com/LinearActuatorProducts/StepperMotorLinearActuators/>. [Accessed 01-Feb-2016].

- [82] R. G. Bacabac, T. H. Smit, J. J. W. A. V. Loon, B. Z. Doulabi, M. Helder, and J. Klein-Nulend, "Bone cell responses to high-frequency vibration stress: does the nucleus oscillate within the cytoplasm?," *FASEB J.*, vol. 20, no. 7, pp. 858–864, May 2006.
- [83] J. C. Wolchok, C. Brokopp, C. J. Underwood, and P. A. Tresco, "The effect of bioreactor induced vibrational stimulation on extracellular matrix production from human derived fibroblasts," *Biomaterials*, vol. 30, no. 3, pp. 327–335, Jan. 2009.
- [84] I. R. Titze, R. W. Hitchcock, K. Broadhead, K. Webb, W. Li, S. D. Gray, and P. A. Tresco, "Design and validation of a bioreactor for engineering vocal fold tissues under combined tensile and vibrational stresses," *J. Biomech.*, vol. 37, no. 10, pp. 1521–1529, Oct. 2004.
- [85] Y. Du, "Airway smooth muscle response to vibrations," Thesis, Auckland University of Technology, 2006.
- [86] "2-phase vs. 5-phase Stepper Motors." [Online]. Available: <http://www.orientalmotor.com/technology/articles/2phase-v-5phase.html>. [Accessed: 09-Jan-2016].
- [87] "Industrial Circuits Application Note Microstepping." [Online]. Available: <http://users.ece.utexas.edu/~valvano/Datasheets/StepperMicrostep.pdf>. [Accessed: 10-Jan-2016].
- [88] K. Webb, R. W. Hitchcock, R. M. Smeal, W. Li, S. D. Gray, and P. A. Tresco, "Cyclic strain increases fibroblast proliferation, matrix accumulation, and elastic modulus of fibroblast-seeded polyurethane constructs," *J. Biomech.*, vol. 39, no. 6, pp. 1136–1144, 2006.
- [89] M. C. Sutcliffe and J. M. Davidson, "Effect of static stretching on elastin production by porcine aortic smooth muscle cells," *Matrix Stuttg. Ger.*, vol. 10, no. 3, pp. 148–153, Jul. 1990.
- [90] "Arduino - ArduinoBoardMega." [Online]. Available: <https://www.arduino.cc/en/Main/arduinoBoardMega>. [Accessed: 11-Feb-2016].
- [91] "EasyDriver - Stepper Motor Driver - ROB-12779 - SparkFun Electronics." [Online]. Available: <https://www.sparkfun.com/products/12779>. [Accessed: 11-Feb-2016].

- [92] W. W. Ahmed, M. H. Kural, and T. A. Saif, "A novel platform for in situ investigation of cells and tissues under mechanical strain," *Acta Biomater*, vol. 6, no. 8, pp. 2979–2990, Aug. 2010.
- [93] "Hammond Mfg. - Diecast Aluminum - Watertight - w/ Flanged Lid (1590W_FL Series)." [Online]. Available: http://www.hammondmfg.com/dwgdw_FL.htm. [Accessed: 12-Feb-2016].
- [94] I. Watanabe and S. Okada, "EFFECTS OF TEMPERATURE ON GROWTH RATE OF CULTURED MAMMALIAN CELLS (L5178Y)," *J Cell Biol*, vol. 32, no. 2, pp. 309–323, Feb. 1967.
- [95] K. Richter, M. Haslbeck, and J. Buchner, "The Heat Shock Response: Life on the Verge of Death," *Mol. Cell*, vol. 40, no. 2, pp. 253–266, Oct. 2010.
- [96] C. Saini, J. Morf, M. Stratmann, P. Gos, and U. Schibler, "Simulated body temperature rhythms reveal the phase-shifting behavior and plasticity of mammalian circadian oscillators," *Genes Dev*, vol. 26, no. 6, pp. 567–580, Mar. 2012.
- [97] R. E. U. Student, R. Cintrón, R. E. U. Mentor, and V. Saouma, "Strain measurements with the digital image correlation system Vic-2D," *System*, vol. 106, p. 2D, 2008.
- [98] M. N. Helfrick, C. Niezrecki, P. Avitabile, and T. Schmidt, "3D digital image correlation methods for full-field vibration measurement," *Mech. Syst. Signal Process.*, vol. 25, no. 3, pp. 917–927, 2011.
- [99] K. Genovese, L. Casaletto, J. A. Rayas, V. Flores, and A. Martinez, "Stereo-Digital Image Correlation (DIC) measurements with a single camera using a biprism," *Opt. Lasers Eng.*, vol. 51, no. 3, pp. 278–285, Mar. 2013.
- [100] W. Gubbels, "3-D Digital Image Correlation using a single color-camera," M.A.Sc. thesis, Mech. Eng., UBC, Vancouver, BC, 2014.
- [101] J. Geng, "Structured-light 3D surface imaging: a tutorial," *Adv. Opt. Photonics*, vol. 3, no. 2, p. 128, Jun. 2011.

- [102] Vermeulen, MMPA (Marc), “High-precision 3D-coordinate measuring machine : design and prototype-development,” 1999.
- [103] “POTENTIOMETER (SLIDE (B)) 100K SL60V - Lee’s Electronic.” [Online]. Available: <http://leeselectronic.com/product/71302.html>. [Accessed: 08-Feb-2016].
- [104] P. B. Lücker, S. Javaherian, J. P. Soleas, D. Halverson, P. W. Zandstra, and A. P. McGuigan, “A microgroove patterned multiwell cell culture plate for high-throughput studies of cell alignment,” *Biotechnol. Bioeng.*, vol. 111, no. 12, pp. 2537–2548, Dec. 2014.
- [105] B. C. Harvey, H. Parameswaran, and K. R. Lutchen, “Can breathing-like pressure oscillations reverse or prevent narrowing of small intact airways?,” *J. Appl. Physiol.*, vol. 119, no. 1, pp. 47–54, Jul. 2015.
- [106] R. R. Christian Schott, “A new two-axis magnetic position sensor,” vol. 2, pp. 911–915 vol.2, 2002.
- [107] Y. C. Yung, H. Vandeburgh, and D. J. Mooney, “Cellular strain assessment tool (CSAT): precision-controlled cyclic uniaxial tensile loading,” *J. Biomech.*, vol. 42, no. 2, pp. 178–182, Jan. 2009.
- [108] H. H. Vandeburgh, S. Swasdison, and P. Karlisch, “Computer-aided mechanogenesis of skeletal muscle organs from single cells in vitro.,” *FASEB J.*, vol. 5, no. 13, pp. 2860–2867, Jan. 1991.
- [109] C. A. Powell, B. L. Smiley, J. Mills, and H. H. Vandeburgh, “Mechanical stimulation improves tissue-engineered human skeletal muscle,” *Am. J. Physiol. - Cell Physiol.*, vol. 283, no. 5, pp. C1557–C1565, Nov. 2002.
- [110] T. Wang, B. S. Gardiner, Z. Lin, J. Rubenson, T. B. Kirk, A. Wang, J. Xu, D. W. Smith, D. G. Lloyd, and M. H. Zheng, “Bioreactor design for tendon/ligament engineering,” *Tissue Eng. Part B Rev.*, vol. 19, no. 2, pp. 133–146, Apr. 2013.
- [111] J. J. Lau, R. M. Wang, and L. D. Black, “Development of an Arbitrary Waveform Membrane Stretcher for Dynamic Cell Culture,” *Ann. Biomed. Eng.*, vol. 42, no. 5, pp. 1062–1073, May 2014.

- [112] C. Picard, V. Hearnden, M. Massignani, S. Achouri, G. Battaglia, S. MacNeil, and A. Donald, “A micro-incubator for cell and tissue imaging,” *BioTechniques*, vol. 48, no. 2, pp. 135–138, Feb. 2010.
- [113] “pellinglab.net,” *pellinglab.net*. .
- [114] K. Haubert, T. Drier, and D. Beebe, “PDMS bonding by means of a portable, low-cost corona system,” *Lab. Chip*, vol. 6, no. 12, pp. 1548–1549, Nov. 2006.
- [115] D. Bodas and C. Khan-Malek, “Hydrophilization and hydrophobic recovery of PDMS by oxygen plasma and chemical treatment—An SEM investigation,” *Sens. Actuators B Chem.*, vol. 123, no. 1, pp. 368–373, Apr. 2007.
- [116] N. Altman and M. Krzywinski, “Points of significance: Sources of variation,” *Nat. Methods*, vol. 12, no. 1, pp. 5–6, Jan. 2015.
- [117] “The Industrial Machinery of Makerspaces | Make:,” *Make: DIY Projects and Ideas for Makers*, 14-Aug-2014. [Online]. Available: <http://makezine.com/2014/08/14/industrial-instruments/>. [Accessed: 05-Sep-2016].
- [118] K. Hayakawa, A. Hosokawa, K. Yabusaki, and T. Obinata, “Orientation of Smooth Muscle-Derived A10 Cells in Culture by Cyclic Stretching: Relationship between Stress Fiber Rearrangement and Cell Reorientation,” *Zoolog. Sci.*, vol. 17, no. 5, pp. 617–624, Jul. 2000.